

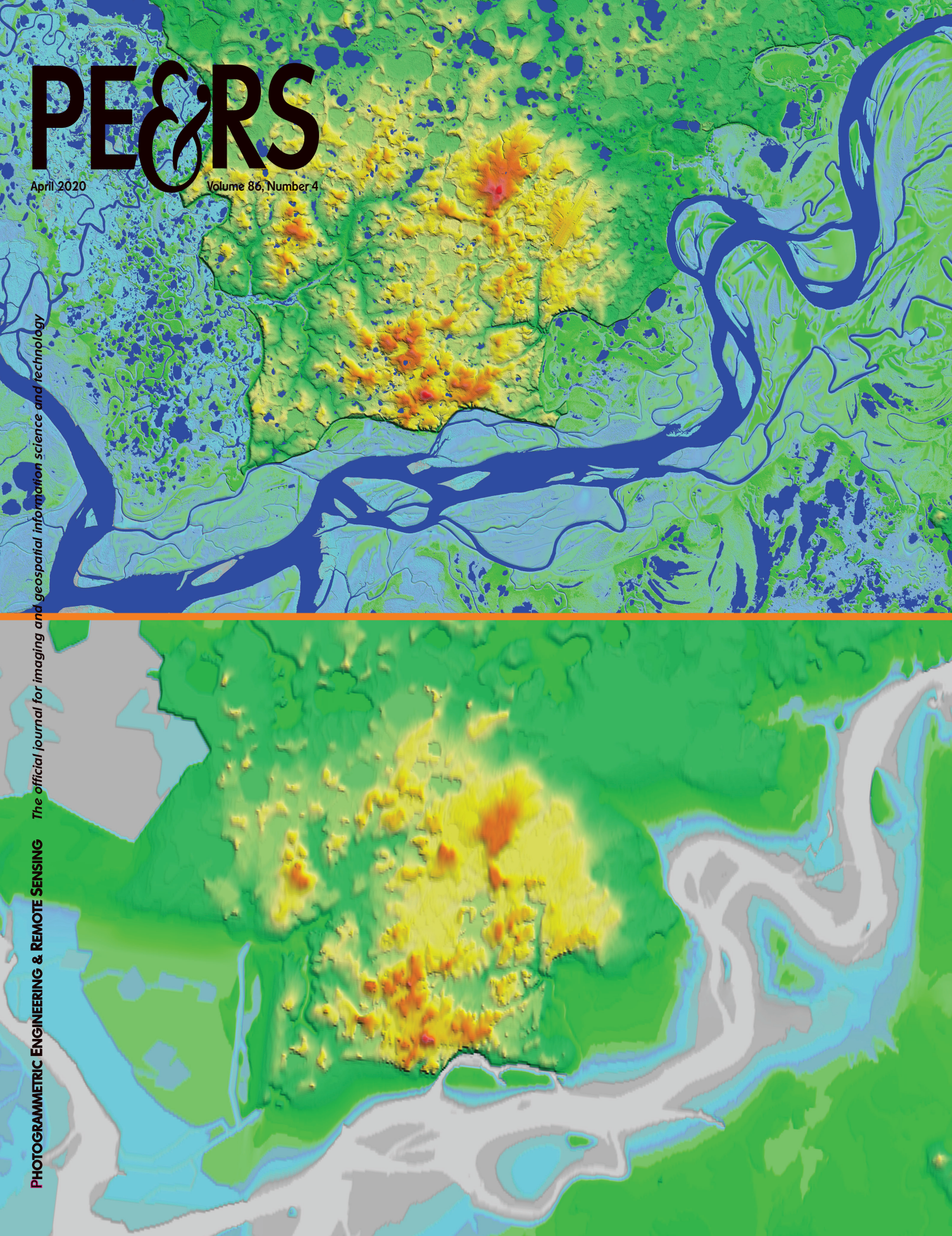
PE&RS

April 2020

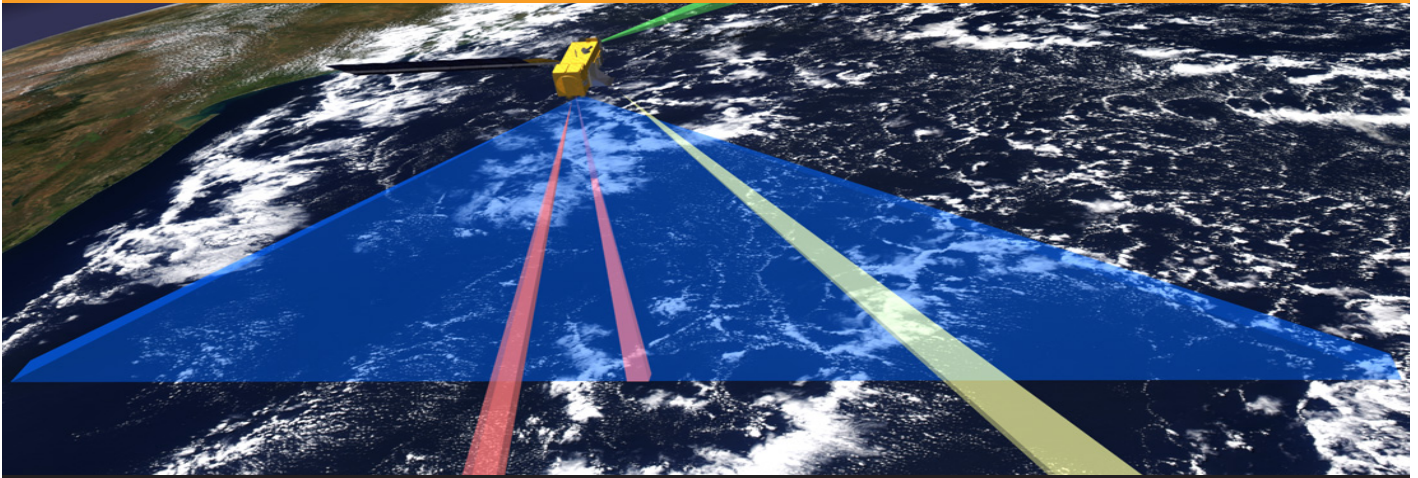
Volume 86, Number 4

The official journal for imaging and geospatial information science and technology

PHOTOGRAMMETRIC ENGINEERING & REMOTE SENSING



NOW AVAILABLE!



MANUAL OF REMOTE SENSING

Fourth Edition

ASPRS Announces the 4th Edition of the *Manual of Remote Sensing*!

The *Manual of Remote Sensing, 4th Ed.* (MRS-4) is an “enhanced” electronic publication available online from ASPRS. This edition expands its scope from previous editions, focusing on new and updated material since the turn of the 21st Century. Stanley Morain (Editor-in-Chief), and co-editors Michael Renslow and Amelia Budge have compiled material provided by numerous contributors who are experts in various aspects of remote sensing technologies, data preservation practices, data access mechanisms, data processing and modeling techniques, societal benefits, and legal aspects such as space policies and space law. These topics are organized into nine chapters. MRS4 is unique from previous editions in that it is a “living” document that can be updated easily in years to come as new technologies and practices evolve. It also is designed to include animated illustrations and videos to further enhance the reader’s experience.

MRS-4 is available to ASPRS Members as a member benefit or can be purchased by non-members. To access MRS-4, visit <https://my.asprs.org/mrs4>.



edited by: Stanley A. Morain,
Michael S. Renslow and Amelia M. Budge



The goal of the Manual of Remote Sensing-4 was to create a more effective, affordable, and durable Manual, and to broaden its scope to include economic and societal benefits. Effective in the sense that MRS-4's content could be found online as an enhanced e-book; affordable in the sense that content could be retrieved by everyone on an annual subscription basis; and durable in the sense that it could be easily updated as a "living" manual through fresh, contributor-driven and vetted material as technologies advance. It does not reprise the extensive mathematical basis for remote sensing given in MRS-2, but instead focuses on system designs; data processing, storage, and retrieval; and on societal applications. A key feature of this concept is to facilitate timely updates of cutting edge or new developments from a wide spectrum of sophisticated contributors facile collectively with the technological, mathematical, and utilitarian aspects of Earth and space sciences.

Table of Contents

Preface

Stanley A. Morain, Michael S. Renslow, and Amelia M. Budge

Chapter 1: Fundamentals of Electromagnetic Radiation

Stanley A. Morain and Amelia M. Budge

Chapter 2: Sensors and Platforms

Charles K. Toth, Kenneth Jezek, Franz Meyer, Batuhan Osmanoglu, Stanley A. Morain and Amelia M. Budge

Chapter 3: Selected 21st Century Remote Sensing Technologies

Stanley A. Morain, Shizuo Yamamoto, Mihail C. Roco, Chad A. Mirkin, Mark C. Hersam, Yves Tourre, C. Vignolles and J-P. Lacaux

Chapter 4: Unmanned Aerial Systems for Low-Altitude Remote Sensing

Costas Armenakis, Brandon Stark, Brendan Smith, YangQuan Chen, Ravi A. Persad, Julien Li-Chee-Ming, Norbert Haala, Michael Cramer, Jeff L. Sloan and Jill J. Cress

Chapter 5: Quality Assurance and Quality Control of Remote Sensing Systems

Ayman Habib, Eija Honkavaara, Karsten Jacobsen, Ana Paula Kersting, Zahra Lari, Aparajithan Sampath, Ahmed Shaker and Wai Yeung Yan

Chapter 6: Archiving and Access Systems for Remote Sensing

John Faundeen, George Percivall, Shirley Baros, Peter Baumann, Peter Becker, J. Behnke, Karl Benedict, Lucio Colaiacomo, Liping Di, Chris Doescher, J. Dominguez, Roger Edberg, Mark Ferguson, Stephen Foreman, David Giaretta, Vivian B. Hutchison, Alex Ip, N.L. James, Siri Jodha S. Khalsa, B. Lazorchak, Adam Lewis, Fuqin Li, Leo Lymburner, C.S. Lynnes, Matt Martens, Rachel Melrose, Steve Morris, Norman Mueller, Vivek Navale, Kumar Navulur, D.J. Newman, Simon Oliver, Matthew Purss, H.K. Ramapriyan, Russ Rew, Michael Rosen, John Savickas, Joshua Sixsmith, Tom Sohre, David Thau, Paul Uhler, Lan-Wei Wang and Jeff Young

Chapter 7: Image Processing and Analysis Methods

Sergio Bernardes, Marguerite Madden, Ike Astuti, Sergio Bernardes, Emilio Chuvieco, David Cotten, Philip E. Dennison, Iryna Dronova, Ioannis Gitas, Peng Gong, Belen Franch-Gras, Matt Hancher, Akira Hirano, Allison Howard, Xuefei Hu, Alfredo Huete, Thomas Jordan, Chris Justice, Rick L. Lawrence, Linlin Lu, Marguerite Madden, Deepak R. Mishra, Sachidananda Mishra, Tomoaki Miura, Giorgos Mountrakis, Mahesh Pal, Caren Remillard, Dar A. Roberts, Jean-Claude Roger, Kunwar K. Singh, Ben Somers, Dimitris Stavrakoudis, Wanxiao Sun, Guoqing Sun, David Thau, Laurent Tits, E. Lynn Usery, Eric Vermote, Cuizhen Wang, Mingshu Wang, Qihao Weng, Wenjing Xu, Tian Yao, Hiroki Yoshioka, Lei Zhang, Qingyuan Zhang and Zhi Zhang

Chapter 8: Societal Benefits - Methods and Examples for Estimating the Value of Remote Sensing Information

Richard Bernknopf, David Brookshire, Molly Macauley, Guy Jakeman, Yusuke Kuwayama, Holly Miller, Leslie Richardson and Alan Smart

Chapter 9: Space Policy and Space Law

Joanne Gabrynowicz, Karen D. Dacres, Kevin O'Connell, Kevin Pomfret and Timothy F. Robertson

Master Acronym/Abbreviations List

**MRS-4 is available to ASPRS Members
as a member benefit or
can be purchased by non-members.
To access MRS-4,
visit <https://my.asprs.org/mrs4>.**



ANNOUNCEMENTS

GeoCue Group is pleased to announce a partnership with Sumac Geomatics Incorporated, based in Thunder Bay, Ontario, as a Canadian distributor for GeoCue's True View® integrated LIDAR/Imaging sensors for UAV/drone operations. Sumac Geomatics will be supporting True View customers in Ontario and Manitoba. GeoCue's new True View product line provides integrated drone-based 3D LIDAR/Imaging sensors with full workflow software from data capture to product generation. The True View 410 is available for immediate delivery, with additional models being introduced later this year. True View sensors are available as a traditional equipment purchase or as an innovative Hardware-as-a-Service (HaaS) subscription model.

Sumac Geomatics is a service provider to the forestry, mining and civil engineering sectors. With strong foundations in Geographic Information Systems (GIS), remote sensing, photogrammetry, and field services, Sumac's team has a reputation of delivering projects across Canada, especially in remote locations and communities. In a rapidly evolving industry, Sumac works hard to stay on the cutting-edge of software, hardware, and operational advances to remain responsive and effective both in the field and in the office. The company was one of the first in Canada to pioneer the commercial use of Remotely Piloted Aerial Systems (drones) and photogrammetry for high resolution mapping and surveying, has developed new approaches to forest operations planning, and is the Eastern Canada field service partner for the Photodocufy facility documentation service. More recently, Sumac has diversified its business with a hardware solutions business line. This includes becoming Canadian sales and service representative for the Teledyne Optech Cavity Monitoring System (CMS), an industry standard technology for monitoring/measuring stope-based mining. Sumac's project experiences are now perfectly suited to bringing the True View 3D imaging system to its customers in Ontario and Manitoba.

To learn more, visit www.geocue.com.

Teledyne Optech, a Teledyne Technologies, is pleased to announce that OGL Engineering of Calgary, Alberta is the first Canadian company to purchase the Optech Galaxy T2000 lidar sensor. With the purchase of the Galaxy T2000 and a GSM4000 sensor mount, OGL will increase the efficiency of their aerial data collection, which includes projects for a variety of industries including: electric utilities, pipelines, forestry, mining, and government infrastructure. As a team that provides A to Z aerial survey services from project design and data acquisition, through to data processing and engineering analysis, OGL understands how integral a reliable and efficient data acquisition solution is to achieve project success.

The Galaxy T2000 boasts a true 2 MHz laser emission rate directed fully to the ground by a new high frequency, programmable scanner for effective point distribution. Combined

with Teledyne Optech's patented SwathTRAK™ capability, the Galaxy T2000 is capable of maintaining fixed-width data swaths in mountainous terrain via an innovative and dynamic field-of-view (FOV), enabling far fewer flight lines and more equidistant point spacing compared to fixed-FOV sensor designs.

Find out more at www.teledyneoptech.com.

EQUIPMENT

A **SPECTRAL EVOLUTION** distributor in China, Azup International Group, Ltd., mounted a new RS-8800 field spectroradiometer on a drone and took some field scans.

The RS-8800 field spectroradiometer is a full range (350-2500nm) high resolution/high sensitivity system including an Internet of Things (IoT) operating system that allows you to operate the system by iPhone, Android device, or tablet. In combination with our new Sensa/Tilt™ gimbal stabilized fiber holder, researchers can access and store more important field data in addition to their scans, including:

- A picture of the exact sample Field of View that you want to scan
- The angle of the scan
- The sun height angle
- The GPS location

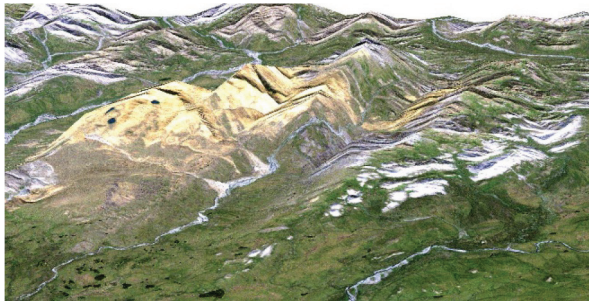
The SR-8800 uses its IoT operating system to control the pistol grip functionality so that any user can get consistent scans. The IoT uses a WiFi network accessed by an Android device, iPhone or tablet for controlling the system and downloading data stored on the instrument.

For more information, visit: <https://spectralevolution.com/applications/remote-sensing/rs-8800-mounted-on-a-drone/>.

CALENDAR

- 7-9 May, **GISTAM 2020—6th International Conference on Geographical Information Systems Theory, Applications and Management**, Prague, Czech Republic. For more information, visit: www.gistam.org/.
- 18-20 May, **UAV STRATUS**, Buffalo, New York. For more information, visit <http://stratus-conference.com/home>.
- 20-22 May, **AutoCarto 2020**, Redlands, California. For more information, visit <https://cartogis.org/autocarto/>.
- 15-22 August, **43rd COSPAR Scientific Assembly**, Sydney, Australia. For more information, visit www.cospar-assembly.org/.

FEATURE



202 The Challenges and Joys of Mapping America's Last Frontier

An interview with Dr. Dave Maune, Project Manager for Alaska Statewide IfSAR Mapping

PEER-REVIEWED ARTICLES

215 Satellite-Imagery Geometric Accuracy Improvement Based on Direct Correction of Dominant Coefficients

Xinming Tang, Changru Liu, Ping Zhou, Ning Cao, Fengxiang Li, and Xia Wang

An important and difficult point in the application of satellite imagery is refining the positioning model and improving the geometric accuracy. In this article, we focus on improvement in geometric accuracy and develop a new rational function model (RFM) refinement method.

225 Temporal Validation of Four LAI Products over Grasslands in the Northeastern Tibetan Plateau

Gaofei Yin, Ainong Li, Zhengjian Zhang, and Guangbin Lei

Time series of leaf area index (LAI) products are now widely used, and the temporal validation is the prerequisite for their proper application. However, a systematical comparison between different products using both direct and indirect methods is still lacking. The objective of this paper is to assess and compare the temporal performances of four LAI products: Moderate Resolution Imaging Spectroradiometer (MODIS) LAI (MOD15A2, MOD15A2h, Geoland2 Version 1 (GEOV1), and Global Land Surface Satellite (GLASS).

235 Building Extraction from High-Resolution Remote Sensing Images Based on GrabCut with Automatic Selection of Foreground and Background Samples

Ka Zhang, Hui Chen, Wen Xiao, Yehua Sheng, Dong Su, and Pengbo Wang

This article proposes a new building extraction method from high-resolution remote sensing images, based on GrabCut, which can automatically select foreground and background samples under the constraints of building elevation contour lines.

247 Topographic and Geomorphological Mapping and Analysis of the Chang'E-4 Landing Site on the Far Side of the Moon

Bo Wu, Fei Li, Han Hu, Yang Zhao, Yiran Wang, Peipei Xiao, Yuan Li, Wai Chung Liu, Long Chen, Xuming Ge, Mei Yang, Yingqiao Xu, Qing Ye, Xueying Wu, and He Zhang

The Chinese lunar probe Chang'E-4 successfully landed in the Von Kármán crater on the far side of the Moon. This article presents the topographic and geomorphological mapping and their joint analysis for selecting the Chang'E-4 landing site in the Von Kármán crater.



211 In Memoriam—Hans J. Wehrli

COLUMNS

209 GIS Tips & Tricks

ANNOUNCEMENTS

201 High-Accuracy UAS Mapping Workshop

208 Geospatial Revolution

212 2020 William T. Pecora Award Nominations

213 New ASPRS Members

Join us in welcoming our newest members to ASPRS.

214 *PE&RS* Call for Submissions—Optical Polarization Remote Sensing & Photogrammetry

DEPARTMENTS

198 Industry News

198 Calendar

234 Who's Who in ASPRS

259 ASPRS Sustaining Members

260 ASPRS Media Kit

See the Cover Description on Page 200

COVER DESCRIPTION

The United States purchased Alaska from Russia in 1867 for \$7.2M. Alaska became a state in 1959 and has vast natural resources that remain largely unexplored today. Alaska was never mapped to National Map Accuracy Standards and has never had statewide digital orthophotos -- common in every other state. Why, you ask? Even today, there are very few photo-identifiable control points in a large state that spreads over 10 UTM zones; GPS hadn't been invented yet in the 1960s to survey in remote areas, many of which are inaccessible; for decades, we didn't have cloud free aerial or satellite imagery in many areas because of persistent cloud cover; and modern aerial triangulation techniques had not been invented yet. It was no surprise to learn that some mountains in the National Elevation Dataset had been mapped a mile away from their correct location, so attempts to produce orthophotos resulted in streams that appeared to flow over hills rather than through the valleys.

In 1884, John Wesley Powell, 2nd Director of the U.S. Geological Survey (USGS), in his testimony to Congress, stated: "A Government cannot do any scientific work of more value to the people at large, than by causing the construction of proper topographic maps of the country." That statement is as true today as it was in 1884.

In 2008, the Alaska Statewide Digital Mapping Initiative (SDMI) hired Dewberry Engineers to prepare the *Alaska DEM Whitepaper* that recommended aerial IfSAR (which maps through clouds) for statewide mapping at mid-accuracy. Dewberry was selected to write this whitepaper because it had edited and authored the ASPRS textbook: *Digital Elevation Model Technologies and Applications: The DEM Users Manual* that provided guidance on the need to establish user requirements, accompanied by chapters explaining the advantages and disadvantages of photogrammetry, IfSAR, topographic and bathymetric lidar, and sonar for mapping of elevations from the tops of the mountains to the depths of the waters. Dewberry stressed the fact that the topographic layer is foundational and must be correct in order for other mapping layers to fit together in compliance with accuracy standards

In 2009, Dewberry prepared the *Alaska DEM Funding and Implementation Plan* on how to pay for statewide IfSAR mapping by cost sharing among stakeholders. Between 2010 and 2020, as a USGS prime contractor, Dewberry subcontracted with Fugro EarthData and Intermap Technologies to produce hydro-enforced DTMs and DSMs and Ortho-rectified Radar Imagery (ORIs), with QA/QC checkpoints surveyed by JOA Surveys. Dewberry performed all management and QA/QC. Dewberry also subcontracted with CompassData to survey the official elevation of Denali (20,310 ft.) with GPS and to survey the depth of the ice and snow on Denali's peak (6.1 meters) using ground penetrating radar (GPR).

The IfSAR mapping was paid for by USGS, the state of Alaska, and other federal stakeholders, and cost \$67.3M to complete in 2020. Statewide US Topo maps and digital orthophotos will be available from USGS in 2021.

The front cover, from Intermap Technologies, compares the hydro-rich IfSAR DTM (top) with the prior DTM from the NED (bottom) for a portion of the Kuskokwim River. The accompanying highlight article summarizes the challenges and joys of mapping America's Last Frontier. The article includes several quotes from Kevin Gallagher, USGS Associate Director, Core Science Systems, who provides great insights into the value of this mapping program now, and over the next 20, 30 or 50 years.



PHOTOGRAMMETRIC ENGINEERING & REMOTE SENSING

JOURNAL STAFF

Publisher ASPRS
Editor-In-Chief Alper Yilmaz
Assistant Editor Jie Shan
Assistant Director — Publications Rae Kelley
Electronic Publications Manager/Graphic Artist
Matthew Austin

Photogrammetric Engineering & Remote Sensing is the official journal of the American Society for Photogrammetry and Remote Sensing. It is devoted to the exchange of ideas and information about the applications of photogrammetry, remote sensing, and geographic information systems. The technical activities of the Society are conducted through the following Technical Divisions: Geographic Information Systems, Photogrammetric Applications, Lidar, Primary Data Acquisition, Professional Practice, and Remote Sensing Applications. Additional information on the functioning of the Technical Divisions and the Society can be found in the Yearbook issue of *PE&RS*.

Correspondence relating to all business and editorial matters pertaining to this and other Society publications should be directed to the American Society for Photogrammetry and Remote Sensing, 425 Barlow Place, Suite 210, Bethesda, Maryland 20814-2144, including inquiries, memberships, back issues, changes in address, manuscripts for publication, advertising, subscriptions, and publications. The telephone number of the Society Headquarters is 301-493-0290; the fax number is 225-408-4422; web address is www.asprs.org.

PE&RS. *PE&RS* (ISSN0099-1112) is published monthly by the American Society for Photogrammetry and Remote Sensing, 425 Barlow Place, Suite 210, Bethesda, Maryland 20814-2144. Periodicals postage paid at Bethesda, Maryland and at additional mailing offices.

SUBSCRIPTION. For the 2020 subscription year, ASPRS is offering two options to our *PE&RS* subscribers — an e-Subscription and the print edition. E-subscribers can plus-up their subscriptions with printed copies for a small additional charge. Print and Electronic subscriptions are on a calendar-year basis that runs from January through December. We recommend that customers who choose both e-Subscription and print (e-Subscription + Print) renew on a calendar-year basis.

The rate of the e-Subscription (digital) Site License Only for USA and Non-USA is \$1000.00 USD. e-Subscription (digital) Site License Only for Canada* is \$1049.00 USD. e-Subscription (digital) Plus Print for USA is \$1365.00 USD. e-Subscription (digital) Plus Print for Canada* is \$1424.00 USD. e-Subscription (digital) Plus Print for Non-USA is \$1395.00 USD. Printed-Subscription Only for USA is \$1065.00 USD. Printed-Subscription Only for Canada* is \$1124.00 USD. Printed-Subscription Only for Non-USA is \$1195.00 USD. *Note: e-Subscription/Printed-Subscription Only/e-Subscription Plus Print for Canada include 5% of the total amount for Canada's Goods and Services Tax (GST #135123065). **PLEASE NOTE: All Subscription Agencies receive a 20.00 USD discount.**

POSTMASTER. Send address changes to *PE&RS*, ASPRS Headquarters, 425 Barlow Place, Suite 210, Bethesda, Maryland 20814-2144. CDN CPM #40020812

MEMBERSHIP. Membership is open to any person actively engaged in the practice of photogrammetry, photointerpretation, remote sensing and geographic information systems; or who by means of education or profession is interested in the application or development of these arts and sciences. Membership is for one year, with renewal based on the anniversary date of the month joined. Membership Dues include a 12-month electronic subscription to *PE&RS*. Or you can receive the print copy of *PE&RS* Journal which is available to all member types for an additional fee of \$60.00 USD for shipping USA, \$65.00 USD for Canada, or \$75.00 USD for international shipping. Dues for ASPRS Members outside of the U.S. will now be the same as for members residing in the U.S. Annual dues for Regular members (Active Member) is \$150.00 USD; for Student members \$50.00 USD for USA and Canada \$58.00 USD; \$60.00 USD for Other Foreign members. A tax of 5% for Canada's Goods and Service Tax (GST #135123065) is applied to all members residing in Canada.

COPYRIGHT 2020. Copyright by the American Society for Photogrammetry and Remote Sensing. Reproduction of this issue or any part thereof (except short quotations for use in preparing technical and scientific papers) may be made only after obtaining the specific approval of the Managing Editor. The Society is not responsible for any statements made or opinions expressed in technical papers, advertisements, or other portions of this publication. Printed in the United States of America.

PERMISSION TO PHOTOCOPY. The appearance of the code at the bottom of the first page of an article in this journal indicates the copyright owner's consent that copies of the article may be made for personal or internal use or for the personal or internal use of specific clients. This consent is given on the condition, however, that the copier pay the stated per copy fee of 3.00 USD through the Copyright Clearance Center, Inc., 222 Rosewood Drive, Danvers, Massachusetts 01923, for copying beyond that permitted by Sections 107 or 108 of the U.S. Copyright Law. This consent does not extend to other kinds of copying, such as copying for general distribution, for advertising or promotional purposes, for creating new collective works, or for resale.

Be a part of ASPRS Social Media:

 facebook.com/ASPRS.org

 linkedin.com/groups/2745128/profile

 twitter.com/ASPRSorg

 youtube.com/user/ASPRS

HIGH-ACCURACY UAS MAPPING WORKSHOP

Standards, Principles, and Best Practices

WHAT YOU'LL LEARN

- How do professionals assure the quality and accuracy of their results?
- What is photogrammetry and why is it important?
- What are best practices for mapping with drone imagery in a variety of use cases?
- When should you use your drone-based lidar?
- What are best practices for mapping with drone lidar in a variety of use cases?
- What circumstances favor mapping with drones over conventional platforms?

Brought to you by:



AUVSI XPONENTIAL

May 4 - 7, 2020 | Boston, MA

Are you frustrated by not achieving the results your surveyor or engineering client expects, despite your investment in drone technology? If you are like many entrepreneurs in this industry, you started with a drone and a basic camera and ran into problems with hardware performance, digital product accuracy, and lack of good data in areas of heavy vegetation.

To learn basic principles and to avoid missing out on the latest technology advances, you may benefit from having someone explain system design, best practices, and quality control processes step-by-step, in simple terms, without a lot of equations and complicated jargon.

The ASPRS High-Accuracy UAS Mapping Workshop provides you the opportunity to hear from geospatial professionals with years of practical experience who are now working on the “bleeding edge”, using UAS to produce accurate products that meet client expectations.

ASPRS has been leading the world for over 80 years, advancing standards in photogrammetry, mapping and remote sensing and providing certification for practitioners who have the right skills and a proven track record. ASPRS can help you achieve the results you and your clients are looking for.

DISCOVER ALL THE DETAILS

<https://conferences.asprs.org/AUVSI-2020>

The Challenges and Joys of Mapping America's Last Frontier



**An interview with Dr. Dave Maune,
Project Manager for Alaska Statewide
IfSAR Mapping**

“Why was Alaska never previously mapped to National Map Accuracy Standards?”

Although all other states had USGS 1:24,000-scale topographic quad maps produced to National Map Accuracy Standards (NMAS) as well as large-scale orthophotos refreshed every few years to modern digital mapping standards, Alaska has never had statewide orthophotos, and its 1:63,360-scale topo quad maps from USGS did not satisfy NMAS for several reasons: (1) lack of cloud-free stereo imagery; (2) lack of photo-identifiable ground control; and (3) because photogrammetric block triangulation and GPS technologies hadn't been invented yet when USGS produced Alaska's quad maps many decades ago. Recent attempts to produce digital orthophotos by draping satellite imagery over DEMs from the National Elevation Dataset (NED) failed because the NED was too inaccurate to support orthorectification, as demonstrated by Figure 1.

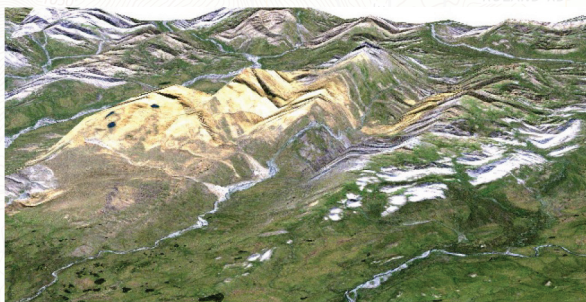


Figure 1. The NED's low-res 60m DEM had horizontal errors as large as one mile in the Brooks Range, shown here. When draping satellite imagery over a DEM from the NED, some rivers flowed uphill and not through valleys as they should. Image courtesy of UAF GINA.

Figure 2. Looking up at Denali (20,310 ft.) from the base camp at 7,000 ft. from which 4 surveyors traversed ~83 miles horizontally and climbed ~6 miles vertically (including back-and-forth caching) while carrying over 700 pounds of equipment each year to the peak to perform GPS & GPS surveys in 2015 and 2016. Image courtesy of CompassData.



“A Government cannot do any scientific work of more value to the people at large, than by causing the construction of proper topographic maps of the country,” by John Wesley Powell, 2nd Director of USGS, in his testimony to Congress on December 5, 1884.”

“What were your initial challenges?”

Despite the logistical challenges in GPS surveying IfSAR prism reflectors and QA/QC checkpoints throughout vast remote areas of Alaska, the Dewberry team knew that we could do the job technically, but we didn't know how much it would cost or who would pay for it. I authored the Alaska DEM Funding & Implementation Plan that recommended cost sharing among multiple federal and state stakeholders, and Dewberry worked with its two IfSAR subcontractors to submit a technical proposal to USGS. We estimated it would cost \$77.3M to map Alaska over a 2-year period, with Fugro EarthData mapping the most-difficult 23% of the state using its GeoSAR system, and Intermap Technologies mapping the less-difficult 77% of the state using its (three) STAR systems. Fugro's perceived advantage was that the GeoSAR included both X-band and P-band; combined with GeoSAR's lidar profiler, the P-band should be better able to map DTMs through dense forests, but Fugro did not have a mature production line for doing this. Intermap's advantage was that it had produced NEXTMap®Europe, NEXTMap®Britain, and NEXTMap®USA over 49 states; it had a mature production line for delivering standard products that exceeded USGS specifications for mid-accuracy DEMs, even though it used algorithms to estimate vegetation heights for production of DTMs from X-band IfSAR that maps top reflective surfaces (DSMs).

“Why was Dewberry selected to solve Alaska mapping problems?”

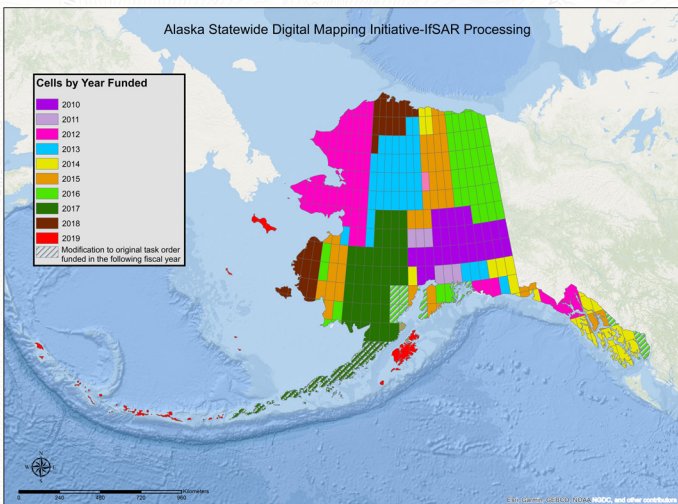
At the Alaska Surveying and Mapping Conference in 2008, I used ASPRS' DEM Users Manual (that I authored/edit-ed) as a reference, explaining why the topographic layer is foundational for producing orthoimagery and other mapping layers. The DEM Users Manual explained the need for establishing DEM requirements first -- prior to deciding what DEM technology to use. Alaska then hired Dewberry to produce the Alaska DEM Whitepaper. Contrary to my lidar recommendations elsewhere, the Alaska DEM Whitepaper recommended aerial IfSAR statewide for Alaska because our requirements analysis indicated that DSMs and DTMs with 20' contour accuracy satisfied known statewide requirements, including immediate aerial navigation and safety requirements of the Federal Aviation Administration (FAA), and because IfSAR could meet this requirement while mapping through persistent clouds. Alaska then asked USGS to contract with Dewberry to execute statewide IfSAR mapping under its USGS GPSC contract.

Photogrammetric Engineering & Remote Sensing
Vol. 86, No. 4, April 2020, pp. 202–207.
0099-1112/20/202–207

© 2020 American Society for Photogrammetry
and Remote Sensing
doi: 10.14358/PERS.86.4.202

“What challenges did you face once you received funded task orders?”

We first needed to develop consensus on standards, specifications, priorities and deliverables. Dewberry provided overall project management and rigorous QA/QC, using checkpoints from JOA Surveys. Data were delivered in the Alaska Albers projection, then converted to multiple file formats for USGS and NGA. Elevation data was delivered in both orthometric and ellipsoid heights, using Geoid09 throughout for consistency. Intermap’s Ortho-rectified Radar Images (ORIs) had 62.5-cm resolution, whereas Fugro’s ORIs had 2.5-meter resolution – both better than USGS’ 5-meter resolution requirement. Fugro delivered hydro-enforced DSMs and DTMs that met USGS’ hydro specifications whereas Intermap’s standard hydro masks exceeded USGS specifications for lakes and double-line streams. USGS received data that exceeded specifications, but this caused edge-join issues and inconsistencies along seam lines between the two firms. Mapping the easier terrain, Intermap routinely exceeded accuracy specifications whereas Fugro struggled to satisfy accuracy requirements partly because the P-band didn’t just penetrate vegetation, but sometimes also penetrated the ground, depending on soil wetness. Fugro developed an X-band/P-band hybrid model for DTMs, but some issues remained. GeoSAR appeared to lower Denali’s peak elevation by 60+ feet, possibly from IfSAR foreshortening, shadow or layover. This caused Dewberry to launch two expeditions to climb Denali in 2015 to GPS survey the official elevation of the top of the ice and snow (at 20,310 ft), returning in 2016 to install a USGS survey monument at Windy Corner and to use ground penetrating radar (GPR) to measure the 6.1-meter depth of ice and snow on the peak. Both years, Blaine Horner of CompassData led 4-person teams that carried equipment loads of over 700 pounds from their base camp at 7,000’, to the peak, under extremely difficult conditions.



In addition to these technical and logistical challenges, USGS lacked the funding necessary to acquire the data efficiently in large contiguous blocks over a 2-year acquisition period. Instead, as funds became available from diverse stakeholders, funding was received in piecemeal fashion for smaller blocks each year between 2010 and 2019 (see Figure 3) for annual project areas. By the time funds were available in 2019 for mapping of Kodiak Island which we had planned to map with GeoSAR (because of the rugged terrain and dense forests), GeoSAR had already been retired from service by Fugro and was no longer operating commercially. Intermap did the best they could to map Kodiak Island with X-band IfSAR only.

Because funds were received so erratically in small, inefficient acquisition blocks, members of the Dewberry team acquired much data on speculation, taking financial risks and not knowing whether they would ever be paid.

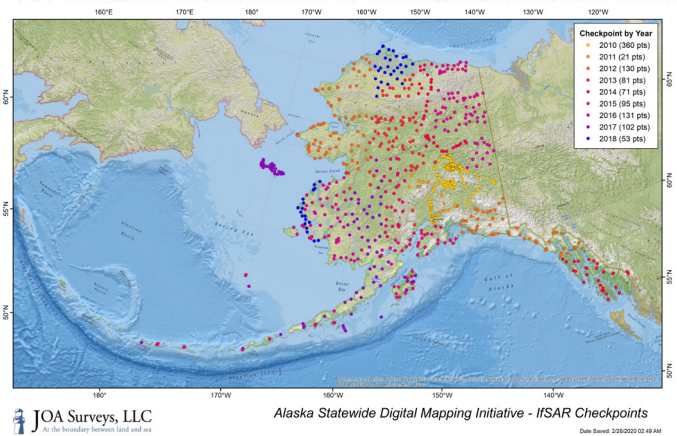


Figure 5. JOA Surveys efficiently surveyed 1,044 QA/QC checkpoints in remote terrain within each of the cells mapped by Intermap and Fugro.

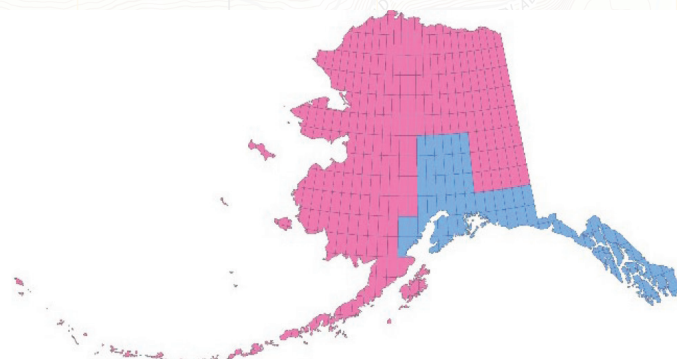


Figure 4. Intermap efficiently mapped all Alaska 1-degree cells shown in pink, and Fugro efficiently mapped all cells shown in blue.

Figure 3. Rather than being funded efficiently for large contiguous blocks in two years, small non-contiguous blocks were mapped each year between 2010 and 2019 as funds became available from different stakeholders. This also impacted Dewberry’s ability to efficiently acquire annual QA/QC checkpoints in advance of accuracy testing.

“What are your greatest joys, now that the project is complete?”

My biggest joy is that we successfully mapped all of Alaska, consistently meeting or exceeding USGS’ specifications, at a total cost of \$66.3M, rather than the \$77.3M originally estimated. This is a tribute to cost efficiencies by all involved.

My second joy is knowing the vast improvement in usability of IfSAR DEMs compared to the prior DEMs from the NED.

- In preparing the initial Alaska DEM Whitepaper, I learned of the importance of hydro features to Alaskans. Figure 6 (courtesy of Intermap) shows the richness of the hydro features from IfSAR, compared with sparse hydro features in the NED. Hydro-enforced IfSAR DTMs are now being used to update National Hydrography Data-sets (NHD) throughout Alaska.
- I also learned of the importance of being able to map through clouds and produce digital orthoimages. Figure 7 shows how higher-resolution greyscale IfSAR ORIs can be used to pan-sharpen lower-resolution color satellite imagery; and Figure 8 demonstrates how IfSAR ORIs can be used to produce color orthophotos, even when satellite images are cloudy.

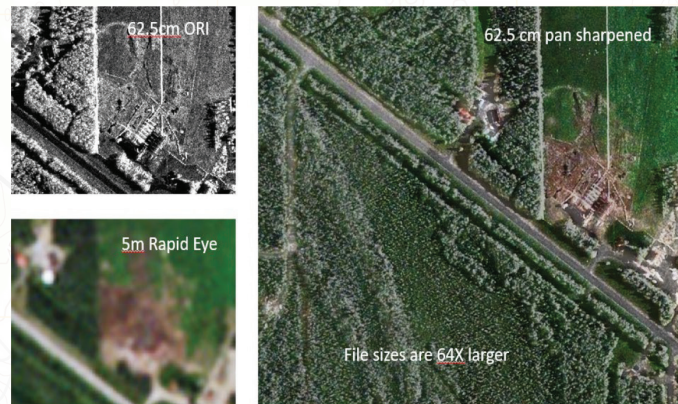


Figure 7. This figure demonstrates how to pan-sharpen 5m color satellite imagery with 62.5-cm greyscale IfSAR ORIs.

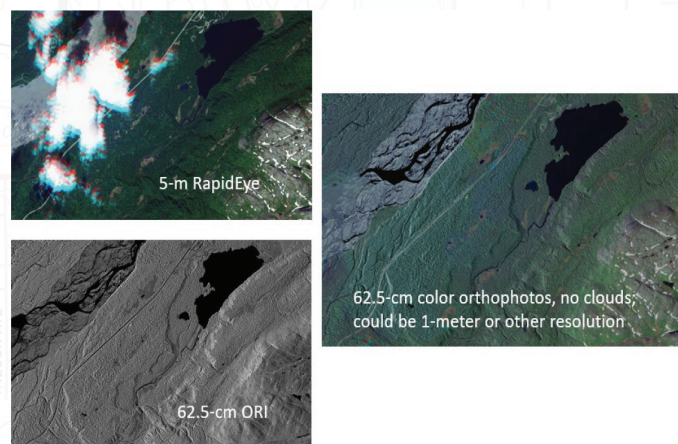
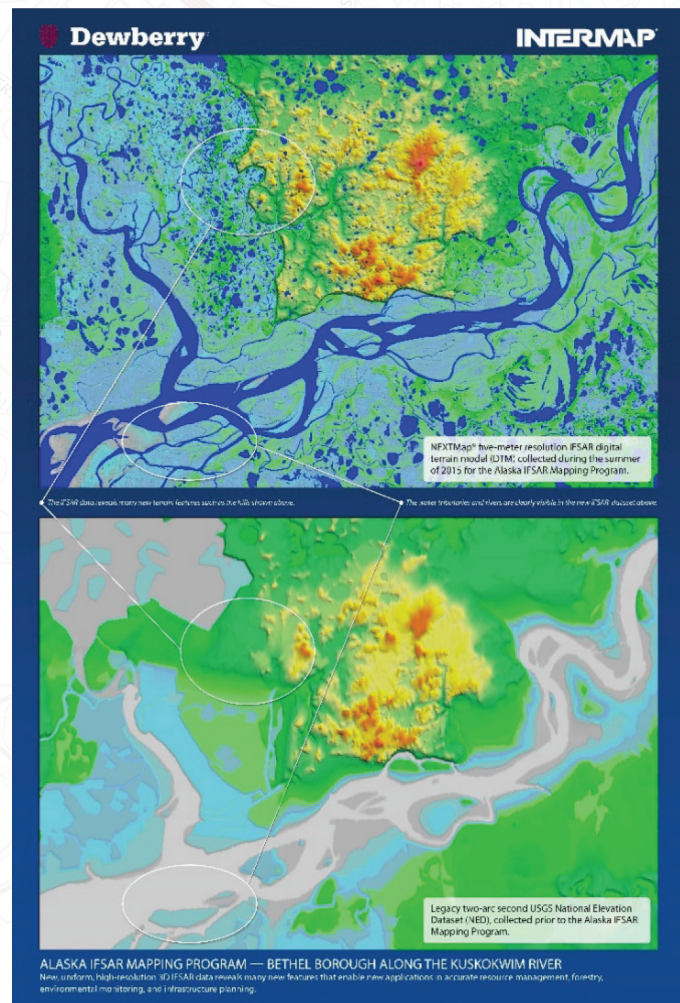


Figure 8. This figure demonstrates how IfSAR ORIs can be used to pan-sharpen cloudy satellite imagery – mapping through the clouds.



“The detailed mapping of elevation in the State of Alaska significantly improves the economy, quality of life and safety of our largest State. It satisfied needs for flood modeling, flight safety, precision forestry, landslide modeling, critical minerals assessments, natural resource assessments, and transportation and infrastructure development. And while the data that has been collected has significant value today, it will be even more valuable 20, 30 or 50 years from now as it will provide a baseline for which changes can be measured. For example, changes in shoreline, glacial mass, subsidence and hydrologic regime. It raises Alaska to the modern mapping standard and it opens the door for the next chapter in the future of Alaska, a future that recognizes Alaska as a natural resource wonder, a thriving economy and strategic national security interest.” By Kevin T. Gallagher, USGS Associate Director, Core Science Systems.

Figure 6. Aerial IfSAR (top) of Kuskokwim River compared with the prior NED (bottom). IfSAR hydro features are extremely rich.

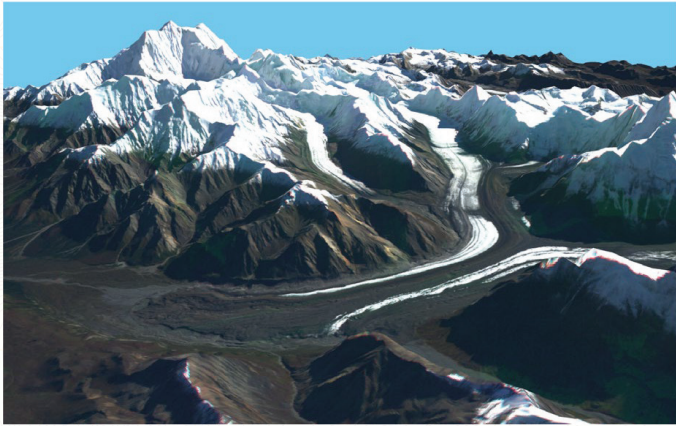


Figure 9. This is a satellite image draped over the IfSAR DTM of Mt. Hayes, then viewed from a perspective selected by Dewberry. Compare this image with Figure 1 to see the vast improvements.



Figure 10. The top image shows a satellite image draped over the IfSAR DTM of Denali's peak. The lower image shows a Denali fly-by photograph taken by E-Terra. The similarity is remarkable.

My third joy is in finding that everything now fits when draping satellite imagery over IfSAR DTMs. See Figures 9 and 10.

My fourth joy is exhilaration received from Blaine Horner's two mountaineering expeditions to perform GPS and GPR surveys to officially survey Denali's elevation at 20,310 ft and the depth of the ice/snow at 6.1 meters. Whereas many have died attempting to climb Denali with no extra heavy burden to carry, Blaine Horner's two teams, shown in Figures 11 and 12, carried over 700 pounds of car batteries, power tools and other heavy equipment both years to the top. During his 2016 expedition, Blaine even won NPS' Mislow-Swanson Denali Pro Award for saving the lives of two badly injured European climbers.

My fifth joy is knowing the 7.5-minute 1:25,000-scale US Topo map series of Alaska, to include statewide orthoimagery, will be completed in 2021 (Figures 14 and 15 courtesy of USGS). With IfSAR completed in 2020, USGS will acquire commercial satellite imagery in 2021 for orthorectification to the IfSAR. The Dewberry team is proud of its accomplishments in providing the accurate topographic foundational layer to which other layers now fit. (Figure 16).

Figure 14. US Topo of Juneau with shaded relief turned on.



Figure 11. Blaine Horner (left) with Rhett Foster, Udi Karriere and Tom Heinrichs prior to flying to the Base Camp at 7,000' for their climb to GPS survey Denali's peak in 2015.



Figure 12. Kristen Schild (left) with husband Seth Campbell, Patrick Saylor and Blaine Horner at the Base Camp prior to their climb to GPR survey the ice/snow depth on Denali's peak in 2016.



Figure 13. In 2016, Blaine Horner installed and surveyed a USGS survey marker at Windy Corner and then rescued two badly injured European climbers who had fallen.

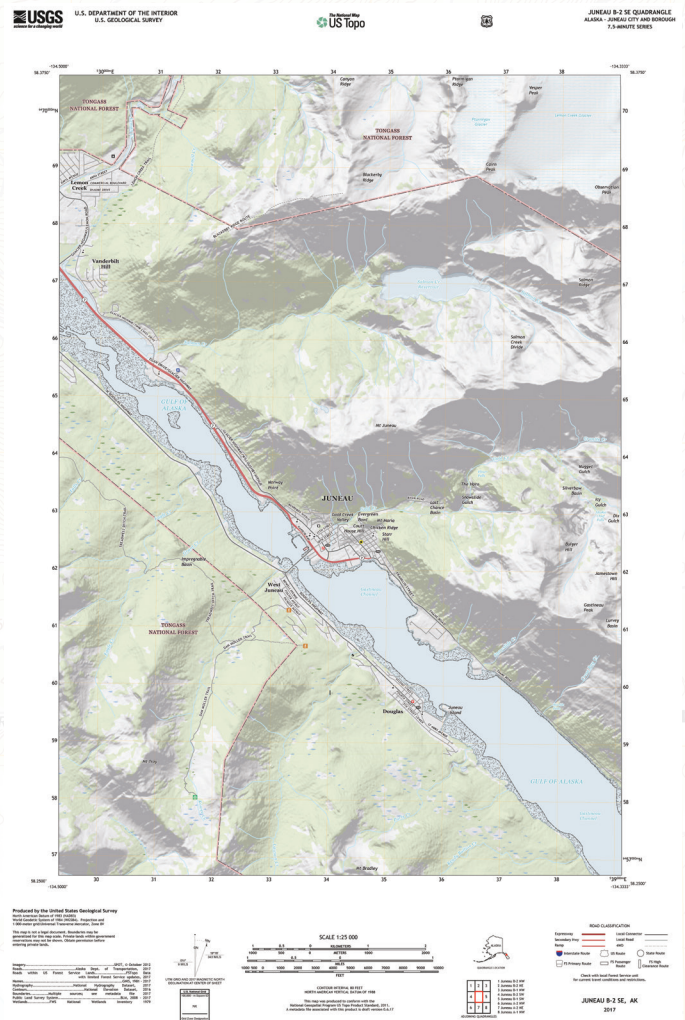




Figure 15. Glaciated US Topo with orthoimagery layer turned on.

"This data and information is provided to the world, license-free, in the public domain, for its use and application in all areas previously mentioned as well as recreation and scientific research. These maps are easily downloaded electronically and used for a wide variety of applications from recreational, to city planning, to emergency response. Lastly, data layers such as hydrography, roads, trails, boundaries and other data layers will be enhanced because of the new, more detailed elevation data." By Kevin T. Gallagher, USGS.



Figure 17. Lt Gov Mead Treadwell briefing the Alaska Mapping Roundtable on June 28, 2012 in Washington D.C. Image courtesy of USGS.

Lastly, it gives me great joy that America's Last Frontier was mapped with such outstanding teamwork, not just by the Dewberry team but by numerous federal and state stakeholders. In addition to organizing Skybreaking events that showcased the SAR aircraft and technology, Nick Mastrodicasa of AK DOTPF arranged for OMB and over 20 other federal agencies to meet for the first Alaska Mapping Roundtable in Washington, D.C. in 2012 (Figure 17). After briefings by Alaska's Lt Gov Mead Treadwell, Dave Maune, Nick Mastrodicasa and briefers from USGS, agency executives unanimously agreed on the urgent need for accurate mapping of Alaska which holds major natural resources and is becoming more vital each year as marine navigation routes are opening through the Arctic and as the search expands for mining of critical minerals for USGS' Earth Mapping Resources Initiative (Earth MRI). Ultimately, \$66.3M in funding was received from USGS, the State of Alaska, NRCS, BLM, NPS, DOD, USFS, and FWS. Senator Lisa Murkowski led the effort to obtain needed funding at the federal level. Project success can be attributed to collaboration by all involved. This was a total team effort and its major reason for success.

Dr. Dave Maune, is an Associate Vice President at Dewberry Engineers,



Inc., headquartered in Fairfax, Virginia, with more than 50 locations and 2,000+ professionals nationwide. Dave is best known as the editor and principal author of all three editions of The DEM Users Manual published by ASPRS in 2001, 2007 and 2018, and as the author of the National Enhanced Elevation Assessment (NEEA) that provided the blueprint for USGS' 3D Elevation Program (3DEP) based on QL5 IfSAR of Alaska and QL2 lidar elsewhere in the U.S. Dewberry is a full-service A/E firm that specializes in geospatial technologies, products and services, including remote sensing data acquisition and processing, data analytics, digital orthophotography, emergency response, geospatial benefit-cost analyses, GIS, topographic and hydrographic mapping and surveying, and independent QA/QC of geospatial data provided by others.

Proudly Mapping America's Last Frontier

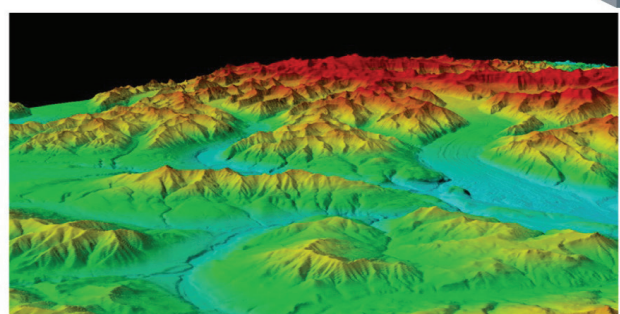
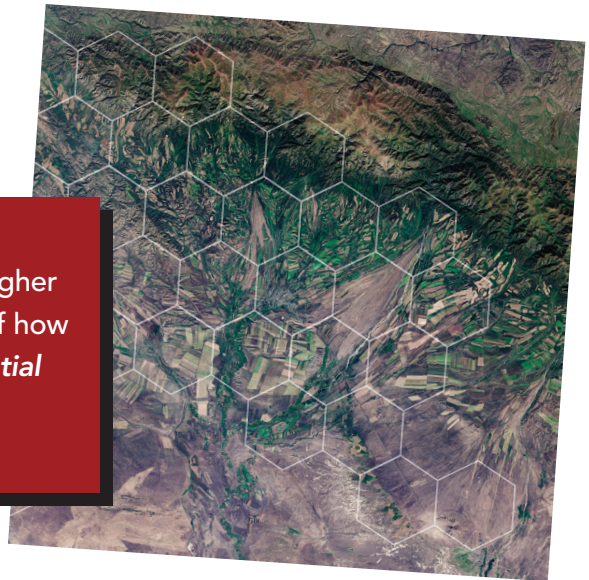


Figure 16. the proud Dewberry team includes Fugro, Intermap, JOA Surveys and CompassData.

GEOSPATIAL REVOLUTION

With more than 1 million video views, the *Geospatial Revolution Project* is the go-to source for government, higher education, and workforce development for an overview of how geospatial technology is changing the world. The *Geospatial Revolution Project* is anchored in a world-class research university and trusted for its PBS editorial standards.



THE NEXT GENERATION

WPSU Penn State is celebrating the 10th Anniversary (2010-2020) of the launch of the original *Geospatial Revolution Project* with a new video episode about next-generation innovations in geospatial technology.

Our Emmy Award-winning production team explores stories from public safety, business, and national defense. The real revolution in geospatial technologies is just beginning!



AUDIENCES & DISTRIBUTION

The new episode—with ready-made *Geospatial Revolution* audiences in government, public safety, industry, education, and the general public—will be screened at conferences, posted to social media, linked to the original project website, and shared with original engagement partners:

- U.S. government (e.g., U.S. DOD, NGA, FBI, U.S. Army Corps of Engineers)
- Higher education/workforce development collaborators
- K-12 STEM education

CONTACT

Please make a philanthropic gift to WPSU Penn State to support the new episode. *For more information, contact:*

Elaine Brzycki
Project Development
WPSU Penn State
ejb23@psu.edu

Kristian Berg
Director, *Geospatial Revolution Project*
WPSU Penn State
kjb35@psu.edu

Dr. Todd S. Bacastow
Teaching Professor
Dept. of Geography • Penn State
tsb4@psu.edu

Karen Schuckman
Associate Teaching Professor
Dept. of Geography • Penn State
kls505@psu.edu

“Geospatial Revolution is considered the ‘Bible’ of the GIS field. I can’t wait to see the next episode!”

– Dr. Salvatore Amaduzzi
University of Udine, Italy



GEOSPATIAL REVOLUTION
geospatialrevolution.psu.edu

This publication is available in alternative media on request. Penn State is committed to affirmative action, equal opportunity, and the diversity of its workforce. Copyright © 2020 The Pennsylvania State University

Looking for Topographic Terrain or Bathymetric Lidar Data? Look to the NOAA Digital Coast

It was over 10 years ago, in 2007, that the US Geological Survey (USGS), the National Aeronautics and Space Administration (NASA), and the Association of America State Geologists (AASG) cited the need for a national lidar (light detection and ranging) dataset (Stoker, 2007). In the years since the inception of the USGS 3D Elevation Program in 2012, the USGS, in cooperative projects with federal, state and local agencies, has funded the collection of over 2 million ASPRS LAS tiles; that equates to approximately 12 trillion lidar point cloud records and not to mention the IfSAR data collected for Alaska. (<https://www.usgs.gov/core-science-systems/ngp/3dep/3dep-data-acquisition-status-maps>). Since 1999, the National Oceanographic and Atmospheric Administration (NOAA), through the Digital Coast Partnership has been collecting and distributing lidar data. The lidar (and derived products) are available from several sources. Without getting too much into the weeds regarding the technical aspects, here is my favorite source.

The NOAA Digital Coast Data Section (<https://coast.noaa.gov/digitalcoast/data/>) stores and distributes lidar (and other) data sets for coastal states (note: if you know that you are only looking for lidar data, you can go directly to the Digital Coast Data Access Viewer (DAV) and bypass the other data available (<https://coast.noaa.gov/dataviewer/##/lidar/search/>)). The lidar data are searchable through either a geo-interface, i.e. draw a box and the search returns available datasets, or through a simple two parameter (what type of data are you searching for, and where in the US) search interface. Alternatively, you can browse through the available datasets (Elevation, Land Cover, Weather/Climate, Imagery, and Economics/Demographics) by category.

In this example, I chose to find “lidar” data (Find box) near “Pittsburgh, PA, USA” (Near box) and the search returned three (3) datasets.

One of the nice features of this search utility is that you can preview the geographic extent of the dataset (Preview) and read the Metadata (Metadata button) before you go to the Download button to get the data.

2006-2008 PAMAP Lidar: Statewide (South)

Providers

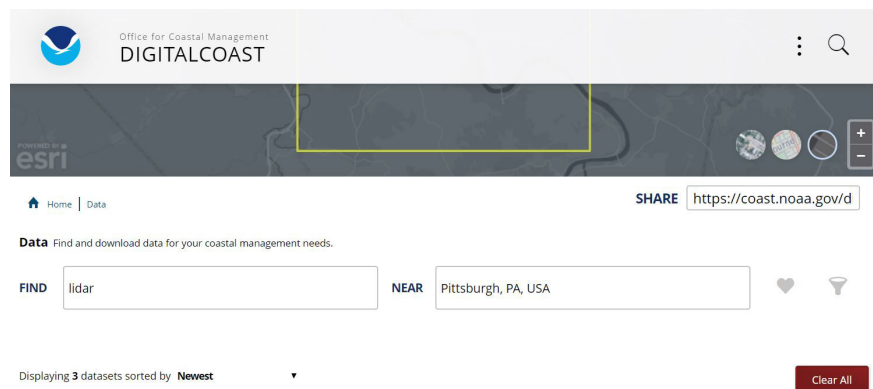
Pennsylvania Department of Conservation and Natural Resources

Download Metadata Preview

Finally, when you go to the Download button and click on “Custom Download” you get a map in a new window showing the footprint of the dataset. You can zoom/pan to find your area of interest, and use the “Draw Search Area” tool (pencil draws a box), or enter an address, or enter the Lat/Lon to find the data.



Once you have completed the search, to download the data, put it into your cart and select, from dropdown choices, the Projection & Datum, Geoid Model (in Advanced options), Output options (points, rasters, derived products such as contours and/or intensity images) and file format (LAS, LAZ, ASCII). Enter you e-mail address, review your order, and wait. You will receive your “order number” and confirmation for your order on the last screen.



Photogrammetric Engineering &
Remote Sensing
Vol. 86, No. 4, April 2020, pp. 209–211.
0099-1112/20/209–211
© 2020 American Society for
Photogrammetry and Remote Sensing
doi: 10.14358/PERS.86.4.209

Digital Coast Data Access Viewer

NATIONAL OCEANIC AND ATMOSPHERIC ADMINISTRATION



Status of Request: 335826

Submitted: 2019-12-03 12:38

Status: **Data jobs queued or being processed**

Details: The data jobs associated with this request are being or will soon be processed. Please check the status of the individual data jobs for details. Besides, a confirmation message containing a list of data jobs has been sent to the user, along with a link for the user to check the status or progress of the data jobs.

Data Jobs (1)

Job ID	Data Set	Output Options	Status
504427	2006-2008 PAMAP Lidar: Statewide (South)	Projection: State Plane 1983, Zone: Zone 3702 Pennsylvania South, Horizontal Datum: NAD83, Horizontal Units: U.S. Feet, Vertical Datum: NAVD88, Vertical Units: U.S. Feet, File Format: LAZ, Data Classification: Any Points, Data Returns: Any Points, Ancillary Data: No Ancillary Data, Geoid Name: GEOID18	Job is being processed. The processing of the job was started at 2019-12-03 12:43 and may take about 51 minutes to finish.

[Refresh Request Status](#) [View All Requests](#)

[United States Department of Commerce](#) | [National Oceanic and Atmospheric Administration](#)

[Contact Us](#) | [Privacy Policy](#) | [Link Disclaimer](#) | [USA.gov](#)

You should receive an e-mail message within a few minutes with confirmation of your order and a link to check on the status and progress of your data request. Clicking the link will return a page like the image displayed above.

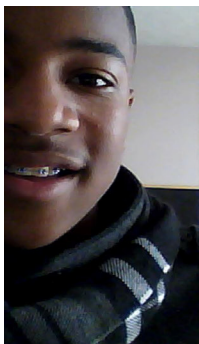
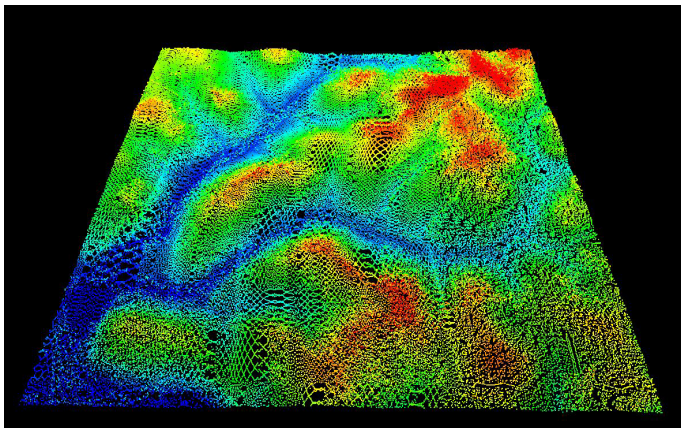
When the data are ready for download (you get a hint of how long it will take), you will get another message with a link to download the file. I specified the complete point cloud in LAZ format (to shorten the download time). Download the file (your data will be available for 10 calendar days), decompress (if your software requires a LAS file) using a LASzip utility (<https://rapidlasso.com/laszip/>) and you are ready to go.

One word of clarification, the NOAA Digital Coast Data Viewer is not the same as the US National Map (see below). Although there are some overlapping datasets, the NOAA DAV has been focusing on distributing data since 1999 and generally limits coverage to coastal states. Another difference is that the NOAA DAV distributes both topobathymetric and bathymetric lidar data which are not a part of the 3DEP. For more tips on using the DAV, there is a GeoZone blog (<https://geozoneblog.wordpress.com>) and search for “DAV” or “DAV Tips”.

Just a final note, another great source of terrain data products is the US National Map Download (<https://viewer.nationalmap.gov/basic/>). Lidar point cloud data are available for a fee through the Amazon Public Dataset (<https://www.usgs.gov/news/usgs-3dep-lidar-point-cloud-now-available-amazon-public-dataset>).

Stoker, J. 2007. The need for a national LIDAR dataset. *PE&RS*. 74:1066-1068.

Al Karlin, Ph.D., CMS-L, GISP is with Dewberry's geospatial and technology services group in Tampa, Florida. As a senior GIS professional, Karlin works with all aspects of lidar, remote sensing, photogrammetry, and GIS-related projects. Many thanks to Kirk Waters (NOAA/Applied Sciences Program) for helpful hints on this column.



Too young to drive the car? Perhaps! But not too young to be curious about geospatial sciences.

The ASPRS Foundation was established to advance the understanding and use of spatial data for the betterment of humankind. The Foundation provides grants, scholarships, loans and other forms of aid to individuals or organizations pursuing knowledge of imaging and geospatial information science and technology, and their applications across the scientific, governmental, and commercial sectors.

Support the Foundation, because when he is ready so will we.

asprsfoundation.org/donate



Hans J. Wehrli

Photogrammetric Pioneer

Hans J. Wehrli passed away on February 20, 2020. He is survived by his wife of 64 years, Lisette Wehrli, and his children Nicole Wampfler, Gregory Wehrli, and Linette LaMountian, as well as his seven grandchildren.

Hans, born in Aarau, Switzerland, on April 25, 1926 came to the United States in 1953 to expand Kern Instruments Inc., a subsidiary of Kern & Co. AG, Aarau, Switzerland. Initially the focus of his assignment was in surveying instrumentation, including adaptation of such instruments for the optical tooling industry, ranging in applications from alignment of paper machines to sophisticated guidance systems in the aerospace industry.

By the early 1960's, under Hans's leadership, Kern entered the photogrammetric market and quickly became an industry leader. Under his guidance in the concept, design and sales are instruments such as the PG2, AT Table, Monocomparator, Point marker, Stereo comparator, DSR analytical stereoplotter, and several one-off instruments.

Hans understood early the benefit of electronics to improve productivity.

For example, the DKM2-A, a universal one-second theodolite became the standard for a new generation of optical/mechanical theodolites with automatic vertical indexing. And when combined with an electronic distance meter, displayed the distance in digital format. In addition to surveying uses, the next generation of this new theodolite found wide acceptance for highly precise industrial measurements.

Hans was instrumental in 1969 in having Kern optical lenses accompany the moon landing of Apollo 11 where these lenses were used in the craft's acquisition cameras which filmed the tests of reactions of men and materials in space.



As a visionary, Hans very quickly recognized the power and validity of PC's. As the leader, he dedicated his time and efforts to a team that would convert the entire software suite to this new DOS platform.

Hans and his Kern team brought the first Industrial Measurement System when it released the ECDS (Electronic coordinate Determination System) integrating an E2 theodolite with a PC and software providing three essential components: data collection, data reduction and data analysis. This system was used for the alignment of the magnets of the SLC (Stanford Linear Collider).

In 1988, Hans received the ASPRS Fairchild Award established to recognize someone who demonstrated outstanding efforts and influence in

the development of the art of aerial photogrammetry in the United States.



Kern 25 Years USA Anniversary, May 24th, 1979

Even after retiring in 1988 when Kern was merged with Wild Leitz (Hexagon), Hans continued to influence the photogrammetric market. He designed and implemented the low-cost Alpha 2000 (analytical stereo plotter), RM-1 to RM-6 photoscanners and DAS digital aerial cameras under the company Wehrli & Associates.

2 0 2 0

William T. Pecora AWARD

**2020 William T. Pecora Award Nominations
Now Being Accepted through May 1, 2020**

The William T. Pecora Award is presented annually to individuals or groups that have made outstanding contributions toward understanding the Earth by means of remote sensing. The Department of the Interior (DOI) and the National Aeronautics and Space Administration (NASA) jointly sponsor the award.

The award was established in 1974 to honor the memory of Dr. William T. Pecora, former Director of the U.S. Geological Survey and Under Secretary, Department of the Interior. Dr. Pecora was a motivating force behind the establishment of a program for civil remote sensing of the Earth from space. His early vision and support helped establish what we know today as the Landsat satellite program.

The Award Committee must receive nominations for the 2020 award by May 1, 2020. Additional questions can be directed to the Committee at pecora@usgs.gov.

ELIGIBILITY

Any individual or group working in the field of remote sensing of the Earth is eligible to receive the William T. Pecora Award. We accept nominations for public and private sector individuals, teams, organizations, and professional societies. Both national and international nominations are welcome. Previous nominees not selected as recipients may be re-nominated for future awards.

An individual award recognizes achievements in the scientific and technical remote sensing community, as well as contributions leading to successful practical applications of remote sensing. Consideration will be given to sustained career achievements or singular contributions of major importance to the field of remote sensing.

A group award recognizes a team, a group of individuals, or part of an organization that has made major breakthroughs in remote sensing science or technology or developed an innovative application that has a significant impact on the user community or national/international policies.

Specific individual and group achievements should be peer-reviewed and documented in industry-recognized and scientifically credible publications.

This year's flyer also provides additional details and can be shared with other interested parties:

<https://prd-wret.s3-us-west-2.amazonaws.com/assets/palladium/production/atoms/files/PECORA-Award-flyer-2020.pdf>.

Detailed Instructions for preparing a nomination and other information about the award can be found on the Pecora Award web site: www.usgs.gov/pecora.



JOURNAL STAFF

Editor-In-Chief

Alper Yilmaz, Ph.D., PERSeditor@asprs.org

Associate Editors

Rongjun Qin, Ph.D., qin.324@osu.edu

Michael Yang, Ph.D., michael.yang@utwente.nl

Petra Helmholz, Ph.D., Petra.Helmholz@curtin.edu.au

Bo Wu, Ph.D., bo.wu@polyu.edu.hk

Clement Mallet, Ph.D., clemallet@gmail.com

Vasit Sagan, Ph.D., Vasit.Sagan@slu.edu

Jose M. Pena, Ph.D., jmpena@ica.csic.es

Prasad Thenkabail, Ph.D., pthenkabail@usgs.gov

Ruisheng Wang, Ph.D., ruiswang@ucalgary.ca

Desheng Liu, Ph.D., liu.738@osu.edu

Valérie Gouet-Brunet, Ph.D., valerie.gouet@ign.fr

Dorota Iwaszczuk, Ph.D., dorota.iwaszczuk@tum.de

Qunming Wang, Ph.D., wqm11111@126.com

Filiz Sunar, Ph.D., fsunar@itu.edu.tr

Norbert Pfeifer, Ph.D., np@ipf.tuwien.ac.at

Jan Dirk Wegner, Ph.D., jan.wegner@geod.baug.ethz.ch

Hongyan Zhang, Ph.D., zhanghongyan@whu.edu.cn

Zhenfeng Shao, Ph.D., shaozhenfeng@whu.edu.cn

Dongdong Wang, Ph.D., ddwang@umd.edu

Assistant Editor

Jie Shan, Ph.D., jshan@ecn.purdue.edu

Contributing Editors

Grids & Datums Column

Clifford J. Mugnier, C.P., C.M.S., cjmce@lsu.edu

Book Reviews

Sagar Deshpande, Ph.D., bookreview@asprs.org

Mapping Matters Column

Qassim Abdullah, Ph.D., Mapping_Matters@asprs.org

Sector Insight

Lucia Lovison-Golob, Ph.D., lucia.lovison@sat-drones.com

Bob Ryerson, Ph.D., FASPRS, bryerson@kimgeomatics.com

GIS Tips & Tricks

Alvan Karlin, Ph.D., CMS-L, GISP akarlin@Dewberry.com

ASPRS Staff

Assistant Director — Publications

Rae Kelley, rkelly@asprs.org

Electronic Publications Manager/Graphic Artist

Matthew Austin, maustin@asprs.org

Advertising Sales Representative

Bill Spilman, bill@innovativemediasolutions.com

NEW ASPRS MEMBERS

ASPRS would like to welcome the following new members!

Alaska

Brian Gutzwiller

At Large

Dr. Mehmet Alkan

Dr. Suliman Gargoum

Yifei Liu

Fabio Carneiro Lobo, Sr.

Reid McLean

Shu Yun Wei

Wanben Wu

Trudy Ganendra

Cascadia

Jesse Joe, GST

Barrett Lewis

Audrey McHugh Britton

Russell Park

Thomas Spaul

Megan Thayne

Florida

Aidan Allenbaugh

Amobichukwu C. Amanambu

Paul Barnes

Joseph Gareau

Robert Hanson

Heartland

Dustin Shropshire

Dr. Jason A. Tullis

Mid South

Renga Samy

David Richard Trotter

Robert Sorrells

Andrew Szush

Kenneth Comeaux, CP

Eric John Deroche

North Atlantic

Mingshi Yu

Dr. Anthony Campbell

Northeastern

Hao Quan

Pacific Southwest

Dr. Ahmed Elaksher, CP

Iryna Dronova

Oscar Duran

Adam Johnson

Clayton Yada

Potomac

Chinazor Stephanie Azubike

Michael V. Finn

Daniel Fogleman

Dr. Stanley Grossman

Jie Lin

Jessica S. Parsons, CP

Kurt R. Rogers

Rocky Mountain

Brian Connolly

Amanda Drinkard

Mr. Eric McNeill

Eli James Rodemaker

Western Great Lakes

Daniel Boudreau, GISP

Josh Wilber

FOR MORE INFORMATION ON ASPRS MEMBERSHIP, VISIT

[HTTP://WWW.ASPRS.ORG/JOIN-NOW](http://www.asprs.org/join-now)

Your Path To Success In The Geospatial Community

PE&RS Special Issue Call for Submissions

Optical Polarization Remote Sensing & Photogrammetry

Photogrammetric Engineering and Remote Sensing (PE&RS) is seeking submissions for special issue on optical polarization remote sensing.

Light is an electromagnetic wave vector and its wave equation of scalar propagation has four basic parameters: amplitude, frequency, phase and polarization. The polarization signal is usually ignored, and the remaining three parameters provide the physical basis of the four major resolutions (radiometric, spectral, spatial and temporal) of optical remote sensing. Nevertheless, polarization, which refers to the asymmetry of the light vibration, provides key information for studying the properties of materials.

More than 30 years of work has resulted in a science of polarization remote sensing (PoIRS). PoIRS includes the underlying physical theories, measurement instruments, including precision detection technology, and analytical approaches for studying polarization in imagery. The general conclusion of this research is that including the polarization signal in optical remote sensing images (such as hyperspectral or infrared images) can increase the contrast ratio by 2–3 orders of magnitude for mapping snow and ice, water quality, environmental pollution, rock density and roughness, oil spills, vegetation biomass, air pollution particle detection and atmospheric attenuation applications. Thus, PoIRS offers a unique detection capability.

This special issue seeks papers on all aspects of optical polarization remote sensing science and technology, including theory, technology and applications.

How to Submit your Manuscript

All submissions will be peer reviewed according to the *Photogrammetric Engineering and Remote Sensing (PE&RS)* guidelines. Submitted manuscripts should not have been published or be under review elsewhere.

Prospective authors should consult the *PE&RS* Instructions for Authors on the journal homepage for guidelines and information on paper formatting and submission.

Authors should submit manuscripts using the *PE&RS* manuscript central system at <https://www.editorialmanager.com/asprs-pers/default.aspx>. Please choose '*PE&RS* Special Issue Paper' from the 'Manuscript Type' picklist on the submission form, irrespective of the paper type (i.e. even if your paper would normally be classified as a Research Letter, Tech Note, Research Paper, or Review Article). Also, please enter "Polarization" in the space provided on the submission form for the name of the special issue.

Important Dates

Deadline for the submission of contributions: **May 31, 2020**

Expected print publication date: **Late 2020**

Articles will be available online after acceptance, final technical review and the completion of revisions for compliance with journal format. However, the paper copy of the special issue will be published only when all papers are accepted.

If you have any specific questions about the special issue, please contact the editorial team listed below.

Editorial Team

Editor:

- Lei Yan, Peking University, China, lyan@pku.edu.cn
- Jouni Peltoniemi, Finnish Geospatial Research Institute (FGI) Finland, jouni.peltoniemi@nls.fi

Associate Editor:

- Bin Yang, Hunan University, China, binyang@hnu.edu.cn

Satellite-Imagery Geometric Accuracy Improvement Based on Direct Correction of Dominant Coefficients

Xinming Tang, Changru Liu, Ping Zhou, Ning Cao, Fengxiang Li, and Xia Wang

Abstract

An important and difficult point in the application of satellite imagery is refining the positioning model and improving the geometric accuracy. In this study, we focus on improvement in geometric accuracy and develop a new rational function model (RFM) refinement method. First, we derive the conversion relationship between the rigorous sensor model and the RFM, based on which we illustrate the approximate meaning of the zero-order and first-order terms of the rational polynomial coefficients (RPCs). Second, the correlation problem between RPCs and the influence of individual RPCs on geometric positioning accuracy are analyzed and verified. The dominant coefficients that determine geolocation are then identified. Finally, a new RFM refinement method based on direct correction of the dominant coefficients is proposed and validated. The experiments, conducted with ZY3-02 satellite imagery, indicate that the proposed method can effectively improve the geometric accuracy of satellite images.

Introduction

In recent decades, with the continuous development of satellite technology, numerous high-resolution optical satellites have been put into use, providing an effective means for rapid and large-scale collection of geospatial information. In particular, with the successful launch of satellites such as the United States' *Ikonos* (Fraser, Hanley and Yamakawa 2002; Ager 2003; Lutes 2004), *QuickBird* (Noguchi *et al.* 2004), and *WorldView* series (Aguilar, Saldaña and Aguilar 2013), France's *SPOT* system (Madani 1999), Japan's *ALOS* (Osawa 2004), and China's *Ziyuan-3* (X. Tang *et al.* 2013; Xu *et al.* 2017) and *Gaofen* series (Zheng and Zhang 2016), remote sensing satellite images have been increasingly used in digital model generation (Toutin 2004; Poon *et al.* 2005), topographic mapping (Di, Ma and Li 2003; Holland, Boyd and Marshall 2006), environmental protection (Stumpf, Malet and Delacourt 2017), and more, producing significant economic and social benefits. However, the imaging model of the satellite image is the key technology in processing and application of remote sensing images. How to refine the imaging model to improve geometric accuracy is an important and difficult research point.

Nowadays, the rational function model (RFM) is the mainstream postprocessing model of most satellites, owing to its advantages of sensor independence, computational convenience, and universality, and it is the first choice to replace the rigorous sensor model (RSM; Tao and Hu 2001; Grodecki and Dial 2003; Fraser, Dial and Grodecki 2006). Usually, the

RFM provided by satellite-imagery vendors is calculated from an RSM with direct least-squares solutions. However, due to the effects of incomplete calibration and measurement errors of satellite orbit and attitude, inherent errors are always introduced into the RFM, which affect the geometric positioning accuracy. To eliminate these errors, various compensation methods have been proposed.

Regenerating the rational polynomial coefficients (RPCs) with control data is the simplest solution (Tao and Hu 2001; Hu and Tao 2002; Long, Jiao and He 2014). This scheme is simple in theory and effective when the RSM is excessively complicated to develop or is not available. However, this method is obviously terrain dependent, and it is highly dependent on the actual terrain relief and the number and distribution of ground control points (GCPs), which are difficult constraints in practical applications. When the accuracy requirement is not stringent, this method can be used for photogrammetry rectification and remote sensing applications.

Correction parameters attached to the RFM are the most commonly used bias-compensation method at present. These bias-compensation models are defined in image space or object space and usually modeled as shift, shift and drift, affine transformation, and second-order polynomial models (Fraser and Hanley 2005). Aguilar *et al.* (2013) and Fraser and Hanley (2003) have demonstrated that the shift model is effective for *Ikonos*, *WorldView*, and *GeoEye* satellites. As for *QuickBird* images, Noguchi *et al.* (2004) have stated that the shift-and-drift model is warranted if the highest possible accuracy is sought. Tong, Liu, and Weng (2010) and J. Wang, Di, and Li (2005) compared shift, shift-and-drift, affine transformation, and second-order polynomial models using *QuickBird* and *Ikonos* imagery and obtained meter-level accuracy with a number of good-quality GCPs. Experiments by Pan *et al.* (2013), T. Wang *et al.* (2014), and Liu *et al.* (2013) confirmed that the affine transformation model is effective for the *Ziyuan-3* (ZY3) and *TH1* satellites. Similar research has been reported for other types of satellite images with this bias-compensation method (Jiang *et al.* 2015; Jeong *et al.* 2016; Topan *et al.* 2016; M. Wang *et al.* 2017).

Although these bias-compensation methods can improve geometric positioning accuracy, they are implemented with additional parameters and the original RPCs remain unchanged; thus, the geometric positioning often depends on these correction parameters. In addition, for compatibility with different photogrammetric systems it is often necessary to generate new RPCs using these correction parameters (Fraser *et al.* 2006; Tong *et al.* 2010; Rupnik *et al.*, 2016). Although

Xinming Tang, Changru Liu, Ping Zhou, Ning Cao, and Xia Wang are with the Land Satellite Remote Sensing Application Center, Ministry of Natural Resource of the People's Republic of China, Beijing 100048, China (liucr13@163.com).

Fengxiang Li is with the Shandong Provincial Institute of Land Surveying and Mapping, Jinan 250102, China.

Photogrammetric Engineering & Remote Sensing
Vol. 86, No. 4, April 2020, pp. 215–224.
0099-1112/20/215–224

© 2020 American Society for Photogrammetry
and Remote Sensing
doi: 10.14358/PERS.86.4.215

these new RPCs exhibit better substitution accuracy, generating them involves significant work.

Wu *et al.* (2015) presented an RFM direct-refinement approach to the geometric integration of high-resolution satellite imagery and airborne lidar data and showed a method that improved the dominating RPCs and the ground coordinates of the lidar points, decreased the inconsistencies between the two data sets, and improved geopositioning accuracy. S. Tang, Wu, and Zhu (2016) also used this method in a combined adjustment of multiresolution satellite imagery to improve geopositioning accuracy. Their method is implemented with only part of the RPCs modified and is a novel RFM refinement method. However, there is no theoretical analysis, and numerous RPCs need to be corrected even though some of them are unnecessary.

In this study, a new and improved RPC direct-correction method is developed and verified based on theory and experiments. The advantage of this method is that it corrects only a few RPCs, and the result of the refinement still consists of RPCs. This allows different commercial software packages to be seamlessly linked together. In addition, this method is theoretically applicable to all remote sensing images using the RFM as the geometric model. The method is validated with ZY3-02 satellite images in single-scene and block-network modes. Experimental results verify the feasibility and effectiveness of the proposed method.

Principles and Methods

RSM and RFM

The RSM describes the correspondence between the projection center, the image point, and the ground point. It is a sensor geometry model based on a collinear equation (Habib *et al.* 2007; Jiang *et al.* 2018):

$$\begin{bmatrix} X \\ Y \\ Z \end{bmatrix}_{\text{WGS84}} = \begin{bmatrix} X(t) \\ Y(t) \\ Z(t) \end{bmatrix}_{\text{WGS84}} + mR_{\text{J2000}}^{\text{WGS84}}(t)R_{\text{body}}^{\text{J2000}}(t)R_{\text{cam}}^{\text{body}} \begin{bmatrix} x \\ y \\ -f \end{bmatrix}, \quad (1)$$

where t represents the imaging time, $(X, Y, Z)_{\text{WGS84}}$ represents the object coordinate of the image point in the World Geodetic System 1984 (WGS84) coordinate system, $(X(t), Y(t), Z(t))_{\text{WGS84}}$ represents the center coordinate of the GPS antenna in the WGS84 system, and m is the scale factor. The expressions $R_{\text{J2000}}^{\text{WGS84}}(t)$, $R_{\text{body}}^{\text{J2000}}(t)$, and $R_{\text{cam}}^{\text{body}}$ are, respectively, the rotation matrices from the J2000 coordinate system to the WGS84 system, from the satellite's body coordinate system to the J2000 coordinate system, and from the camera coordinate system to the satellite's body coordinate system; and $(x, y, -f)$ are the image-point coordinates in the camera coordinate system, with f the focal length.

The RFM uses the ratio of two polynomials to represent the correspondence between the image-point coordinates (x, y) and the ground coordinates (X, Y, Z) . Equation 2 is an example of an RFM based on third-order polynomials (Toutin 2004; Poon *et al.* 2005):

$$\begin{cases} x = \frac{\sum_{i=0}^{m_1} \sum_{j=0}^{m_2} \sum_{k=0}^{m_3} a_{ijk} X^i Y^j Z^k}{\sum_{i=0}^{n_1} \sum_{j=0}^{n_2} \sum_{k=0}^{n_3} b_{ijk} X^i Y^j Z^k} \\ y = \frac{\sum_{i=0}^{m_1} \sum_{j=0}^{m_2} \sum_{k=0}^{m_3} c_{ijk} X^i Y^j Z^k}{\sum_{i=0}^{n_1} \sum_{j=0}^{n_2} \sum_{k=0}^{n_3} d_{ijk} X^i Y^j Z^k} \end{cases}, \quad (2)$$

where (x, y) are the normalized image coordinates, (X, Y, Z) are the normalized object coordinates, and $a_{ijk}, b_{ijk}, c_{ijk}, d_{ijk}$ are RPCs. The maximum power of each ground coordinate $(m_1, m_2, m_3, n_1, n_2, n_3)$ is limited to 3, and the total power of all ground coordinates is also limited to 3; hence, this RFM usually consists of 78 RPCs: $a_i, b_i, c_i,$ and d_i ($i = 0-19$), where b_0 and d_0 are equal to 1.

The RSM is essentially a collinear equation, and Equation 1 can be converted to the following format at time t_0 :

$$\begin{cases} x = -f \frac{R_{11}(X - X_s) + R_{12}(Y - Y_s) + R_{13}(Z - Z_s)}{R_{31}(X - X_s) + R_{32}(Y - Y_s) + R_{33}(Z - Z_s)} \\ y = -f \frac{R_{21}(X - X_s) + R_{22}(Y - Y_s) + R_{23}(Z - Z_s)}{R_{31}(X - X_s) + R_{32}(Y - Y_s) + R_{33}(Z - Z_s)} \end{cases}, \quad (3)$$

where

$$R^{-1} = \left(R_{\text{J2000}}^{\text{WGS84}}(t_0) R_{\text{body}}^{\text{J2000}}(t_0) R_{\text{cam}}^{\text{body}} \right)^{-1} = \begin{pmatrix} R_{11} & R_{12} & R_{13} \\ R_{21} & R_{22} & R_{23} \\ R_{31} & R_{32} & R_{33} \end{pmatrix}.$$

Equation 3 can be expanded as follows:

$$\begin{cases} x = \frac{-fR_{11}X - fR_{12}Y - fR_{13}Z + f(R_{11}X_s + R_{12}Y_s + R_{13}Z_s)}{R_{31}X + R_{32}Y + R_{33}Z - (R_{31}X_s + R_{32}Y_s + R_{33}Z_s)} \\ y = \frac{-fR_{21}X - fR_{22}Y - fR_{23}Z + f(R_{21}X_s + R_{22}Y_s + R_{23}Z_s)}{R_{31}X + R_{32}Y + R_{33}Z - (R_{31}X_s + R_{32}Y_s + R_{33}Z_s)} \end{cases}. \quad (4)$$

The constant term in the denominator of Equation 4 is rationalized and simplified as follows:

$$\begin{cases} x = \frac{A_1X + B_1Y + C_1Z + D_1}{A_3X + B_3Y + C_3Z + 1} \\ y = \frac{A_2X + B_2Y + C_2Z + D_2}{A_3X + B_3Y + C_3Z + 1} \end{cases}. \quad (5)$$

Equation 5 is the commonly used direct linear transformation model of the frame sensor, that is, the simple form of the RSM. For the linear-array push-broom sensor, the denominator term of the second rational polynomial (y value, flight direction) in Equation 5 should be 1.

When the RFM takes the one-order terms, Equation 2 can be simplified as follows:

$$\begin{cases} x = \frac{a_0 + a_1X + a_2Y + a_3Z}{1 + b_1X + b_2Y + b_3Z} \\ y = \frac{c_0 + c_1X + c_2Y + c_3Z}{1 + d_1X + d_2Y + d_3Z} \end{cases}. \quad (6)$$

By comparing Equation 2 with Equations 5 and 6, we find that the RFM is essentially a generic expression, and the latter two equations can be deduced from Equation 2 using different RPCs. That is to say, the RFM is an approximation of the RSM.

As we know, the RSM is physically meaningful and theoretically rigorous; therefore, we can confirm that the zero-order and first-order terms in the RFM can express the optical projection in the imaging process, which demonstrates the approximate physical meaning of these coefficients. However, it should be noted that all the coefficients in Equation 5 are rationalized by the constant term of the denominator in Equation 4. That is, each coefficient in Equation 5 is a function expression for those in Equation 4. Considering that Equation 5 is the first-order approximation of the RFM, the RPCs can be regarded as all different function combinations

of RSM parameters, from which the correlation between the RPCs is preliminarily proved in the theory. Theoretically, we can obtain the conversion relationship between the RFM and RSM through Equations 4 and 5, but as the RFM generally takes the third-order polynomial form and its denominator terms generally take different values, it is difficult to accurately calculate the RFM from the RSM, and vice versa—and thus, it is impossible to accurately express the physical meaning of the RPCs. That is to say, the RPCs do not have a specific physical meaning, but are merely a mathematical expression.

Correlation Analysis of RPCs

Regarding the particular imaging characteristics of the high orbit, the narrow field of view, and the foregoing preliminary discussion of the correlation problem within the RPCs, we can theoretically derive the correlation between RPCs from a mathematical point of view.

According to the corresponding points and the RFM, the image-point residuals can be calculated as follows:

$$\begin{cases} f(R) = x - x' \\ g(R) = y - y' \end{cases}, \quad (7)$$

where (f, g) are the image-point residual errors, R are the RPCs, (x, y) are the image-point coordinates, and (x', y') are the image coordinates calculated by the RFM. Then for any point k , we can obtain the coefficient matrix:

$$A_k = \begin{bmatrix} \frac{\partial f_k}{\partial R} \\ \frac{\partial g_k}{\partial R} \end{bmatrix} = \begin{bmatrix} 1 & X_k & \cdots & Z_k^3 & -x_k X_k & \cdots & -x_k Z_k^3 \\ 1 & X_k & \cdots & Z_k^3 & -y_k X_k & \cdots & -y_k Z_k^3 \end{bmatrix}. \quad (8)$$

Then the cofactor matrix can be determined by

$$Q_{RR} = A^T P A = \sum_{k=1}^n A_k^T P_k A_k, \quad (9)$$

where n is the number of corresponding points and P_k is set as the identity matrix.

According to the error theory, the correlation coefficient c_{ij} can be calculated by

$$c_{ij} = \frac{q_{ij}}{\sqrt{q_{ii}} \sqrt{q_{jj}}}, \quad (10)$$

where q is the cofactor of the RPCs in the cofactor matrix and i and j are the indices for the RPCs ($= 0-19$).

From the perspective of mathematics, the two formulas in Equation 7 respectively represent the sample and line directions of the image and have no relationship; thus, we discuss only the correlation between a and b , and c and d are similar.

The correlation coefficient between a_0 and a_1 is calculated as

$$c_{(a_0, a_1)} = \frac{\sum X}{\sqrt{\sum 1 \sum X^2}} = \frac{\sum X}{\sqrt{n \sum X^2}}. \quad (11)$$

When the corresponding points are sufficient in quantity and are widely distributed within the whole image, we can obtain the relationship $\sum X = 0$; then the correlation coefficient is close to 0, which could also be derived from the polynomial expressions. Similarly, we can conclude that the correlation coefficients within a_0, a_1, a_2, a_3 and within b_1, b_2, b_3 are all close to 0.

Similarly, the correlation coefficient between a_1 and a_{11} is expressed as

$$c_{(a_1, a_{11})} = \frac{\sum (X^2)^2}{\sqrt{\sum X^2 \sum (X^3)^2}} = \frac{\sum X^4}{\sqrt{\sum X^2 \sum X^6}}. \quad (12)$$

According to the transform principle of limitation sum to definite integral, Equation 12 can be transformed into

$$c_{(a_1, a_{11})} = \frac{\int_{-1}^1 x^4 dx}{\sqrt{\int_{-1}^1 x^2 dx \cdot \int_{-1}^1 x^6 dx}} = 0.92. \quad (13)$$

It can be noted that there are strong correlations between a_1 and a_{11} .

Similarly, we calculated the correlation coefficients between the other coefficients, and found that groups such as $a_0 - b_2, a_1 - b_4, a_2 - b_8, a_2 - b_9, a_3 - b_6$, and $a_4 - b_1$ have strong correlations. As a result, these correlation problems inevitably caused the normal equations to be ill conditioned and indeterminate in the least-squares solutions; thus, the correlation problem should be considered.

Influence of Individual RPCs on Geometric Positioning

Because there are many RPCs and they have no specific physical meaning, it is impossible to theoretically deduce the influence of individual RPCs on the whole imaging geometry. In this investigation, we designed an experiment from the perspective of numerical error, to verify the impact of RPCs on geometric positioning accuracy under different accuracy conditions as follows:

1. The test image was divided into a regular grid (e.g., 20×20), and the image coordinate of each grid point was set as the image point of the virtual control point; then the image point was used to calculate the object coordinate with the RFM in different elevation layers. To ensure computational stability, the number of elevation layers should be greater than 3.
2. According to the principle of single variable, each RPC was subjected to different magnitude errors (e.g., $0.01r, 0.02r, \dots, 0.1r$, where r represents the coefficient value), whereas the other coefficients remained unchanged. With this new RFM and the virtual control points, a new image coordinate was obtained and the image-point coordinate variance calculated.
3. Counting the variances of those coordinates, the influence of the independent RPCs on geopositioning accuracy was analyzed.

The experiment conducted with a nadir (NAD) image of the ZY3-02 satellite indicated that the geometric geolocation error was proportional to the coefficients' numerical precision for every RPC. Hence, Figure 1 shows only the effect trend of different RPCs on the geometric location accuracy under the condition of $0.05r$.

Obviously, the degree of influence that different RPCs have on the geometric accuracy is very different. First, in terms of the same class of polynomial coefficients, the geometric errors of the 0th, 1st, 2nd, 3th, 4th, 7th, and 8th items in each polynomial—especially the first four (i.e., the zero-order and first-order terms of the RPCs)—are significantly greater than those of the other items. Compared with those first four items, the degree of influence of the other items is extremely small and in fact almost negligible. In addition, comparing the different classes of polynomial coefficients, the influence of the coefficients in the numerator is extraordinary larger than that of the coefficients in the denominator, and the latter can be considered negligible. A similar principle was reflected with the forward (FWD) and backward (BWD) sensors, which were arranged at an inclination of $\pm 22^\circ$ from the NAD.

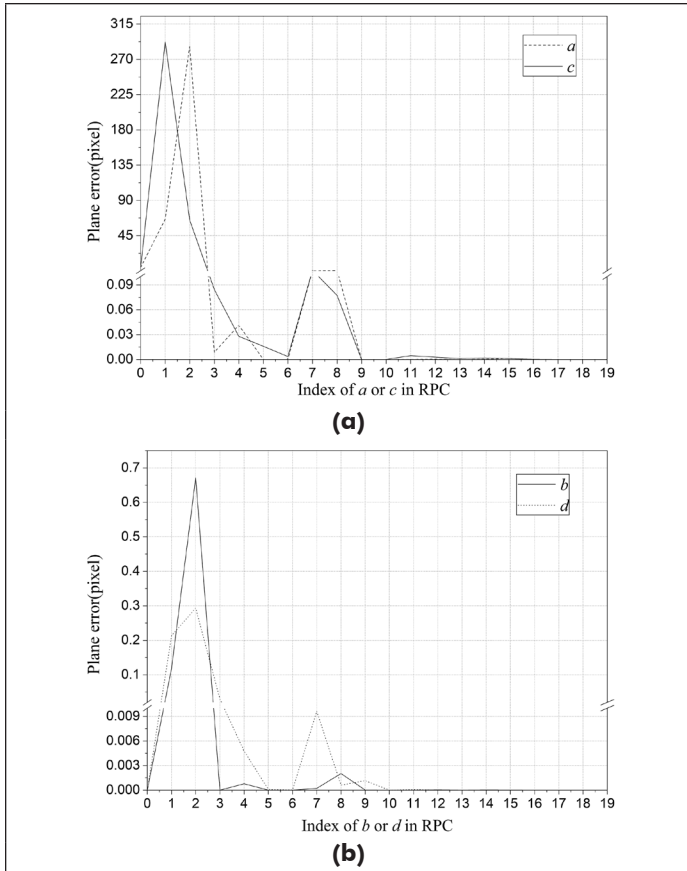


Figure 1. Plane errors affected by rational polynomial coefficients (RPCs) with numerical accuracy of $0.05r$ for ZY3-02 nadir image: (a) RPCs of a and c ; (b) RPCs of b and d .

This analysis indicates that although the RPCs are numerous, only some of them have a substantial influence on the geometric positioning, particularly the first four terms of the numerator polynomials. We refer to these eight coefficients that have a significant impact on geometric positioning accuracy as the *dominant coefficients*. Therefore, to improve the image geometric positioning accuracy, we must improve the accuracy of these dominant coefficients.

Geometric Refinement Based on Direct Correction of Dominant Coefficients

The foregoing experiments and analyses reveal the approximate relation between the RFM and the RSM. The geometric positioning accuracy of the RFM is actually determined by the zero order and first order of each polynomial; therefore, it is necessary to improve the numerical precision for the RPCs corresponding to those in the RSM, that is, the zero-order and first-order terms in the RFM, for the purpose of improving the stability of the imaging geometry. Furthermore, considering the different influence of these coefficients on geometric positioning accuracy and their weak correlation, the image geometric positioning accuracy can be significantly improved by increasing the precision of the first four terms (dominant coefficients) of the numerator polynomials.

Based on this analysis, the R in Equation 7 becomes the first four terms (dominant coefficients) of the numerator polynomials in the RFM; then the error equation for the RFM becomes

$$\begin{cases} v_x = \frac{\partial f}{\partial a_0} \Delta a_0 + \frac{\partial f}{\partial a_1} \Delta a_1 + \frac{\partial f}{\partial a_2} \Delta a_2 + \frac{\partial f}{\partial a_3} \Delta a_3 - (x - x') \\ v_y = \frac{\partial g}{\partial c_0} \Delta c_0 + \frac{\partial g}{\partial c_1} \Delta c_1 + \frac{\partial g}{\partial c_2} \Delta c_2 + \frac{\partial g}{\partial c_3} \Delta c_3 - (y - y') \end{cases} \quad (14)$$

For the block-network images, the unknowns also include the object coordinate of the tie point. The error equation can be expressed as

$$\begin{cases} v_x = \frac{\partial f}{\partial a_0} \Delta a_0 + \frac{\partial f}{\partial a_1} \Delta a_1 + \frac{\partial f}{\partial a_2} \Delta a_2 + \frac{\partial f}{\partial a_3} \Delta a_3 + \frac{\partial f}{\partial X} \Delta X + \frac{\partial f}{\partial Y} \Delta Y + \frac{\partial f}{\partial Z} \Delta Z - (x - x') \\ v_y = \frac{\partial g}{\partial c_0} \Delta c_0 + \frac{\partial g}{\partial c_1} \Delta c_1 + \frac{\partial g}{\partial c_2} \Delta c_2 + \frac{\partial g}{\partial c_3} \Delta c_3 + \frac{\partial g}{\partial X} \Delta X + \frac{\partial g}{\partial Y} \Delta Y + \frac{\partial g}{\partial Z} \Delta Z - (y - y') \end{cases} \quad (15)$$

where (v_x, v_y) are the image-point residuals; (x, y) are the image measurement coordinates, which can be obtained through manual picking or image matching; (x', y') are the calculated image-point coordinates with the RFM and object coordinates; $\Delta a_0, \Delta a_1, \Delta a_2, \Delta a_3, \Delta c_0, \Delta c_1, \Delta c_2,$ and Δc_3 are the corrections of the RPCs; and $(\Delta X, \Delta Y, \Delta Z)$ are the corrections of the object coordinates.

Moreover, as the RFM is an approximation of the RSM, the dominant coefficients can also be treated as a weighted pseudo-observation, which could provide certain constrains on the RPCs to avoid unpredictable corrections.

Combining this analysis, the direct correct method (DCM) of the RFM refinement can be expressed as

$$\begin{cases} V_1 = A_1 x - I_1 & P_1 \\ V_2 = A_2 x + B_2 y - I_2 & P_2 \\ V_3 = x - I_3 & P_3 \end{cases} \quad (16)$$

where $V_1, V_2,$ and V_3 are the measurement residual vectors; $x = \{\Delta a_0, \Delta a_1, \Delta a_2, \Delta a_3, \Delta c_0, \Delta c_1, \Delta c_2, \Delta c_3\}$ are the corrections of the dominant coefficients; $y = \{\Delta X, \Delta Y, \Delta Z\}$ are the corrections of the object coordinates; $A_1, A_2,$ and B_2 are the partial derivative coefficient matrix of the unknown parameters; $I_1, I_2,$ and I_3 are the measurement values; and $P_1, P_2,$ and P_3 are the weight matrix.

Compared with the method of Wu *et al.* (2015), the method proposed in this study reduces the number of parameters to be solved (from 18 to eight), and only the coefficients in the numerator polynomials that have the greatest influence on the geometric accuracy of the image are corrected, which can rapidly reduce the calculation complexity while still ensuring geometric accuracy. Moreover, our improved method is conducive to programming implementation.

In the actual calculation, the initial value of the dominant coefficients can be obtained from the original RPC file, and the object coordinate can be calculated by the first order of the RFM with the average elevation or by directly using the average coordinates of each RFM.

The observations are used to estimate the correction parameters with priori information. The weight of observation is defined as

$$P = \frac{\sigma_0^2}{\sigma^2} \quad (17)$$

where σ_0 is the error of unit weight and σ is the *a priori* error of the observation.

The first two observation equations in Equation 16 refer to the control-point and tie-point observations, and their weights are related to the coordinate accuracy of the image points. For the tie point, the matching accuracy determines its weight. Owing to the high-precision matching algorithm,

the error of the tie points is assumed to be 0.3 pixels. For the control point, the weight should be very large because of the high measurement accuracy, but it can change moderately in the iteration process according to the image-point adjustment residual. For P_1 and P_2 , the weight value represents the contributions of the image-point observations to the geometric accuracy, and the larger the weight is, the greater the contribution. The third equation is related to the model parameters, with weight determined by the original positioning accuracy of the image. In our investigation, the setup of P_3 follows that of Wu *et al.* (2015). In addition, considering the sensitivity of the dominant coefficients to the geolocation accuracy, the absolute corrections of the dominant coefficients can be set as the iteration convergence conditions to guarantee the iterative efficiency and accuracy with parameters that vary within a reasonable range.

Experiments and Discussion

Satellite images captured by the ZY3-02 satellite were used to verify the validity and feasibility of the proposed method. The ZY3-02 satellite, one of the Chinese civilian stereo-mapping satellites, was launched in May 2016 equipped with triple-linear cameras and a multispectral camera. Three experiments were conducted to test the proposed method in single-scene and block-network modes with different terrains. In addition, the correlation problem was validated by using all the images. Two types of GCP were used in the experiments: one is automatically matched with high-precision reference data, and the other is obtained by GPS with accuracy better than 1 m. The image-point coordinates of the GCPs were obtained by manual measurement with accuracy better than 0.5 pixel. The statistics used in the experiments were the root-mean-square error, maximum error, and mean error.

Study Areas and Data Sets

The first data set, which was captured by the ZY3-02 triple-linear stereo cameras and distributed in Taiyuan, Shanxi, China, was used to verify the effectiveness of the proposed approach in the single-scene mode. A total of 55 uniformly distributed GCPs were obtained from the corresponding digital orthophoto map and digital elevation model using a high-precision matching algorithm. All GCPs were imaged simultaneously in these three images, namely, the triple-linear stereo camera GCPs. The details and distribution of the image and control data are shown in Figure 2 and listed in Tables 1 and 2, respectively.

The second data set comprises the Hubei and Xinjiang test areas. The Hubei area consists of 42 images from the ZY3-02 satellite, with an area of approximately 20,000 km². This area is located in the eastern part of Hubei Province, China, with flat and hilly terrain. The Xinjiang test area is located in the central part of the Xinjiang Uygur Autonomous Region, China. This area consists of 63 scenes from the ZY3-02 satellite, covering an area of approximately 30,000 km² with mountains and hills as the dominant terrain. There is a sufficient number

Table 1. Information for images used in Taiyuan.

Item	Value
Sensor type	TLC
Center position	112.54° E, 38.21° N
Acquisition time	2017-01-04
Terrain	Flat, Hill
Stereo GCP number	55
Verify item	Plane, stereo

TLC = triple-linear camera; GCP = ground control point.

Table 2. Information for control data used in Taiyuan.

Area	GSD of DOM (m)	Horizontal accuracy of DOM RMS (m)	Elevation accuracy of DEM RMS (m)	Height range (m)	Size (km)	Center position
Shanxi	0.5	1	1.5	(487.11, 2398.7)	50 × 95	38.00° N, 112.52° E

GSD = ground sampling distance; DOM = digital orthophoto map; RMS = root-mean-square error; DEM = digital elevation model.

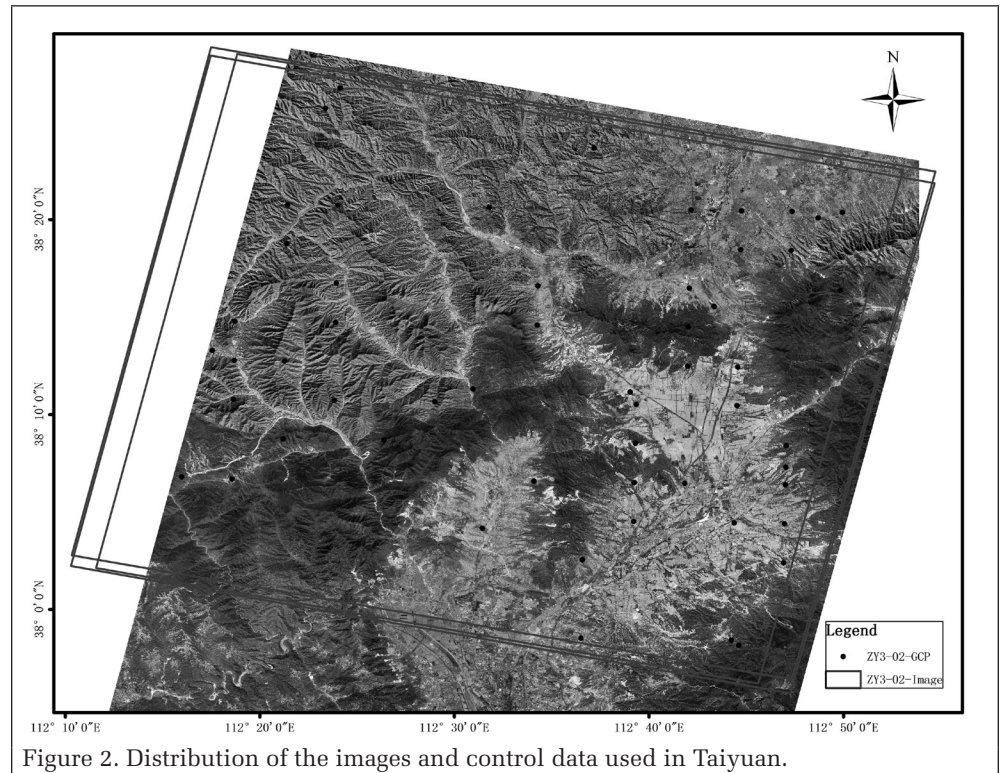


Figure 2. Distribution of the images and control data used in Taiyuan.

Table 3. Information for images from the second data set.

Area	Number of GCPs	Number of images	Image type	Size of area (km ²)	Terrain
Hubei	38	42	TLC	20,000	Flat, Hill
Xinjiang	18	63	TLC	30,000	Mountain, Hill

GCP = ground control point; TLC = triple-linear camera.

of GCPs in the two areas, and they are evenly distributed. The tie points were obtained by a high-precision matching algorithm. The detailed information of the second data set is listed in Table 3.

Verification of RPCs Correlations

The correlation coefficients between RPCs were calculated with all the test images. The virtual control points used in this study were obtained as described under *Influence of Individual RPCs on Geometric Positioning*. Then we calculated the cofactor matrix as shown in Equation 9 to estimate the correlation coefficient for each image. Because of

the differences in imaging perspective between the sensors, we used the mean value of the correlation coefficients as the statistic. According to the analysis under Correlation Analysis of RPCs, only the correlation coefficients between a and b are discussed, given that c and d are similar. RPCs that have a high correlation—a correlation coefficient greater than 0.7—are listed in bold in Table 4. If the correlation coefficient is smaller than 0.2, we consider those two RPCs to be unrelated and set the coefficient to 0.

As can be observed in Table 4, there is indeed a significant correlation between RPCs, even a strong one, which is consistent with the theoretical derivation under Correlation Analysis of RPCs. In terms of the polynomial order number, the zero-order and first-order terms of the RFM—that is, the first four terms of each polynomial—have small correlation

coefficients, even no correlation, but are closely related to other-order coefficients. There is little correlation between most of the second-order and third-order coefficients, but there is a strong correlation in the small remaining part, where the correlation coefficient is relatively large, close to 0.9 or even 1. In terms of the class of coefficients, the correlation within a is little, whereas the correlations within b and of a with b are significantly increased, and the situation is more complicated.

Single-Scene Refinement

Both the planimetric and stereoscopic accuracies were verified because of the stereoscopic observations of ZY3-02 satellite. Different numbers of GCPs were used to refine the RFM, and the remaining points were selected as check points to inspect the accuracy. Note that the GCPs were located in the four corners of the stereo pair when four points were used

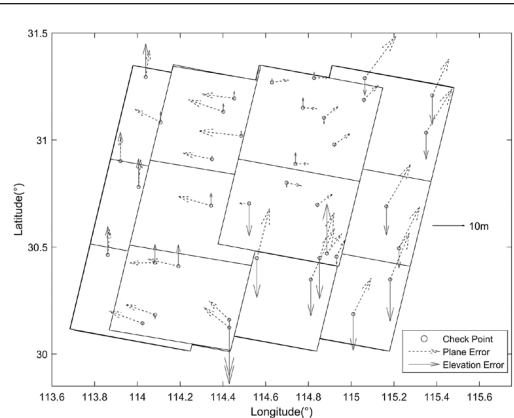
Table 4. Matrix of correlation coefficients between rational polynomial coefficients.

	a_0	a_1	a_2	a_3	a_4	a_5	a_6	a_7	a_8	a_9	a_{10}	a_{12}	a_{14}	a_{15}	a_{16}	a_{18}	b_1	b_2	b_3	b_{15}	b_{18}		
a_0	1.0																						
a_1	0.0	1.0																					
a_2	0.0	0.0	1.0																				
a_3	0.0	0.0	0.0	1.0																			
$a_7/a_8/a_9$	0.7	0.0	0.0	0.0	0.0	0.0	0.0																
$a_{11}/a_{12}/a_{13}$	0.0	0.9	0.0	0.0	0.0	0.0	0.0	0.0	0.0	0.0	0.0												
$a_{14}/a_{15}/a_{16}$	0.0	0.0	0.8	0.0	0.0	0.0	0.0	0.0	0.0	0.0	0.0	0.0	1.0										
$a_{17}/a_{18}/a_{19}$	0.0	0.0	0.0	0.7	0.0	0.0	0.0	0.0	0.0	0.0	0.0	0.0	0.0	0.0	0.0								
b_1	0.0	0.0	0.0	0.0	1.0	0.0	0.0	0.5	0.0	0.0	0.0	0.0	0.0	0.0	0.0	0.0	1.0						
b_2	0.7	0.0	0.0	0.0	0.0	0.0	0.0	0.5	1.0	0.6	0.0	0.0	0.0	0.0	0.0	0.0	0.0	1.0					
b_3	0.0	0.0	0.0	0.0	0.0	0.0	1.0	0.0	0.0	0.0	0.0	0.0	0.0	0.0	0.0	0.0	0.0	0.0	1.0				
b_4	0.0	0.7	0.0	0.0	0.0	0.0	0.0	0.0	0.0	0.0	0.0	1.0	0.0	-0.3	0.0	0.0	0.0	0.0	0.0	0.0			
b_5	0.0	0.0	0.0	0.0	0.0	0.0	0.0	0.0	0.0	0.0	1.0	0.0	0.0	0.0	0.0	0.0	0.0	0.0	0.0	0.0			
b_6	0.0	0.0	0.0	0.7	0.0	0.0	0.0	0.0	0.0	0.0	0.0	0.0	0.0	0.0	0.0	0.0	1.0	0.0	0.0	0.0			
b_7	0.0	0.4	0.6	0.0	0.0	0.0	0.0	0.0	0.0	0.0	0.0	0.0	1.0	0.5	0.5	0.0	0.0	0.0	0.0	0.0			
b_8	0.0	0.0	0.9	0.0	0.0	0.0	0.0	0.0	0.0	0.0	0.0	-0.3	0.6	1.0	0.7	0.0	0.0	0.0	0.0	0.0			
b_9	0.0	0.0	0.7	0.0	0.0	0.0	0.0	0.0	0.0	0.0	0.0	0.6	0.6	1.0	0.0	0.0	0.0	0.0	0.0	0.0			
b_{10}	0.0	0.0	0.0	0.0	0.7	0.0	0.0	0.0	0.0	0.0	0.0	0.0	0.0	0.0	0.0	0.0	0.0	0.0	0.0	0.0			
$b_{11}/b_{12}/b_{13}$	0.3	0.0	0.0	0.0	0.8	0.0	0.0	0.6	0.0	0.0	0.0	0.0	0.0	0.0	0.0	0.0	0.0	0.9	0.0	0.0			
b_{14}	0.5	0.0	0.0	0.0	0.0	0.0	0.0	0.7	0.7	0.4	0.0	0.0	0.0	0.0	0.0	0.0	0.4	0.7	0.0	0.0			
b_{15}/b_{16}	0.6	0.0	0.0	0.0	-0.0	0.0	0.0	0.3	1.0/0.8	0.4/0.7	0.0	0.0	0.0	0.0	0.0	0.0	-0.0	0.9/0.8	0.0	1.0/0.7			
$b_{17}/b_{18}/b_{19}$	0.0	0.0	0.0	0.0	0.0	0.0	0.6/0.9/0.9	0.0	0.0	0.0	0.0	0.0	0.0	0.0	0.0	0.0	0.0	0.0	0.7/0.9/0.9	0.0	0.0	0.0/1.0/0.8	

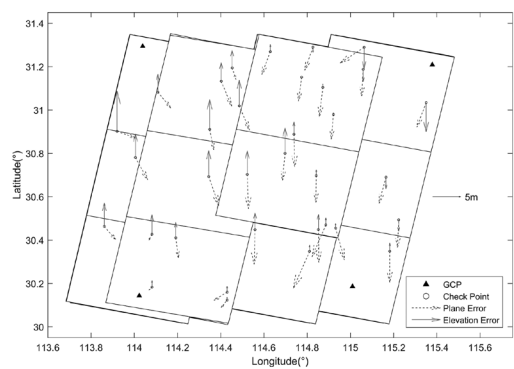
Table 5. Results of refinement of ZY3-02 images with different models.

Model	Number of GCPs/CPs	Plane accuracy (pixels)						Stereo accuracy (m)		
		NAD		BWD		FWD		East	Plane North	Height
		x	y	x	y	x	y			
Direct reproject	0/55	4.93	9.14	1.16	12.95	3.60	6.87	15.4	11.19	17.57
Affine transformation	4/51	0.75	0.35	0.77	0.68	0.81	0.77	0.79	1.89	3.45
	5/50	0.70	0.35	0.76	0.67	0.68	0.79	0.85	1.72	3.39
	6/49	0.70	0.36	0.74	0.60	0.71	0.81	0.79	1.72	3.43
	9/46	0.51	0.33	0.59	0.62	0.54	0.91	0.75	1.34	3.63
	12/43	0.47	0.32	0.59	0.60	0.57	0.78	0.72	1.31	3.24
	16/39	0.34	0.30	0.51	0.61	0.36	0.79	0.72	0.89	3.31
	20/35	0.42	0.40	0.52	0.49	0.37	0.75	0.76	1.00	2.85
25/30	0.40	0.30	0.51	0.62	0.44	0.72	0.66	1.07	3.16	
DCM	4/51	0.79	0.42	0.74	0.68	0.71	0.78	0.86	1.59	3.44
	5/50	0.64	0.35	0.71	0.70	0.82	0.93	0.86	1.58	3.94
	6/49	0.65	0.35	0.69	0.62	0.64	0.90	0.82	1.52	3.65
	9/46	0.52	0.39	0.58	0.63	0.54	0.89	0.74	1.30	3.59
	12/43	0.47	0.32	0.58	0.61	0.59	0.80	0.77	1.30	3.23
	16/39	0.34	0.30	0.48	0.66	0.36	0.77	0.72	0.82	3.37
	20/35	0.41	0.39	0.51	0.49	0.38	0.76	0.80	0.95	2.70
25/30	0.40	0.29	0.51	0.62	0.44	0.73	0.66	1.07	3.16	
WuDCM	9/46	2.01	1.76	2.48	1.48	0.78	4.37	6.44	4.88	14.86
	12/43	0.69	0.52	0.68	0.64	0.57	0.99	1.11	1.51	3.36
	16/39	0.85	0.38	1.04	0.61	0.82	0.80	0.79	2.33	3.43
	20/35	0.44	0.42	0.49	0.42	0.45	0.79	0.79	1.00	2.72
	25/30	0.48	0.34	0.53	0.60	0.48	0.81	0.76	1.23	3.27

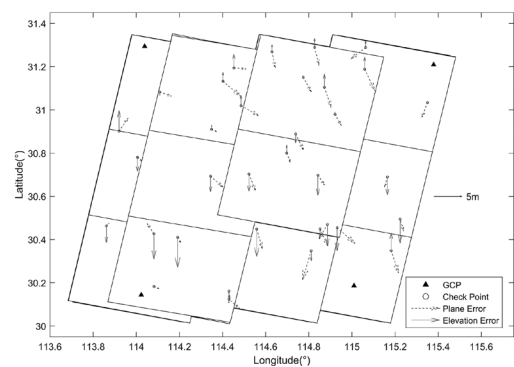
GCP = ground control point; CP = check point; NAD = nadir; BWD = backward sensor; FWD = forward sensor; DCM = direct correct method; WuDCM = the method of Wu *et al.* (2015).



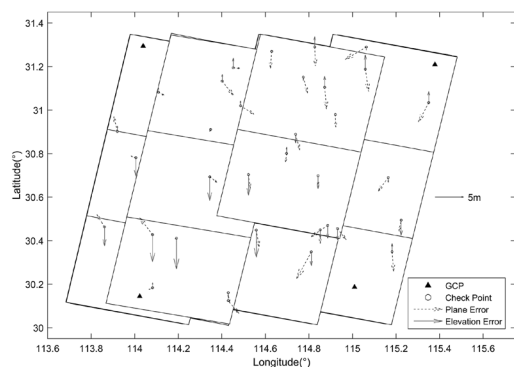
(a)



(b)



(c)



(d)

Figure 3. Residual vector distribution of Hubei area: (a) direct intersection, (b) affine transformation model, (c) direct correct method, (d) WuDCM (from Wu *et al.* 2015).

Table 6. Absolute accuracy of Hubei area with different models.

Model	Number of GCPs/CPs	East (m)		North (m)		Height (m)	
		RMS	Max	RMS	Max	RMS	Max
Direct intersection	0/38	7.71	15.06	8.92	17.98	4.83	10.47
Affine transformation	4/38	1.90	5.03	5.13	7.68	3.50	8.04
DCM	4/38	1.60	3.17	2.49	5.16	1.51	3.04
WuDCM	4/38	1.40	3.77	2.46	4.75	1.56	3.53

GCP = ground control point; CP = check point; RMS = root-mean-square error; Max = maximum error; DCM = direct correct method; WuDCM = the method of Wu *et al.* (2015).

(four-corner control), and more points were used in other situations to guarantee uniform distribution. In addition to the proposed method (DCM), we tested and compared the affine transformation model, the method of Wu *et al.* (2015; WuDCM), and direct reproject. The statistics are shown in Table 5.

As the results for the proposed model demonstrate in Table 5, the image-plane positioning achieved accuracy even better than 1 pixel under four-corner control, which is significantly improved compared with the original positioning accuracy of approximately 10 pixels. Similarly, the stereo accuracy is dramatically improved, with the plane direction better than 2 m and the elevation direction better than 3.5 m. Moreover, the geometric accuracy gradually improved as the number of GCPs increased. All this reveals that the image positioning model refined with the proposed method became more rigorous, and the overall consistency with the ground control system was substantially better. However, accuracy was not effectively improved when a sufficient number (e.g., 25) of points were used, which could have resulted from the limited geometric accuracy of the GCPs themselves and a loss of accuracy due to matching errors. Overall, however, our method for RFM refinement in single-scene mode is feasible and effective.

Compared with the affine transformation model, the proposed method achieved similar or even better results and obtained high geometric accuracy with fewer GCPs. The WuDCM model was subjected to the number of GCPs, and the geometric refinement results were poor, with several pixels level when only the minimum necessary GCPs (nine) were available. This may be due to the lack of redundant observations and the strong correlations between RPCs. However, as the number of GCPs increased, the refinement results increasingly improved, and at the end they were basically consistent with the proposed model. Compared with WuDCM, our method has advantages regarding refinement accuracy and GCP requirements. Although the coefficients are regarded as weighted observations, the WuDCM calculation results are limited because of the strong correlation and overparameterization of the unknowns. In contrast, only the coefficients in the numerator polynomials with weak correlation were corrected in our method; thus, our approach is more stable and the result is more robust.

Block-Adjustment Refinement

The affine transformation model, WuDCM, and the proposed method were again used as adjustment models in this experiment, and the adjustment results estimated with absolute and relative accuracies. The absolute accuracy is evaluated by the check-point coordinate residuals, whereas the relative accuracy is assessed by the reprojection error of the tie points. As this experiment only verified the feasibility of the proposed model in block adjustment, only the four-corner control strategy was used. Detailed statistics are listed in Tables 6 and 7, and the residual vector distributions of the two areas are shown in Figures 3 and 4.

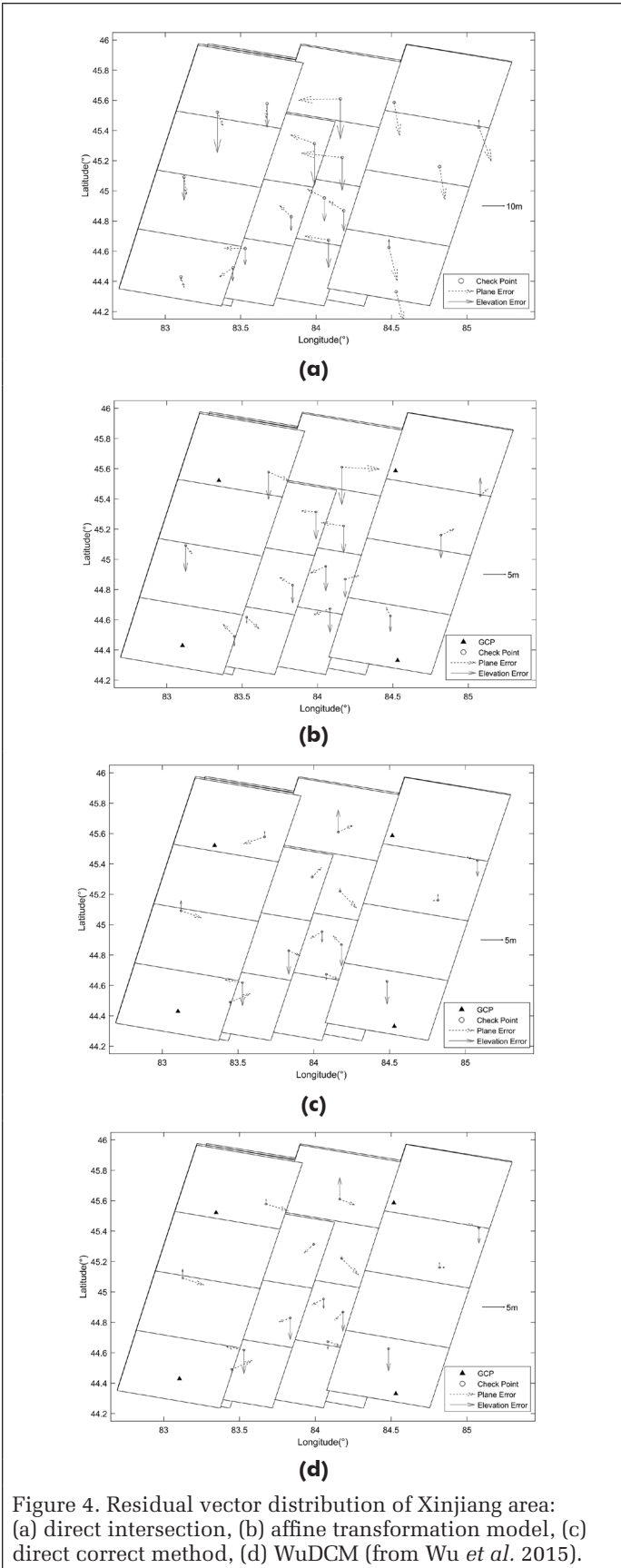


Figure 4. Residual vector distribution of Xinjiang area: (a) direct intersection, (b) affine transformation model, (c) direct correct method, (d) WuDCM (from Wu *et al.* 2015).

Table 7. Absolute accuracy of Xinjiang area with different models.

Model	Number of GCPs/CPs	East (m)		North (m)		Height (m)	
		RMS	Max	RMS	Max	RMS	Max
Direct intersection	0/18	7.45	16.88	7.72	13.81	8.99	16.20
Affine transformation	4/14	3.81	8.51	1.66	2.73	5.40	8.87
DCM	4/14	2.69	4.07	1.43	3.24	2.07	3.24
WuDCM	4/14	2.71	4.13	1.35	3.09	2.11	3.45

GCP = ground control point; CP = check point; RMS = root-mean-square error; Max = maximum error; DCM = direct correct method; WuDCM = the method of Wu *et al.* (2015).

There was an obviously large systematic positioning error in the initial images, as shown in Figures 3a and 4a. After block adjustment with the different geometric refinement methods, the systematic error was effectively compensated, the residual vector distribution was chaotic, and the remaining random error was eliminated. Combined with Tables 6 and 7, the geometric positioning accuracy improved significantly, from 10 m to 5 m, in both plane and height.

In addition, it can be observed from Tables 6 and 7 that the proposed method is better than the affine transformation model at accuracy improvement, in both the horizontal and elevation directions. The root-mean-square and maximum values are smaller than those in the affine transformation model, indicating that the image-error distribution is more uniform and reasonably refined with the proposed method. This phenomenon is similar in both areas. Furthermore, comparing the proposed method with the WuDCM model, we can see that the two methods achieved basically the same results, with only slight differences in some index values. However, it should be noted that the number of RPC corrections in the Hubei and Xinjiang areas were, respectively, 756 and 1134 for WuDCM, versus only 336 and 504 for the DCM. Combined with the analysis under Influence of Individual RPCs on Geometric Positioning, the modification of the coefficients of the denominator term does not generate a significant improvement in accuracy, but instead it imposes higher requirements on the algorithm calculation; therefore, our method has more practical application value.

The relative accuracy is the statistic of reprojection error of the image point, which is mainly related to the random error and can better reflect residual elimination during the refinement process. Tables 8 and 9 show the statistical values of relative accuracy of the two measurement areas after adjustment.

As can be observed in Tables 8 and 9, the original relative accuracy is very poor, at 10 pixels, which is affected by the original RFM geometric accuracy. However, it improved greatly after adjustment with different refinement models. The three models achieved similar results. With respect to root-mean-square error, the relative accuracy in both areas was improved to 0.3 pixel or even better, which satisfies the requirement of seamless stitching. Moreover, the mean values in both directions dropped to 0 and the maximum ones decreased to better than 1.8 pixels, demonstrating that the adjustment refinement results were unbiased. The high relative accuracy proved the efficiency of our method in constructing a robust network structure and securing internal consistency in accuracy.

Conclusions

This article presents a new RFM refinement approach based on directly correcting the dominant coefficients to improve geometric positioning accuracy. Through theoretical analysis and experimental validation, the following conclusions can be drawn.

Table 8. Relative accuracy of Hubei area with different models.

Model	Number of image points	RMS (pixels)		Mean (pixels)		Max (pixels)	
		x	y	x	y	x	y
Direct intersection	17 126	6.12	7.25	0.31	0.73	21.34	22.30
Affine transformation		0.21	0.20	0.00	0.00	1.34	-1.35
DCM		0.21	0.20	0.00	0.00	1.38	1.36
WuDCM		0.19	0.18	0.00	0.00	1.39	1.38

RMS = root-mean-square error; Mean = mean error; Max = maximum error; DCM = direct correct method; WuDCM = the method of Wu *et al.* (2015).

Table 9. Relative accuracy of Xinjiang area with different models.

Model	Number of image points	RMS (pixels)		Mean (pixels)		Max (pixels)	
		x	y	x	y	x	y
Direct intersection	22 622	4.70	4.67	-0.98	-0.58	14.09	16.50
Affine transformation		0.20	0.17	0.00	0.00	-1.30	-1.09
DCM		0.22	0.19	0.00	-0.00	1.25	1.72
WuDCM		0.21	0.17	0.00	-0.00	1.30	1.71

RMS = root-mean-square error; Mean = mean error; Max = maximum error; DCM = direct correct method; WuDCM = the method of Wu *et al.* (2015).

The special physical meaning of each RPC cannot be rigorously derived, but the correlation exists in reality, and there is even a strong correlation between parts of RPCs. The influence of individual RPCs on geometric positioning accuracy is inconsistent, and only the dominant coefficients—the first few terms of the numerator polynomials—dominate the geometric accuracy; hence, an improvement in the numerical precision of these determinants will greatly improve the image-geometry accuracy. The proposed approach takes into account the different influence of RPCs on geopositioning, and the weak correlation, having the characteristics of a simple model and convenient and fast calculation, can effectively improve the geometric accuracy. Further study will focus on the adaptability of this method to other satellite images and try to perform the combined block adjustment of large-scale multisource satellite remote sensing images.

Acknowledgments

This work was supported by the Key Application Generic Technology of China High-resolution Earth Observation System under Grant 11-Y20A13-9001-17/18. The authors also thank the anonymous reviewers for their constructive comments and suggestions.

References

Ager, T. P. 2003. Evaluation of the geometric accuracy of Ikonos imagery. *Proceedings of SPIE* 5093:613–620.

Aguilar, M. A., M.D.M. Saldaña and F. J. Aguilar. 2013. Assessing geometric accuracy of the orthorectification process from GeoEye-1 and WorldView-2 panchromatic images. *International Journal of Applied Earth Observation and Geoinformation* 21:427–435.

Di, K., R. Ma and R. Li. 2003. Geometric processing of Ikonos stereo imagery for coastal mapping applications. *Photogrammetric Engineering and Remote Sensing* 69 (8):873–879.

Fraser, C. S., G. Dial and J. Grodecki. 2006. Sensor orientation via RPCs. *ISPRS Journal of Photogrammetry and Remote Sensing* 60 (3):182–194.

Fraser, C. S. and H. B. Hanley. 2003. Bias compensation in rational functions for Ikonos satellite imagery. *Photogrammetric Engineering and Remote Sensing* 69 (1):53–57.

Fraser, C. S. and H. B. Hanley. 2005. Bias-compensated RPCs for sensor orientation of high-resolution satellite imagery. *Photogrammetric Engineering and Remote Sensing* 71 (8):909–915.

Fraser, C. S., H. B. Hanley and T. Yamakawa. 2002. High-precision geopositioning from Ikonos satellite imagery. Pages 22–26 in *Proceedings of Annual Conference of American Society of Photogrammetry and Remote Sensing*, held in Washington, D.C., 21–26 April 2002. Edited by J. Editor. City, St.: Publisher.

Grodecki, J. and G. Dial. 2003. Block adjustment of high-resolution satellite images described by rational polynomials. *Photogrammetric Engineering and Remote Sensing* 69 (1):59–68.

Habib, A., S. W. Shin, K. Kim, C. Kim, K.-I. Bang, E.-M. Kim and D.-C. Lee. 2007. Comprehensive analysis of sensor modeling alternatives for high resolution imaging satellites. *Photogrammetric Engineering and Remote Sensing* 73 (11):1241–1251.

Holland, D. A., D. S. Boyd and P. Marshall. 2006. Updating topographic mapping in Great Britain using imagery from high-resolution satellite sensors. *ISPRS Journal of Photogrammetry and Remote Sensing* 60 (3):212–223.

Hu, Y. and C. V. Tao. 2002. Updating solutions of the rational function model using additional control information. *Photogrammetric Engineering and Remote Sensing* 68 (7):715–723.

Jeong, J., J. Kim, T. Kim and S. Rhee. 2016. Evaluation of the performance of KOMPSAT-3 stereo images in terms of positioning and the generation of digital surface models. *Remote Sensing Letters* 7 (10):955–964.

Jiang, Y., Z. Cui, G. Zhang, J. Wang, M. Xu, Y. Zhao and Y. Xu. 2018. CCD distortion calibration without accurate ground control data for pushbroom satellites. *ISPRS Journal of Photogrammetry and Remote Sensing* 142:21–26.

Jiang, Y.-H., G. Zhang, P. Chen, D.-R. Li, X.-M. Tang and W.-C. Huang. 2015. Systematic error compensation based on a rational function model for Ziyuan1-02C. *IEEE Transactions on Geoscience and Remote Sensing* 53 (7):3985–3995.

Liu, J.-H., B. Jia, T. Jiang and G.-W. Jiang. 2013. Extrapolative positioning of RPC model of TH-1 satellite three-line imagery. *Geomatics & Spatial Information Technology* 2013 (9):20–21, 25.

Long, T., W. Jiao and G. He. 2014. Nested regression based optimal selection (NRBOS) of rational polynomial coefficients. *Photogrammetric Engineering and Remote Sensing* 80 (3):261–269.

Lutes, J. 2004. Accuracy analysis of rational polynomial coefficients for Ikonos imagery. Pages 23–28 in *Proceedings of Annual Conference American Society Photogrammetry and Remote Sensing*, held in Denver, Colo., 23–28 May 2004. Edited by J. Editor. City, St.: Publisher.

Madani, M.. 1999. Real-time sensor-independent positioning by rational functions. Pages 64–75 in *Proceedings of ISPRS Workshop on Direct Versus Indirect Methods of Sensor Orientation*, held in Barcelona, Spain, DD–DD Month 1999. Edited by J. Editor. City, St.: Publisher.

Noguchi, M., C. S. Fraser, T. Nakamura, T. Shimono and S. Oki. 2004. Accuracy assessment of QuickBird stereo imagery. *The Photogrammetric Record* 19 (106):128–137.

Osawa, Y. 2004. Optical and microwave sensors on Japanese mapping satellite—ALOS. *Japan Aerospace Exploration Agency* 35:309–312.

Pan, H., G. Zhang, X. Tang, D. Li, X. Zhu, P. Zhou and Y. Jiang. 2013. Basic products of the ZiYuan-3 satellite and accuracy evaluation. *Photogrammetric Engineering and Remote Sensing* 79 (12):1131–1145.

Poon, J., C. S. Fraser, C. Zhang, L. Zhang and A. Gruen. 2005. Quality assessment of digital surface models generated from IKONOS imagery. *The Photogrammetric Record* 20 (110):162–171.

- Rupnik, E., M. P. Deseilligny, A. Delorme and Y. Klinger. 2016. Refined satellite image orientation in the free open-source photogrammetric tools Apero/MicMac. *ISPRS Annals of the Photogrammetry, Remote Sensing and Spatial Information Sciences* III (1):83–90.
- Stumpf, A., J.-P. Malet and C. Delacourt. 2017. Correlation of satellite image time-series for the detection and monitoring of slow-moving landslides. *Remote Sensing of Environment* 189:40–55.
- Tang, S., B. Wu and Q. Zhu. 2016. Combined adjustment of multi-resolution satellite imagery for improved geo-positioning accuracy. *ISPRS Journal of Photogrammetry and Remote Sensing* 114:125–136.
- Tang, X., G. Zhang, X. Zhu, H. Pan, Y. Jiang, P. Zhou and X. Wang. 2013. Triple linear-array image geometry model of ZiYuan-3 surveying satellite and its validation. *International Journal of Image and Data Fusion* 4 (1):33–51.
- Tao, C. V. and Y. Hu. 2001. A comprehensive study of the rational function model for photogrammetric processing. *Photogrammetric Engineering and Remote Sensing* 67 (12):1347–1357.
- Tong, X., S. Liu and Q. Weng. 2010. Bias-corrected rational polynomial coefficients for high accuracy geo-positioning of QuickBird stereo imagery. *ISPRS Journal of Photogrammetry and Remote Sensing* 65 (2):218–226.
- Topan, H., A. Cam, M. Özendi, M. Oruç, K. Jacobsen and T. Ta kanat. 2016. Pléiades project: Assessment of georeferencing accuracy, image quality, pansharpening performance and DSM/DTM quality. *The International Archives of the Photogrammetry, Remote Sensing and Spatial Information Sciences* XLI (B1):503–510.
- Toutin, T. 2004. DTM generation from Ikonos in-track stereo images using a 3D physical model. *Photogrammetric Engineering and Remote Sensing* 70 (6):695–702.
- Wang, J., K. Di and R. Li. 2005. Evaluation and improvement of geopositioning accuracy of IKONOS stereo imagery. *Journal of Surveying Engineering* 131 (2):35–42.
- Wang, M., Y. Cheng, X. Chang, S. Jin and Y. Zhu. 2017. On-orbit geometric calibration and geometric quality assessment for the high-resolution geostationary optical satellite GaoFen4. *ISPRS Journal of Photogrammetry and Remote Sensing* 125:63–77.
- Wang, T., G. Zhang, D. Li, X. Tang, Y. Jiang, H. Pan and X. Zhu. 2014. Planar block adjustment and orthorectification of ZY-3 satellite images. *Photogrammetric Engineering and Remote Sensing* 80 (6):559–570.
- Wu, B., S. Tang, Q. Zhu, K.-Y. Tong, H. Hu and G. Li. 2015. Geometric integration of high-resolution satellite imagery and airborne LiDAR data for improved geopositioning accuracy in metropolitan areas. *ISPRS Journal of Photogrammetry and Remote Sensing* 109:139–151.
- Xu, K., Y. Jiang, G. Zhang, Q. Zhang and X. Wang. 2017. Geometric potential assessment for ZY3-02 triple linear array imagery. *Remote Sensing* 9 (7):658–675.
- Zheng, M. and Y. Zhang. 2016. DEM-aided bundle adjustment with multisource satellite imagery: ZY-3 and GF-1 in large areas. *IEEE Geoscience and Remote Sensing Letters* 13 (6):880–884.

Temporal Validation of Four LAI Products over Grasslands in the Northeastern Tibetan Plateau

Gaofei Yin, Ainong Li, Zhengjian Zhang, and Guangbin Lei

Abstract

Time series of leaf area index (LAI) products are now widely used, and the temporal validation is the prerequisite for their proper application. However, a systematical comparison between different products using both direct and indirect methods is still lacking. The objective of this paper is to assess and compare the temporal performances of four LAI products: Moderate Resolution Imaging Spectroradiometer (MODIS) LAI (MOD15A2, MOD15A2h, Geoland2 Version 1 (GEOV1), and Global Land Surface Satellite (GLASS). The study area, which is dominated by grasslands, is located in the northeastern Tibetan Plateau (TP), and temperature is the main stress factor affecting grass growth. Both a correlation analysis with temperature and a direct comparison with temporally continuous LAI reference maps were implemented in our temporal validation experiments. The results show that no single product can capture the rapid change and the seasonal trend in LAI simultaneously, and the compositing period used in each product determines the quality of the corresponding LAI time series. The MOD15A2 and MOD15A2h products, which have short compositing windows (eight days), are suitable for detecting rapid change. A grazing-induced biomass decrease that occurred around day of year 205 in 2014 in our study area was clearly revealed in these two products. For the GEOV1 and GLASS products, which have compositing windows of 30 days and 1 year, respectively, the grazing date was shifted (GEOV1) or even invisible (GLASS). However, products with prolonged compositing windows may be more robust to observation noise, and the resulting products may be suitable for capturing the seasonal trend. This study highlights that the concurrent use of data from various sensors onboard different satellites, and the introduction of new generations of satellites (e.g., Gaofen-6), are two promising ways to further improve existing LAI time series.

Introduction

The leaf area index (LAI), which is a key vegetation structure and function parameter, describes the surface area available for energy and mass exchanges between vegetation and the atmosphere. Currently, several coarse-resolution (~1 km) LAI products are routinely produced, including the Moderate Resolution Imaging Spectroradiometer (MODIS) (Myneni *et al.* 2002), Geoland2 Version 1 (GEOV1) (Baret *et al.* 2013), and Global Land Surface Satellite (GLASS) (Xiao *et al.* 2014) products. These LAI products are widely used as proxy indicators of vegetation status to monitor ecosystem variations in response to climate change and anthropogenic activities (Jiapaer *et al.* 2015). Although the LAI products have been extensively

validated, spanning a wide range in space (Camacho *et al.* 2013; Fang, Wei, and Liang 2012; Garrigues *et al.* 2008), their performance in time series is still not clear.

To assess their performance in time series, temporal validations (TVs) of LAI products are needed (Fang *et al.* 2019b; Xie *et al.* 2019). Current TV studies perform two categories of analyses, specifically indirect TVs and direct TVs. An indirect TV compares the relationship between LAI trends and key meteorological variables in areas where these variables limit plant growth (Yan *et al.* 2016b). On the other hand, a direct TV uses multiple LAI reference maps within a single year, generally derived from up-scaling the *in situ* LAI measurements, to assess the temporal dynamics of uncertainty in LAI products (Fang *et al.* 2019a; Yin *et al.* 2017a). Generating temporally continuous LAI reference maps is the key issue in performing direct TVs (Yin *et al.* 2017a). To the best of our knowledge, there are very few studies, if they exist, to implement both direct and indirect TVs simultaneously to systematically assess the temporal performance of LAI products.

The objective of this paper is to fill the gap existing in the TV of LAI products. To fulfill the research objective, both the direct and indirect TV methods were used for four commonly used LAI products, i.e., MOD15A2 (Myneni *et al.* 2002), MOD15A2h (Yan *et al.* 2016a; Yan *et al.* 2016b), GEOV1 (Baret *et al.* 2013; Camacho *et al.* 2013), and GLASS (Xiao *et al.* 2014). The remainder of the paper is structured as follows. In the next section, we introduce the data and method used in this study. The “Results” section presents both the direct and indirect TV results; a discussion is presented in the section “Discussion”, and conclusions are given in the last section.

Materials and Methods

Study Area and Field Data Collection

The research was conducted in a 5 km × 5 km region centered on ~33°55′ N, 102°51′ E that is close to Huahu Lake in the Zoige National Nature Reserve (Figure 1a). It is located at the northeastern edge of the Tibetan Plateau (TP). The study area is mainly covered by alpine meadows, which have substantial ecological vulnerability (Li *et al.* 2012). In recent years, the degradation of grasslands has become more and more serious, which is directly due to the influence of human activities, such as excessive grazing (Roy *et al.* 2014). The climate is cold and wet, and the temperatures, which range from -15°C to 15°C (as measured at a nearby meteorological station; see Figure 2), are the main limited factor for the temporal variations in the grasslands in our study area (Hansen *et al.* 2013). The spatial variations of grass growth are mainly controlled by altitude, and it ranges from 3400 m to 3500 m (see Figure 1b) according to the ASTER GDEM V3 dataset (METI and NASA 2019).

Gaofei Yin* is with the Faculty of Geosciences and Environmental Engineering, Southwest Jiaotong University, Chengdu 610031, China (yingf@swjtu.edu.cn).

Ainong Li*, Zhengjian Zhang, and Guangbin Lei are with the Research Center for Digital Mountain and Remote Sensing Application, Institute of Mountain Hazards and Environment, Chinese Academy Sciences, Chengdu 610010, China. (ainongli@imde.ac.cn)

*Corresponding authors.

Photogrammetric Engineering & Remote Sensing
Vol. 86, No. 4, April 2020, pp. 225–233.
0099-1112/20/225–233

© 2020 American Society for Photogrammetry
and Remote Sensing
doi: 10.14358/PERS.86.4.225

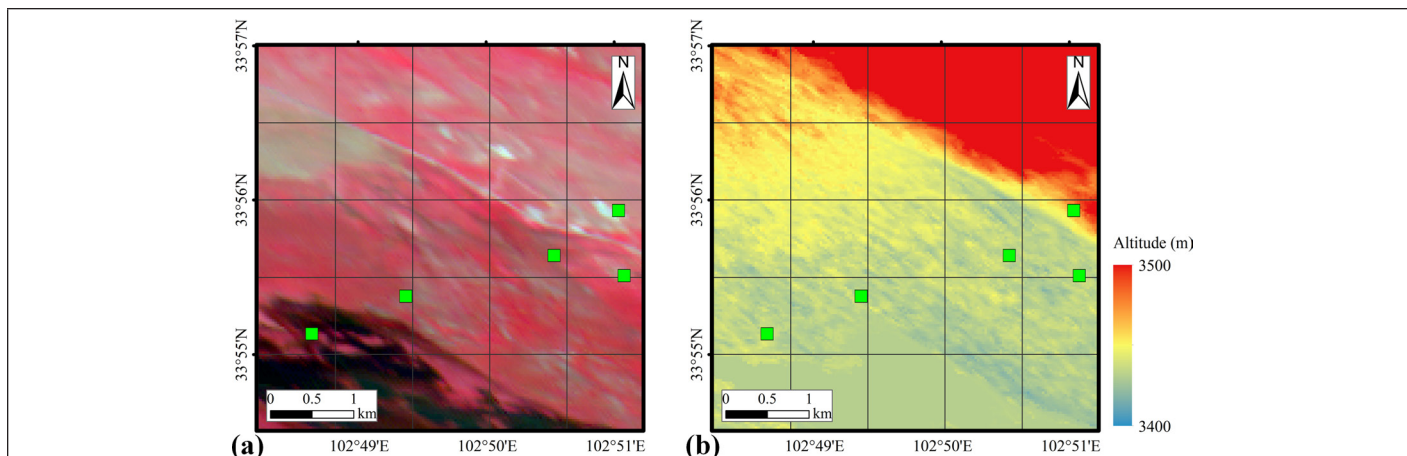


Figure 1. (a) The composite image of *HJ-1A*'s 4, 3, and 2 bands (corresponding to R, G, and B colors); (b) elevation map. The maps were overlaid by a grid representing the pixels of the MOD15A2 LAI product, which has a nominal resolution of 1 km × 1 km. The study area is located in the northeastern TP. The green points represent the locations of the sampling plots.

In our study area, we selected five homogeneous permanent plots, each of which covered a 100 m × 100 m area. To capture the spatial heterogeneity within the study area, the plots were distributed along the northeast-southwest altitudinal gradient. During 2014, eight field campaigns spanning the whole growing season were carried out, and the specified experimental dates were days of the year (DOY) 124, 154, 169, 184, 205, 237, 258, and 296 (see Figure 3). During each field campaign, four square (0.2 m × 0.2 m) quadrats were chosen in each plot. The location of each quadrat was recorded using a portable Global Positioning System. It should be noted that the four quadrats were randomly chosen in a limited homogeneous ~30 m × 30 m area, rather than representing the whole plot. For each field campaign, the quadrats were selected as far as possible from the quadrats sampled earlier, unless the regrowth after harvest had compensated for the loss of biomass. In summary, we adopted a two-level hierarchical sampling design: the five spatially fixed plots along the altitudinal gradient were used to capture the heterogeneity at the scale of the whole study area (5 km × 5 km), and the four randomly distributed quadrats within each plot were used to characterize the heterogeneity at the 30 m × 30 m scale. Finally, the eight field campaigns during 2014 can capture the temporal variation of LAI. The above treatments ensure that the derived reference maps represent the spatiotemporal dynamics in this grassland ecosystem.

The field measured LAI was determined using a regression relationship between the aboveground biomass and the leaf area. For each quadrat, the aboveground grass was mowed and transported to the laboratory. We then measured the harvested biomass after oven-drying the sample at 80°C for 48 hours. Sixteen quadrats were randomly chosen, and their corresponding total leaf area for each quadrat was measured using an LI-3000C portable leaf area meter. In addition, the specific leaf area, i.e., the leaf area per leaf dry weight, was then retrieved through the regression analysis between biomass and leaf area (see Figure 4). Finally, the LAI for each quadrat was estimated using the following formula:

$$L = B \times w_l / 0.04, \quad (1)$$

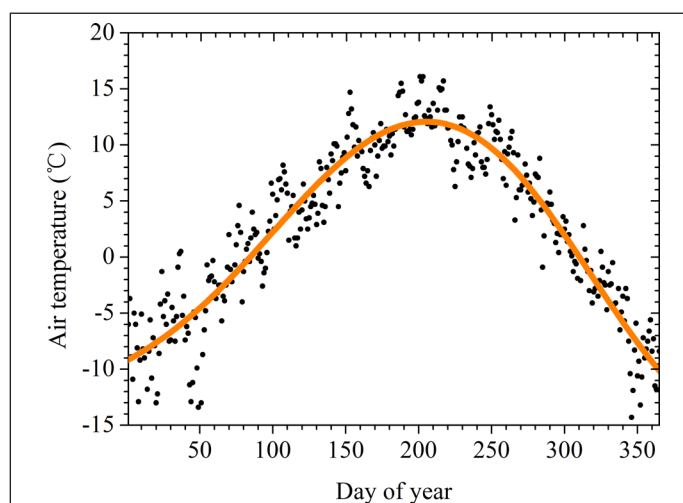


Figure 2. Temporal course of daily air temperatures (dots) measured in 2014 at a nearby meteorological station. The solid line represents the corresponding fitted line using a double logistic function.

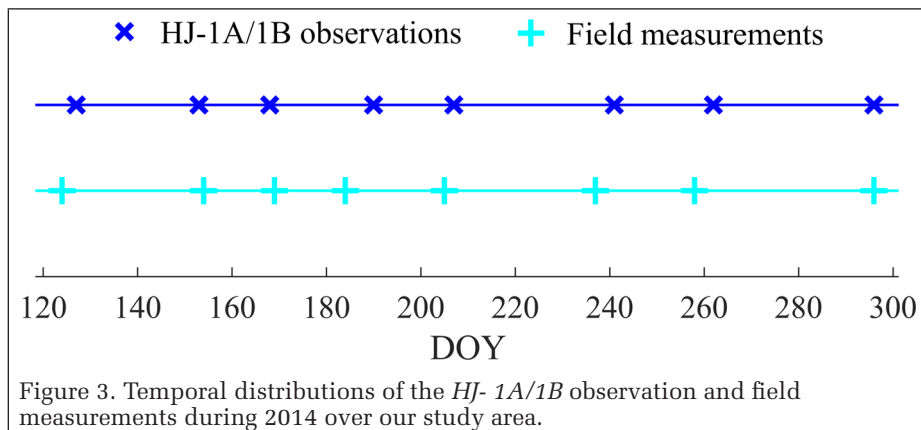
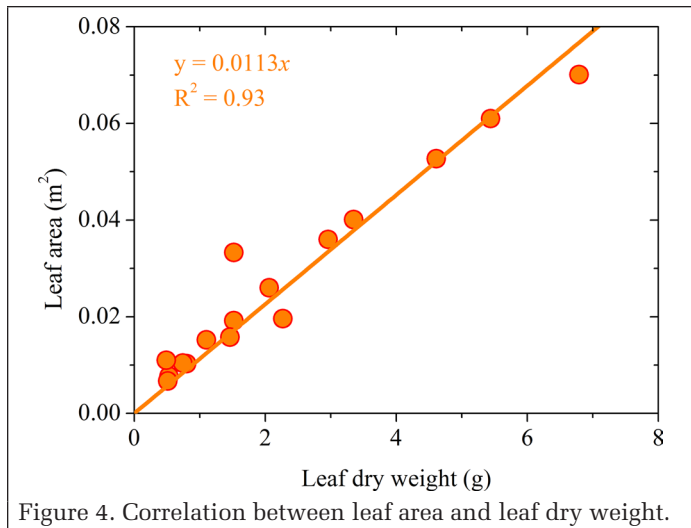


Figure 3. Temporal distributions of the *HJ-1A/1B* observation and field measurements during 2014 over our study area.

where L is the leaf area index, B is the aboveground biomass, w_l is the specific leaf area (0.0113 m²/g), and the denominator denotes the area of the quadrat (0.2 m × 0.2 m). The strong correlation between leaf area and biomass (Figure 4) gives us confidence about the applicability of Equation 1.



Development of LAI Reference Maps

A critical issue in the validation of coarse-resolution LAI products is the scale discrepancy between field measurements and the retrieved values. The hierarchical four-stage validation approach (Morisette *et al.* 2006) was used to upscale the field measurements to the scale of coarse resolution pixels, using the Chinese *Huan Jing (HJ)-1A/1B* charge coupled device (CCD) camera images as the bridge.

The *HJ-1A/1B* satellites are small, civilian, Earth-observing satellites, and each satellite carries two CCD cameras, which are named CCD1 and CCD2 and have a 700 km swath width. They provide a unique opportunity to collect remote sensing observations with high spatial and temporal resolutions, with a revisit period of two days and a pixel width of 30 m. The *HJ-1A/1B* CCD cameras have three visible bands (blue (B): 430–520 nm, green (G): 520–600 nm, and red (R): 630–690 nm) and one near-infrared band (NIR: 760–900 nm) band. Eight cloud-free images acquired on DOYs 127, 153, 168, 190, 207, 241, 262, and 296, which correspond to the eight field campaigns in sequence (see Figure 3), were obtained. The temporal mismatch between field and satellite observations was very small, and the largest temporal disparity is six days (field measurement and satellite image acquisition occurred on DOY 184 and 190, respectively), and this would not incur too much uncertainty because the vegetation was growing during the growing peak and its status was relatively stable. The images were processed to obtain the surface reflectance after applying geometric and atmospheric corrections according to the method of (Wen *et al.* 2015).

The field measured LAI values from the four quadrats within each plot were first averaged to provide a reference value at the scale of an *HJ* image pixel, and then the corresponding normalized difference vegetation index (NDVI) value was extracted from the temporally synchronous image. In total, 40 reference

LAI-NDVI pairs were compiled. An empirical regression modeling approach was used to derive the transfer functions that relate the field measurements to the corresponding NDVI values. Three commonly used functions, i.e., liner, exponential, and logarithmic, were tested and the one with the best fitting capacity was selected during the upscaling procedure.

LAI Products

In this study, the MOD15A2, MOD15A2h, GEOV1, and GLASS LAI products were validated, and their main characteristics can be found in Table 1.

MOD15A2 and MOD15A2h LAI Products

The MOD15A2 LAI product has a spatial resolution of 1 km and a temporal resolution of eight days. The main algorithm is based on lookup tables (LUTs) obtained from a three-dimensional radiative transfer model. Given daily land surface bidirectional reflectance factors and their uncertainties, the algorithm finds the best LAI estimate from a biome-specific LUT. A backup empirical method based on the relationships between the NDVI and LAI is used to produce estimates with relatively poor quality. LAI is first produced daily. The LAI value corresponding to the maximum fraction of photosynthetically active radiation (FPAR) is selected as the final retrieval result over the eight-day compositing period. Vegetation clumping is accounted for in the simulation of canopy reflectance, so the retrieval corresponds to the true LAI (Myneni *et al.* 2002).

The MOD15A2h LAI product, which belongs to the latest Collection 6 MODIS LAI, is an update of MOD15A2 (Myneni and Park 2015; Yan *et al.* 2016a; Yan *et al.* 2016b). The most important change in MOD15A2h is that the products are being produced at a spatial resolution of 500 m instead of 1 km, as in MOD15A2. To achieve this, a new version of MODIS surface reflectances (MOD09GA C6) is used to replace the previously used 1-km intermediate dataset (MODIS daily aggregated surface reflectance product, MODAGAGG). Because of the low quality of the retrievals obtained using the backup algorithm, for the MOD15A2 and MOD15A2h products, only the values retrieved with the main algorithm were used in this study.

GEOV1 LAI Product

The GEOV1 LAI product is developed within the framework of the Copernicus Land service and has a spatial resolution of 1/112° and a temporal frequency of 10 days. It relies on neural networks trained to generate the “best estimates” of LAI obtained by fusing the MODIS and CYCLOPES products. Once trained, these networks were run to provide LAI values from SPOT/VEGETATION directionally normalized reflectances. The normalization is performed by inversion of a bidirectional reflectance distribution function (BRDF) model every 10 days within the 30-day composite period. Therefore, the temporal resolution (10 m) and compositing window (30 m) of GEOV1 are different. The GEOV1 LAI values represent a combination of true and effective LAI values, because the MODIS and CYCLOPES LAI estimates correspond to true and effective LAI values, respectively (Baret *et al.* 2013; Camacho *et al.* 2013).

Table 1. Characteristics of the global LAI products under study.

Product	GSD	Frequency	Main algorithm	LAI definition	Reference
MOD15A2	1 km	8 days	LUT based on three-dimensional (3D) RTM	tLAI	(Knyazikhin 1999; Myneni <i>et al.</i> 2002)
MOD15A2h	500 m	8 days	LUT based on 3D RTM	tLAI	(Myneni and Park 2015; Yan <i>et al.</i> 2016a; Yan <i>et al.</i> 2016b)
GEOV1	1/112°	10 days	ANN trained with existing products	Fused with tLAI and eLAI	(Baret, Pacholczyk, and Lacaze 2012; Baret <i>et al.</i> 2013; Camacho <i>et al.</i> 2013)
GLASS	1 km	8 days	GRNN trained with existing products	tLAI	(Xiao 2014; Xiao <i>et al.</i> 2014)

LUT, RTM, ANN, GRNN, tLAI, and eLAI stand for “lookup table”, “radiative transfer model”, “artificial neural network”, “general regression neural network”, “true LAI”, and “effective LAI”, respectively.

GLASS LAI Product

GLASS has a temporal resolution of eight days and spans from 1982 until the present. For the period extending from 2000 to the present, the product was derived from reprocessed MODIS land surface reflectance data and has a spatial resolution of 1 km. The GLASS LAI product was derived using General Regression Neural Networks (GRNNs). The GRNNs were trained with a database that was generated from the fusion of MODIS data and clumping-corrected CYCLOPES LAI products. Therefore, it corresponds to true LAI. The reprocessed MODIS reflectance data from an entire year were input into the GRNNs to estimate the 1-year LAI profiles. Obviously, the temporal resolution and compositing window of GLASS are quite different: eight days and one year, respectively. Thanks to its long compositing window, the GLASS LAI product has the ability to generate temporally continuous and smooth LAI profiles (Xiao *et al.* 2014).

Evaluation of the LAI Products

The direct TV was implemented by comparing the LAI products with the LAI reference maps date by date. This comparison was implemented by comparing the mean values of the 5 km × 5 km study area calculated from the LAI products and reference maps, respectively. This aggregation process can reduce the influence of geolocation errors and the difference in the point spread function.

Meanwhile, the indirect TV was conducted through a correlation analysis between the LAI values and temporal profiles

of temperature during the growing season in 2014. The temperature data were collected from a nearby meteorological station (see Figure 2). When implementing the correlation, the mean air temperature during each compositing period was used. The temperature was selected, rather than other meteorological variables, because it is the main stress factor for grass growth in our study area (Hansen *et al.* 2013).

Results

LAI Reference Maps

The exponential relationship between LAI and NDVI was found to be better than other regression types. The final transfer function established through the regression analysis based on the 40 reference LAI-NDVI pairs is shown in Figure 5. NDVI correlates well with LAI, and the transfer function can explain 72% of the variation in LAI, with a root-mean-square error (RMSE) equal to 0.34. This transfer function was then applied to the eight NDVI maps calculated using the *HJ* images. The generated reference LAI maps are shown in Figure 6.

The temporal variation in grasslands covering almost the whole growing period was well captured by the LAI reference maps (see Figure 6). At the beginning of our study period (DOY 124), the grass had just started to grow and the area had low LAI values (ranging from 0 to 1.0 in the study area). Then, from DOY 124 to 184, the grass grew rapidly to its growth peak. During the growth peak, the grass had great growth potential and experienced ideal hydrothermal conditions. However, the mean LAI in our study area dropped quickly from 2.5 to 2.0. The field campaign that took place on DOY 205 found that this drop was caused by livestock grazing. After the grazing took place, some patches with low LAI regrew to nearly equal and even larger LAI values on DOY 235, compared to DOY 184. This regrowth was caused by overcompensation effects (Li *et al.* 2010). After DOY 237, the grass continued to decay, and the mean LAI value of the study area declined from 2.0 on DOY 237 to 1.1 on DOY 296.

Direct Temporal Validation

Within our study area, all the LAI products display similar seasonality and reproduce the reference LAI dynamics very well (Figure 7). The main discrepancies appear around DOY 205, when heavy grazing was recorded during the field campaign. Both the MOD15A2 and MOD15A2h products capture this grazing event, and a sharp drop was observed. In fact, the temporal profile of the GEOV1 product also shows a sharp drop, but it is shifted to a later date (i.e., the right side of the plot). In contrast, the GLASS LAI time series do not represent this

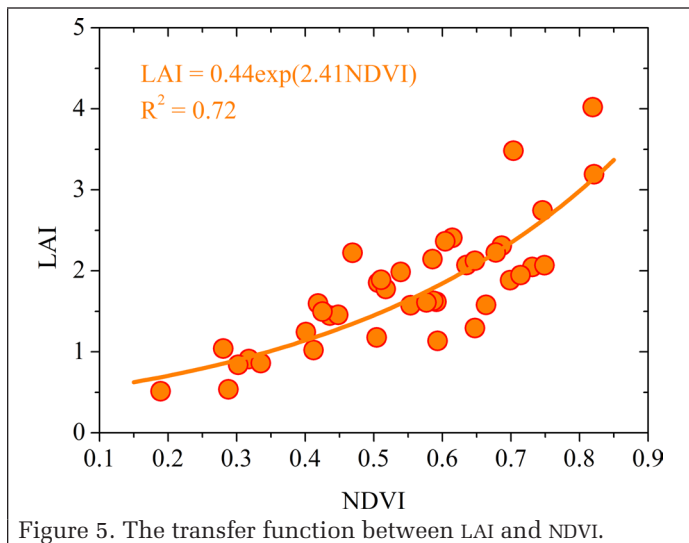


Figure 5. The transfer function between LAI and NDVI.

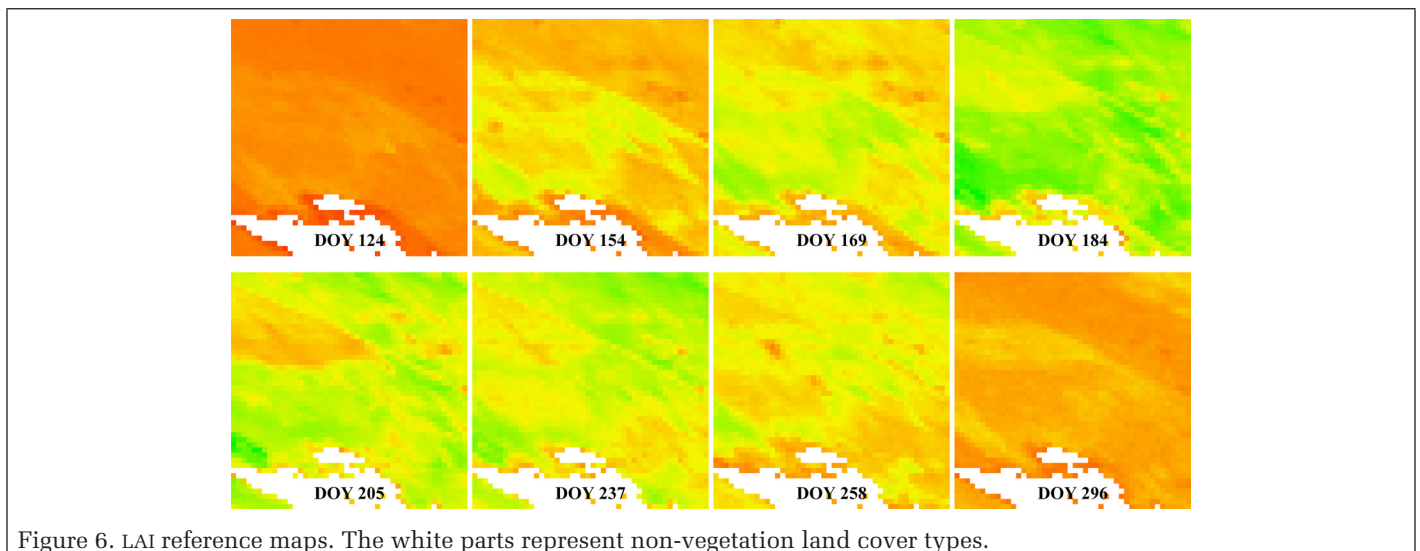


Figure 6. LAI reference maps. The white parts represent non-vegetation land cover types.

grazing-caused drop, i.e., it contains no direct information on livestock grazing, and the LAI value decreases slowly after the growth peak.

The MOD15A2 and MOD15A2h present very noisy and even discontinuous profiles due to insufficient remote sensing observations, and this makes them sensitive to residual clouds (Flood *et al.* 2013). Anomalously low LAI values and a gap in both MOD15A2 and MOD15A2h on DOYs 169 and 217, respectively, were observed. In contrast, GEOV1 and GLASS display smoother temporal variations thanks to their longer compositing windows.

Moreover, an interesting phenomenon is observed when comparing the MOD15A2 and MOD15A2h LAI products, which use the same retrieval algorithm but have different spatial resolutions: the magnitude of the LAI profile from MOD15A2h is larger than that from MOD15A2, especially during the growing peak. This is because of the scale effect, which derives from both the heterogeneity of land surface and the nonlinear characteristics of the retrieval model (Yan *et al.* 2016b). The underestimation of LAI products compared to their counterparts with high spatial resolution was also reported in (Yin *et al.* 2015).

The scatter plots between the reference and estimated LAI from the four products are shown in Figure 8. Compared with the uncertainty threshold established by the Global Climate Observation System (GCOS) (2011), i.e., max (0.5, 20%), the MOD15A2 and MOD15A2h products performed unsatisfactorily in our study area and revealed an obvious underestimation. The consistence between the MOD15A2h and reference LAI was rather low with $R^2 = 0.59$, caused by the abnormal low LAI observed on DOY 169 (see Figure 7). In contrast, the accuracy of GEOV1 and GLASS LAI was satisfactory for grassland, with most of the dots within the boundary defined by the GCOS uncertainty threshold (GCOS 2011).

Indirect Temporal Validation

Several studies have reported the correlation between LAI and meteorological variables that govern plant growth and have demonstrated the potential of LAI products to track meteorological change (Jiapaer *et al.* 2015; Yan *et al.* 2016b). However, the difference in the capacity of different LAI products to capture meteorological variability is still not clear. The correlations of the four LAI products with air

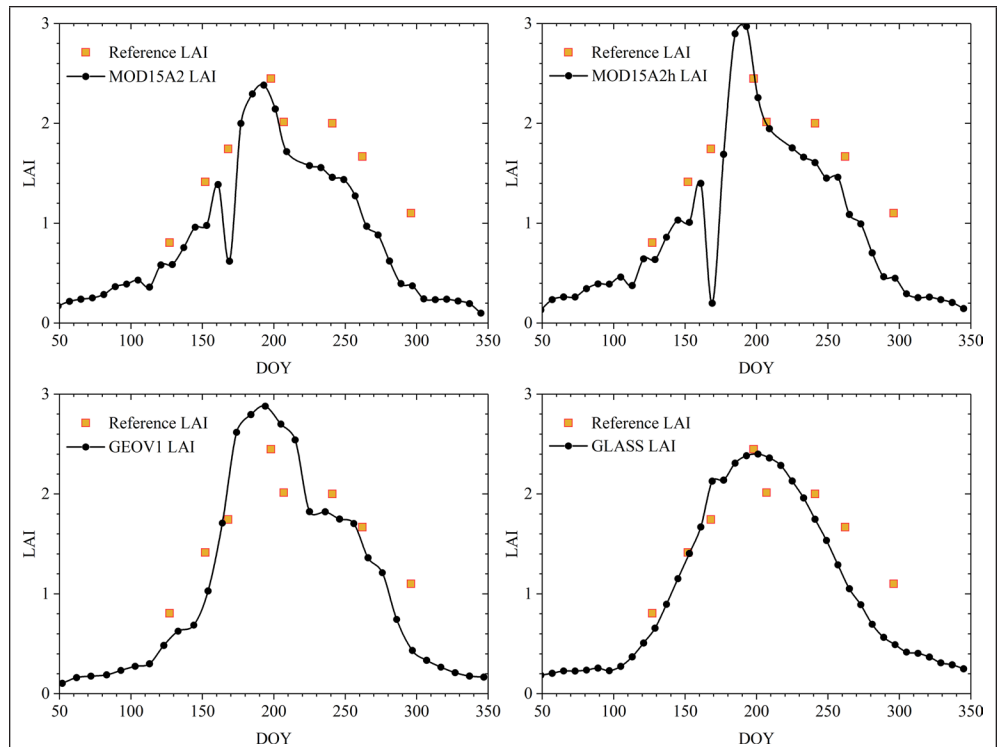


Figure 7. Seasonal trajectories of different LAI products. The reference LAI is also drawn in each plot.

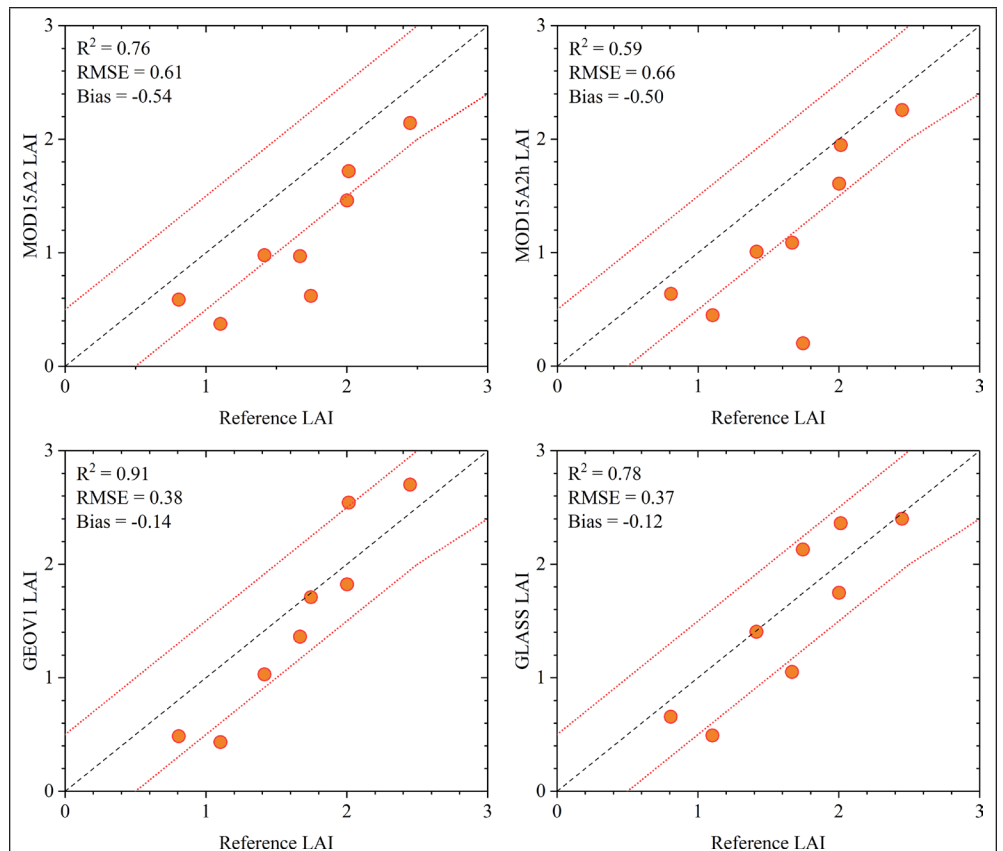


Figure 8. Direct comparison between the reference LAI and the four LAI products in our study area. The red dotted lines represent the accuracy boundaries (max (0.5, 20%)) established by the GCOS.

temperature, which is the main stress factor in our study area, were analyzed and are shown in Figure 9. It should be noted that the anomalously low LAI values observed in the MOD15A2 and MOD15A2h LAI products on DOY 169 were filtered out before the analysis was performed. It can be clearly seen that the four LAI products all display statistically sound correlations with air temperature; however, the correlation coefficient (R^2) values differ among the products. The MOD15A2 and MOD15A2h products have similar R^2 values (0.63 and 0.60, respectively), which are lower than those obtained from the GEOV1 (0.71) and GLASS (0.72) products.

Discussion

Uncertainties in the Validation

The TV for the four selected LAI products, i.e., MOD15A2, MOD15A2h, GEOV1, and GLASS, was implemented through both direct and indirect methods. The performance of the four LAI products in temporal dimension was accordingly analyzed. Several sources of uncertainty exist in this research.

To make the indirect TV temporally consistent with the direct TV, only a one-year temperature temporal profile was used in the correlation analysis. In addition, to address the concern that vegetation growth is also limited by moisture availability, precipitation and soil moisture are also widely used to implement indirect TV (Yan *et al.* 2016b). However, the moisture availability mainly explains the interannual rather than seasonal variations of vegetation growth in TP (Zhang *et al.* 2016), so we did not use moisture indicators in the indirect TV.

Accuracy assessments of LAI reference maps *per se* are reported with large dynamic range. For example, the R^2 and RMSE of the reference maps were typically ranged within [0.42, 0.84] and [0.05, 0.60], respectively, depending on land covers (De Kauwe *et al.* 2011; Fang *et al.* 2019a; Heiskanen *et al.* 2012; Li *et al.* 2014; Zhu *et al.* 2014). Two validation activities, implemented by (Zhu *et al.* 2014) and (Li *et al.* 2014), for grasslands in China obtained R^2 /RMSE of 0.60/0.50 and 0.68/0.60, respectively. The accuracy of our reference maps ($R^2 = 0.72$, RMSE = 0.34) is obviously better than the above comparable studies. However, several sources of uncertainty still exist in our reference maps, including the sampling design and potential temporal variations in the transfer function. To assess if the generated sample is representative for the spatiotemporal variations of LAI in our study area, we compared the frequency distribution of LAI from ground measurements and reference maps (Figure 10). Results show that the sampling design can reproduce the overall shape of the frequency distribution histogram of the whole spatiotemporal variation. The overlapping area (OA) between the two histograms, a commonly used indicator to evaluate the representativeness of sampling design (Yin *et al.* 2017b), was 81.2%, i.e., the sample can preserve 81.2% of the whole spatiotemporal variations. Our transfer function was dependent on an empirical regression analysis between NDVI and LAI, and the fitting relationships between these variables may be temporally dependent (Tillack *et al.* 2014). We did not have sufficient

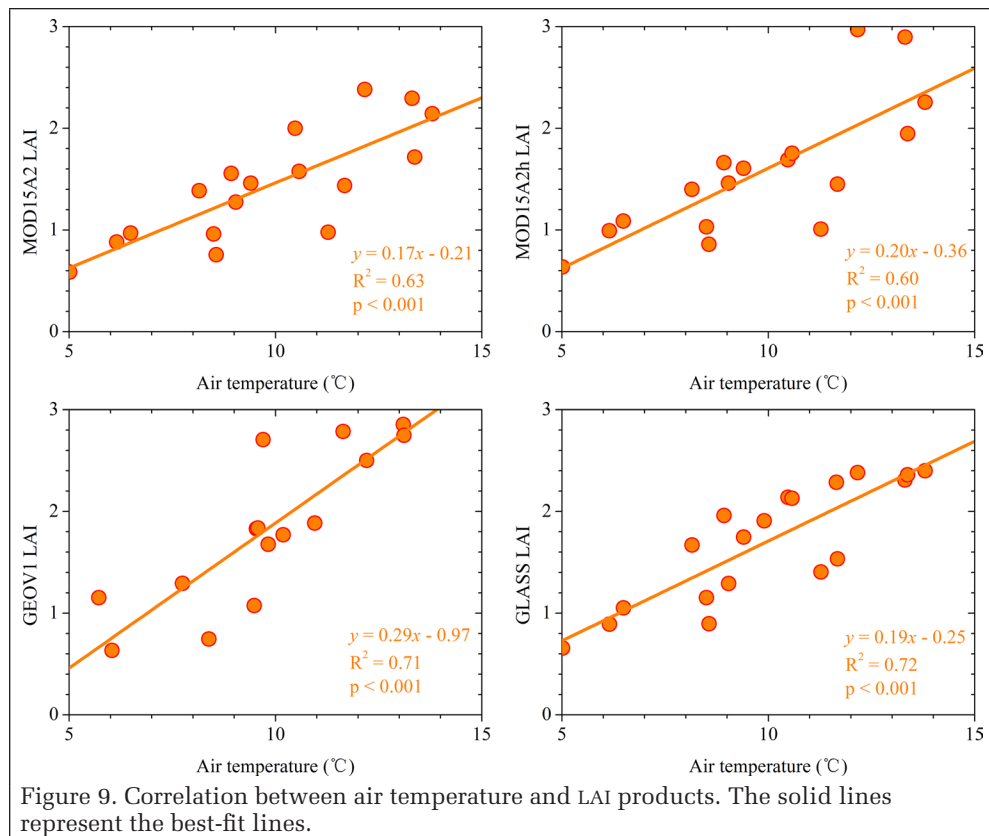


Figure 9. Correlation between air temperature and LAI products. The solid lines represent the best-fit lines.

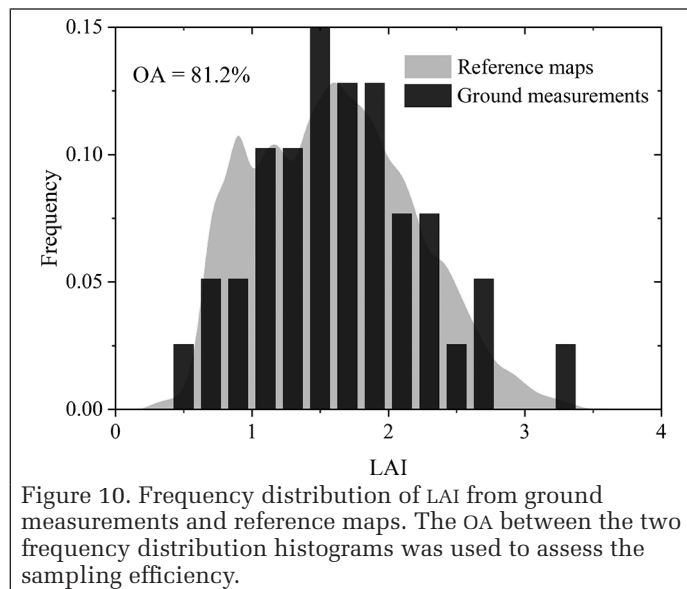


Figure 10. Frequency distribution of LAI from ground measurements and reference maps. The OA between the two frequency distribution histograms was used to assess the sampling efficiency.

field measurements to establish temporally specific transfer functions. However, the high correlation between LAI and temperature during the whole growing season demonstrates the quasi-stability of the transfer functions over time.

The definition of the LAI may also induce uncertainty. We collected field LAI measurements through destructive measurements, which correspond to the true LAI. Theoretically, MODIS LAI products also contain true LAI values (Myneni *et al.* 2002). However, the GLASS and GEOV1 products (Baret *et al.* 2013; Xiao *et al.* 2014), although they are both fused products that integrate MODIS and CYCLOPES, use different definitions of the LAI. Before fusion, GLASS use MODIS data and clumping-corrected CYCLOPES LAI products to obtain “best estimates” of the LAI (Xiao *et al.* 2014); therefore, it corresponds to true LAI values. On the other hand, to produce the GEOV1 product,

MODIS and CYCLOPES data are fused directly (Baret *et al.* 2013). Thus, this product represents a combination of true and effective LAI, because the MODIS and CYCLOPES LAI products correspond to true and effective LAI, respectively.

NDVI was used to calibrate the transfer function. Although it was widely reported that NDVI is sensitive to vegetation greenness and structure, it is also affected by other confounding factors, including atmospheric condition and soil background (Jiang *et al.* 2008). Many other vegetation indices were proposed to mitigate the influence of confounding factors. For example, the Enhanced Vegetation Index is insensitive to atmospheric conditions and saturation problems (Jiang *et al.* 2008), and the recently developed NIR reflectance of terrestrial vegetation is independent from the background influence and more correlated with the vegetation structure (Badgley *et al.* 2017). Therefore, these vegetation indices are also worth testing in the generation of LAI reference maps.

HJ-1A/1B imageries were adopted during the upscaling procedure because of their high resolution in both spatial (30 m) and temporal dimensions (see Figure 3). *Landsat* imageries are also characterized by decametric spatial resolution, yet their revisiting frequency is too low to capture the rapid vegetation dynamics (Zhu *et al.* 2019). *Sentinel-2* imageries currently provide an appropriate trade-off between spatial (10–60 m) and temporal resolutions (five days) (Lamquin *et al.* 2019). However, there was no *Sentinel-2* imagery available during our field campaign (the *Sentinel-2A* was launched in 2015).

Finally, this study focuses on evaluating the performance of four LAI products on capturing the temporal variation of LAI. The temporal variation of error was not explicitly analyzed, because of the spatial limitation of the study area. More validation activities are needed in our future study to give detailed temporal accuracy.

Implications for LAI Product Improvements

This study reveals that all four LAI products reproduced the vegetation dynamics, yet no one can reproduce the rapid change and the seasonal trend in LAI simultaneously. The MOD15A2 and MOD15A2h products successfully detected the grazing-induced sudden drop of LAI around DOY 205. In contrast, this drop was shifted and even undetectable in GEOV1 and GLASS LAI products, respectively. When it comes to the seasonal trend detection, the GEOV1 (R^2 between LAI temperature is 0.71) and GLASS ($R^2 = 0.72$) outperformed the MOD15A2 ($R^2 = 0.63$) and MOD15A2h products ($R^2 = 0.60$).

The direct TV results (Figure 7) implies that the capacity of LAI time series to detect the rapid change (e.g., grazing-caused drop on DOY 205) depends on the compositing method used in each product. The MODIS LAI products (including MOD15A2 and MOD15A2h) use a nonoverlapping compositing method, and the LAI value corresponding to the maximum FPAR during each eight-day compositing period is selected as the final retrieval result (Myneni *et al.* 2002). The relatively short compositing window makes them suitable for capturing rapid changes in LAI values. For the GEOV1 LAI product, although the nominal temporal interval is 10 days, there is a 10-day overlap to each side of the compositing period; i.e., the compositing window is 30-days (Baret *et al.* 2013). This overlapping compositing method leaves out subtle variations in the seasonal trajectory of LAI values, and the exact dates of the disturbances may also shift. Unlike all other LAI products, the GLASS LAI products used a special method to composite the LAI time series. The reprocessed MODIS reflectance data from an entire year are input into GRNNs to estimate the 1-year LAI profiles (Xiao *et al.* 2014). Although the nominal temporal interval is eight days, the temporal window used in processing is an entire year long. Therefore, there is significant loss in the high frequency information in a time series during the compositing procedure. Generally speaking, the compositing window should be short enough to detect the rapid changes

in LAI caused by anthropogenic activities (grazing in our study area) or extreme weather events. On the other hand, the compositing window should not be too short to avoid a “too noisy” temporal profile. For example, indirect TV revealed that the GEOV1 and GLASS LAI products have long compositing windows and this results in smooth LAI profiles, which are suitable for capturing meteorology-derived gradual changes (see Figure 9). Accordingly, the length of the compositing window should achieve an appropriate trade-off to detect both the rapid change and the seasonal trend.

Several methods can be used to improve the LAI time series. First, many gap-filling algorithms have been proposed based on temporal constraints (Fang *et al.* 2008; Verger *et al.* 2013). However, after gap-filling, the local details are missing because of the smoothing tendency of the interpolator. Therefore, it can improve the capacity of LAI products to capture long-term trend, but it reduces the advantages of remote sensing in real-time monitoring of vegetation. The second method to improve LAI time series involves the concurrent use of various sensors from different satellites (Flood *et al.* 2013; Mousivand *et al.* 2015). Currently, many sensors onboard different satellite platforms are taking land surface snapshots simultaneously. These sensors can build “virtual constellations” and provide more potential observations within a given time period, thus increasing the availability of data, especially for regions with a high probability of cloud coverage. Finally, some newly launched satellites can provide improved remote sensing observations and can be used to retrieve improved LAI time series. For example, China launched the *Gaofen (GF)-6* satellite, characterized by both high spatial and temporal resolutions.

Conclusions

This study implemented a systematical temporal validation, over grasslands in the northeastern TP, for four LAI products (MOD15A2, MOD15A2h, GEOV1, and GLASS) with both direct and indirect methods. The direct validation was implemented by comparing the LAI products with temporally continuous reference maps. These reference maps were generated by upscaling the field measurements with Chinese *HJ-1A/1B* CCD camera images as the bridge. Meanwhile, the indirect validation was conducted through a correlation analysis between the LAI product values with temporal profiles of temperature during the growing season.

Although all four LAI products reproduce the vegetation dynamics, no one can reproduce the rapid change and the seasonal trend in LAI simultaneously. The MOD15A2 and MOD15A2h products successfully detected the grazing-induced sudden drop of LAI around DOY 205. In contrast, this drop was shifted and even undetectable in GEOV1 and GLASS LAI products, respectively. As for the correlations of the four LAI products with air temperature (indirect validation), the MOD15A2 and MOD15A2h products have similar R^2 values (0.63 and 0.60, respectively), which are lower than those obtained from the GEOV1 (0.71) and GLASS (0.72) products. This study reveals that the compositing method determines the quality of the retrieved LAI time series to a large extent. The MOD15A2 and MOD15A2h products have short compositing windows (eight days), and they are suitable for detecting rapid changes in ecosystems, which are often caused by anthropogenic activities. On the other hand, GEOV1 and GLASS, with compositing windows of 30 days and 1 year, respectively, are more suitable for capturing gradual changes which are sensitive to climate change. In addition, this study found that a compositing window that is too short may result in a noisy or even discontinuous LAI temporal profile. Therefore, this research highlights the importance of the concurrent use of various sensors from different satellites and the introduction of the new generation of satellites (e.g., GF-6) for improving LAI time series.

Acknowledgments

This work was funded by the National Natural Science Foundation of China (41631180, 41571373), and the China Post-doctoral Science Foundation (2018T110996).

References

- Badgley, G., C. B. Field and J. A. Berry. 2017. Canopy near-infrared reflectance and terrestrial photosynthesis. *Science Advances* 3 (3):e1602244.
- Baret, F., P. Pacholczyk and R. Lacaze. 2012. *BioPar Product User Manual*.
- Baret, F., M. Weiss, R. Lacaze, F. Camacho, H. Makhmara, P. Pacholczyk and B. Smets. 2013. GEOV1: LAI and FPAR essential climate variables and FCOVER global time series capitalizing over existing products. Part1: Principles of development and production. *Remote Sensing of Environment* 137:299–309.
- Camacho, F., J. Cemicharo, R. Lacaze, F. Baret and M. Weiss. 2013. GEOV1: LAI, FPAR essential climate variables and FCOVER global time series capitalizing over existing products. Part 2: Validation and intercomparison with reference products. *Remote Sensing of Environment* 137:310–329.
- De Kauwe, M. G., M. I. Disney, T. Quaife, P. Lewis and M. Williams. 2011. An assessment of the MODIS collection 5 leaf area index product for a region of mixed coniferous forest. *Remote Sensing of Environment* 115 (2):767–780.
- Fang, H., Y. Zhang, S. Wei, W. Lia, Y. Ye, T. Sun and W. Liu. 2019a. Validation of global moderate resolution leaf area index (LAI) products over croplands in northeastern China. *Remote Sensing of Environment* 233.
- Fang, H. L., F. Baret, S. Plummer and G. Schaepman-Strub. 2019b. An overview of global leaf area index (LAI): Methods, products, validation, and applications. *Reviews of Geophysics* 57 (3):739–799.
- Fang, H. L., S. L. Liang, J. R. Townshend and R. E. Dickinson. 2008. Spatially and temporally continuous LAI data sets based on an integrated filtering method: Examples from North America. *Remote Sensing of Environment* 112 (1):75–93.
- Fang, H. L., S. S. Wei and S. L. Liang. 2012. Validation of MODIS and CYCLOPES LAI products using global field measurement data. *Remote Sensing of Environment* 119:43–54.
- Flood, N., T. Danaher, T. Gill and S. Gillingham. 2013. An operational scheme for deriving standardised surface reflectance from Landsat TM/ETM+ and SPOT HRG imagery for Eastern Australia. *Remote Sensing* 5 (1):83–109.
- Garrigues, S., R. Lacaze, F. Baret, J. T. Morisette, M. Weiss, J. E. Nickeson, R. Fernandes, S. Plummer, N. V. Shabanov, R. B. Myneni, Y. Knyazikhin and W. Yang. 2008. Validation and intercomparison of global Leaf Area Index products derived from remote sensing data. *Journal of Geophysical Research: Biogeosciences* 113 (G2):20.
- GCOS. 2011. *Systematic Observation Requirements for Satellite-Based Products for Climate, 2011 Update. Supplemental Details to the Satellite-Based Component of the Implementation Plan for the Global Observing System for Climate in Support of the UNFCCC (2010 Update)*.
- Hansen, M. C., P. V. Potapov1, R. Moore2, M. Hancher2, S. A. Turubanova1, A. Tyukavina1, D. Thau2, S. V. Stehman3, S. J. Goetz4, T. R. Loveland5, A. Kommareddy6, A. Egorov6, L. Chini1, C. O. Justice1, and J. R. G. Townshend1 . 2013. High-resolution global maps of 21st-century forest cover change. *Science* 342 (6160):850–853.
- Heiskanen, J., M. Rautiainen, P. Stenberg, M. Möttöus, V.-H. Vesanto, L. Korhonen, T. Majasalmi. 2012. Seasonal variation in MODIS LAI for a boreal forest area in Finland. *Remote Sensing of Environment* 126:104–115.
- Jiang, Z., A. Huete, K. Didan and T. Miura. 2008. Development of a two-band enhanced vegetation index without a blue band. *Remote Sensing of Environment* 112 (10):3833–3845.
- Jiapaer, G., S. L. Liang, Q. X. Yi and J. P. Liu. 2015. Vegetation dynamics and responses to recent climate change in Xinjiang using leaf area index as an indicator. *Ecological Indicators* 58:64–76.
- Knyazikhin, Y. 1999. MODIS leaf area index (LAI) and fraction of photosynthetically active radiation absorbed by vegetation (FPAR) product (MOD 15) algorithm theoretical basis document. <<http://eosps0.gsfc.nasa.gov/atbd/moddistabls.html>>.
- Lamquin, N., E. Woolliams, V. Bruniuel, F. Gascon, J. Gorroño, Y. Govaerts, V. Leroy, V. Lonjou, B. Alhammoud, J. A. Barsi, J. S. Czaplá-Myers, J. McCorkel, D. Helder, B. Lafrance, S. Clerc, and B. N.Holben. 2019. An inter-comparison exercise of Sentinel-2 radiometric validations assessed by independent expert groups. *Remote Sensing of Environment* 233.
- Li, A. N., J. H. Bian, G. B. Lei and C. Q. Huang. 2012. Estimating the maximal light use efficiency for different vegetation through the CASA model combined with time-series remote sensing data and ground measurements. *Remote Sensing* 4 (12):3857–3876.
- Li, F., D.L.B. Jupp, S. Reddy, L. Lyburner, N. Mueller, P. Tan and A. Islam. 2010. An evaluation of the use of atmospheric and BRDF correction to standardize Landsat data. *IEEE Journal of Selected Topics in Applied Earth Observations and Remote Sensing* 3 (3):257–270.
- Li, Z., H. Tang, X. Xin, B. Zhang and D. Wang. 2014. Assessment of the MODIS LAI product using ground measurement data and HJ-1A/1B imagery in the meadow steppe of Hulunber, China. *Remote Sensing* 6 (7):6242–6265.
- METI and NASA. 2019. *ASTER GDEM V3 User Guide*.
- Morisette, J. T., F. Baret, J. L. Privette, R. B. Myneni, J. E. Nickeson, S. Garrigues, N. V. Shabanov, M. Weiss, R. A. Fernandes, S. G. Leblanc, M. Kalacska, G. Arturo Sánchez-Azofeifa, M. Chubey, B. Rivard, P. Stenberg, M. Rautiainen, P. Voipio, T. Manninen, A. N. Pílant, T. E. Lewis, J. S. Iames, R. Colombo, M. Meroni, L. Busetto, W. B. Cohen, D. P. Turner, E. D. Warner, G. W. Petersen, G. Seufert and R. Cook. 2006. Validation of global moderate-resolution LAI products: A framework proposed within the CEOS land product validation subgroup. *IEEE Transactions on Geoscience and Remote Sensing* 44 (7):1804–1817.
- Mousivand, A., M. Menenti, B. Gorte and W. Verhoef. 2015. Multi-temporal, multi-sensor retrieval of terrestrial vegetation properties from spectral-directional radiometric data. *Remote Sensing of Environment* 158:311–330.
- Myneni, R. and Y. Park. 2015. *MODIS Collection 6 (C6) LAI/FPAR Product User's Guide*.
- Myneni, R. B., S. Hoffman, Y. Knyazikhin, J. L. Privette, J. Glassy, Y. Tian, Y. Wang, X. Song, Y. Zhang, G. R. Smith, A. Lotsch, M. Friedl, J. T. Morisette, P. Votava, R. R. Nemani, and S. W. Running. 2002. Global products of vegetation leaf area and fraction absorbed PAR from year one of MODIS data. *Remote Sensing of Environment* 83 (1–2): 214–231.
- Roy, D. P., M. A. Wulder, T. R. Loveland, cC. E. Woodcock, dR. G. Allen, eM. C. Anderson, fD. Helder, gl. R. Irons, hD. M. Johnson, iR. Kennedy, dT. A. Scambos, jC. B. Schaaf, kj. R. Schott, IY. Sheng, mE. F. Vermote, nA. S. Belward, oR. Bindschadler, pW. B. Cohen, qF. Gao, rJ. D. Hipple, sP. Hostert, tj. Huntington, uC. O. Justice, vA. Kilic, wV. Kovalskyy, aZ. P. Leek, L. Lyburner, xJ. G. Masek, yJ. McCorkel, yY. Shuai, zR. Trezza, ej. Vogelmann, cR. H. Wynnea, and aZ. Zhud . 2014. Landsat-8: Science and product vision for terrestrial global change research. *Remote Sensing of Environment* 145:154–172.
- Tillack, A., A. Clasen, B. Kleinschmit and M. Foerster. 2014. Estimation of the seasonal leaf area index in an alluvial forest using high-resolution satellite-based vegetation indices. *Remote Sensing of Environment* 141:52–63.
- Verger, A., F. Baret, M. Weiss, S. Kandasamy and E. Vermote. 2013. The CACAO method for smoothing, gap filling, and characterizing seasonal anomalies in satellite time series. *IEEE Transactions on Geoscience and Remote Sensing* 51 (4):1963–1972.

- Wen, J., Q. Liu, Y. Tang, B. Dou, D. You, Q. Xiao, Q. Liu and X. Li. 2015. Modeling land surface reflectance coupled BRDF for HJ-1/CCD data of rugged terrain in Heihe River Basin, China. *IEEE Journal of Selected Topics in Applied Earth Observations and Remote Sensing* 8 (4):1506–1518.
- Xiao, Z. 2014. GLASS global leaf area index product: Algorithm theoretical basis document.
- Xiao, Z. Q., S. Liang, J. Wang, P. Chen, X. Yin, L. Zhang and J. Song. 2014. Use of general regression neural networks for generating the GLASS leaf area index product from time-series MODIS surface reflectance. *IEEE Transactions on Geoscience and Remote Sensing* 52 (1):209–223.
- Xie, X. Y., A. Li, H. Jin, J. Tan, C. Wang, G. Lei, Z. Zhang, J. Bian and X. Nan. 2019. Assessment of five satellite-derived LAI datasets for GPP estimations through ecosystem models. *Science of the Total Environment* 690:1120–1130.
- Yan, K., T.aejin Park 2,* , G.uangjian Yan, 1OrcID,C.hi Chen, 2OrcID,B.in Yang 2, 3,Z.hao Liu, 2,R.amakrishna R. Nemani 4, Y.uri Knyazikhin 2 and R.anga B. Myneni 2 . 2016a. Evaluation of MODIS LAI/FPAR product collection 6. Part 1: Consistency and improvements. *Remote Sensing* 8 (5).
- Yan, K., T. Park, G. Yan, Z. Liu, B. Yang, C. Chen, R. R. Nemani, Y. Knyazikhin and R. B. Myneni. 2016b. Evaluation of MODIS LAI/FPAR product collection 6. Part 2: Validation and intercomparison. *Remote Sensing* 8 (6).
- Yin, G. F., A. Li, H. Jin, W. Zhao, J. Bian, Y. Qu, Y. Zeng and B. Xu. 2017a. Derivation of temporally continuous LAI reference maps through combining the LAINet observation system with CACAO. *Agricultural and Forest Meteorology* 233:209–221.
- Yin, G. F., A. N. Li and A. Verger. 2017b. Spatiotemporally representative and cost-efficient sampling design for validation activities in Wanglang experimental site. *Remote Sensing* 9 (12).
- Yin, G. F., J. Li, Q. Liu, L. Li, Y. Zeng, B. Xu, L. Yang and J. Zhao. 2015. Improving leaf area index retrieval over heterogeneous surface by integrating textural and contextual information: A case study in the Heihe River Basin. *IEEE Geoscience and Remote Sensing Letters* 12 (2):359–363.
- Zhang, Y., C. Zhang, Z. Wang, Y. Chen, C. Gang, R. An and J. Li. 2016. Vegetation dynamics and its driving forces from climate change and human activities in the Three-River source region, China from 1982 to 2012. *The Science of the Total Environment* 563–564:210–20.
- Zhu, L., J. M. Chen, S. H. Tang, G. C. Li and Z. D. Guo. 2014. Inter-comparison and validation of the FY-3A/MERSI LAI product over mainland China. *IEEE Journal of Selected Topics in Applied Earth Observations and Remote Sensing* 7 (2):458–468.
- Zhu, Z., M. A. Wulder, D. P. Roy, C. E. Woodcock, M. C. Hansen, V. C. Radeloff, S. P. Healey, C. Schaaf, P. Hostert, P. Strobl, J.-F. Pekel, L. Lyburner, N. Pahlevan and T. A. Scambos. 2019. Benefits of the free and open Landsat data policy. *Remote Sensing of Environment* 224:382–385.

WHO'S WHO IN ASPRS

BOARD OF DIRECTORS

BOARD OFFICERS

President

Thomas Jordan, Ph.D.
University of Georgia

President-Elect

Jeff Lovin
Woolpert

Vice President

Jason M. Stoker, Ph.D.
U.S. Geological Survey

Past President

Anne Hillyer, CP
Bonneville Power Administration (USDOE)

Treasurer

Stewart Walker, Ph.D.

Secretary

Roberta E. Lenczowski

BOARD MEMBERS

Sustaining Members Council – 2019

Chair: Joe Cantz
Vice Chair: TBA
www.asprs.org/About-Us/Sustaining-Members-Council.html

Early-Career Professionals Council – 2020

Chair: Peng Fu
Vice Chair: TBA

Region Officers Council – 2021

Chair: Lorraine B. Amenda, PLS, CP
Vice Chair: Demetrio Zourarakas

Student Advisory Council – 2020

Chair: Victoria Scholl
Vice Chair: TBA
<http://www.asprs.org/Students/Student-Advisory-Council.html>

Technical Division Directors Council – 2020

Chair: John McCombs
Vice Chair: Bandana Kar, Ph.D.

TECHNICAL DIVISION OFFICERS

Geographic Information Systems Division – 2021

Director: Xan Fredericks
Assistant Director: Denise G. Theunissen
www.asprs.org/Divisions/GIS-Division.html

Lidar Division – 2020

Director: Amar K. Nayegandhi, CP, CMS
Assistant Director: Joshua Nimetz, CMS
www.asprs.org/Divisions/Lidar-Division.html

Photogrammetric Applications Division – 2020

Director: Paul C. Bresnahan
Assistant Director: Kurt Rogers
www.asprs.org/Divisions/Photogrammetric-Applications-Division.html

Primary Data Acquisition Division – 2021

Director: Jon Christopherson
Assistant Director: J. Chris Ogier
www.asprs.org/Divisions/Primary-Data-Aquisition-Division.html

Professional Practice Division – 2022

Director: Harold W. Rempel, III, CP
Assistant Director: TBA
www.asprs.org/Divisions/Professional-Practice-Division.html

Remote Sensing Applications Division – 2020

Director: David W. Kreighbaum
Assistant Director: Raechel A. White, Ph.D.
www.asprs.org/Divisions/Remote-Sensing-Applications-Division.html

Unmanned Autonomous Systems (UAS) – 2020

Director: Benjamin Vander Jagt, Ph.D.
Assistant Director: Megan Miller, Ph.D.

REGION PRESIDENTS

Alaska Region

David Parret
<http://www.asprsalaska.org/>

Cascadia Region

TBA
<http://columbia.asprs.org/CRR/>

Central New York Region

John Boland, C.P.
<http://www.esf.edu/asprs/>

Eastern Great Lakes Region

Edward Kunz, GISP
<http://egl.asprs.org/>

Florida Region

Erin McCormick
<http://florida.asprs.org/>

Heartland Region

Paul Manley
<http://heartland.asprs.org/>

Intermountain Region

TBA
<http://asprsintermountain.weebly.com/>

Mid-South Region

Dr. David Hughes
<https://www.asprs.org/all-regions/mid-south.html>

New England Region

TBA
<http://neweng.asprs.org/>

North Atlantic Region

Richard W. Carlson, Jr., P.L.S., C.P.
<http://natlantic.asprs.org/>

Pacific Southwest Region

Riadh Munjy, Ph.D.
<https://pswasprs.org/>

Potomac Region

Jackie Carr
<http://www.asprspotomac.org/>

Rocky Mountain Region

Jeffrey M. Young
<http://www.asprs-rmr.org/>

Western Great Lakes Region

Kirk Contrucci, CP
<http://wgl.asprs.org/>

Building Extraction from High-Resolution Remote Sensing Images Based on GrabCut with Automatic Selection of Foreground and Background Samples

Ka Zhang, Hui Chen, Wen Xiao, Yehua Sheng, Dong Su, and Pengbo Wang

Abstract

This article proposes a new building extraction method from high-resolution remote sensing images, based on GrabCut, which can automatically select foreground and background samples under the constraints of building elevation contour lines. First the image is rotated according to the direction of pixel displacement calculated by the rational function Model. Second, the Canny operator, combined with morphology and the Hough transform, is used to extract the building's elevation contour lines. Third, seed points and interesting points of the building are selected under the constraint of the contour line and the geodesic distance. Then foreground and background samples are obtained according to these points. Fourth, GrabCut and geometric features are used to carry out image segmentation and extract buildings. Finally, WorldView satellite images are used to verify the proposed method. Experimental results show that the average accuracy can reach 86.34%, which is 15.12% higher than other building extraction methods.

Introduction

Buildings, as an important component of the living environment, have been the focus of numerous studies, including in urban planning and construction, change detection, population-density estimation, and disaster assessment. Automatic and efficient extraction of geometric and spatial information of buildings has always been an important research topic in the field of geoinformation science (X. Huang *et al.* 2017). With the advance of remote sensing technology, spatial resolutions of images from very-high-resolution satellites (e.g., SPOT-5, WorldView-1 through WorldView-4, and QuickBird) have reached meter level, providing more detailed spatial and

Ka Zhang is with the Key Laboratory of Virtual Geographic Environment, Nanjing Normal University, Ministry of Education, Nanjing, China; the School of Geography, Nanjing Normal University, Nanjing, China; the Jiangsu Center for Collaborative Innovation in Geographical Information Resource Development and Application, China; the State Key Laboratory Cultivation Base of Geographical Environment Evolution (Jiangsu Province), China; and the Key Laboratory of Urban Land Resources Monitoring and Simulation, MNR, China (zhangka81@126.com).

Hui Chen (co-first author), Yehua Sheng (co-first author), Dong Su, and Pengbo Wang are with the Key Laboratory of Virtual Geographic Environment, Nanjing Normal University, Ministry of Education, Nanjing, China; and the School of Geography, Nanjing Normal University, Nanjing, China.

Wen Xiao (co-first author) is with the School of Engineering, Newcastle University, Newcastle upon Tyne, United Kingdom.

textural information (Cheng and Han 2016). Therefore, extraction of building information from high-resolution remote sensing images has become a research hot spot (Cao *et al.* 2016).

However, accurate building extraction from high-resolution images remains a challenge due to various factors in remote sensing images, such as diversity of objects, complexity of buildings, noise, occlusions, shadows, and low contrast. To make it worse, when the viewing perspective is oblique there will be much coverage of building elevations in remote sensing images. Using monocular optical images to automatically extract the top contour of buildings, those elevation areas are hard to distinguish from building tops (Cui, Yan and Reinartz 2012; J. Wang *et al.* 2015)—but the main goal of building extraction is to have a clean boundary for each building (J. Wang *et al.* 2015).

At present, methods based on shadow and auxiliary information are frequently used. However, in locating a building, shadow-based methods treat the elevation and the roof equally, producing inaccurate boundaries (Ok, Senaras and Yuksel 2013; Ngo, Collet and Mazet 2015; Gao *et al.* 2018). Other methods based on auxiliary data such as lidar (light detection and ranging) can distinguish the roof and elevation well, but the cost of obtaining such data is high (Zarea and Mohammadzadeh 2016; Fernandes and Dal Poz 2017; S. Kim and Rhee 2018). Apart from those, deep learning-based image object extraction is a new research trend, but this kind of method needs large amounts of training data, and usually do not use such data containing a large quantity of elevations of buildings (J. Huang *et al.* 2019; Wurm *et al.* 2019).

This article proposes a building extraction method that can distinguish the roof from the elevation under the constraint of the building's elevation contours without any other types of data or training data. First, building elevation contour lines are extracted. Then the foreground samples are selected under the constraints of elevation contours, which are used as background samples. Finally, GrabCut is used for image segmentation, and geometric features of the segmented area are used to accurately extract buildings from high-resolution images. The method is tested on two urban data sets (Guangdong, China, and Tripoli, Libya) using WorldView-2 and WorldView-3 satellite image configurations. All results are evaluated qualitatively and quantitatively compared with ground truths. The results show that building tops can be accurately distinguished from the elevations of buildings in the monocular images of highly oblique viewing angles with a high level of automation.

Photogrammetric Engineering & Remote Sensing
Vol. 86, No. 4, April 2020, pp. 235–245.
0099-1112/20/235–245

© 2020 American Society for Photogrammetry
and Remote Sensing
doi: 10.14358/PERS.86.4.235

Related Work

Recent methods of extracting buildings from high-resolution remote sensing images can be divided into four categories: based on (a) edge and corner detection (Cui *et al.* 2012; Cote and Saeedi 2013; Manno-Kovacs and Sziranyi 2015); (b) auxiliary information such as shadows (Ok *et al.* 2013; Ngo *et al.* 2015; Gao *et al.* 2018); (c) fusion of multisource data such as lidar, synthetic aperture radar, and DSMs (digital surface models), and so on (Zarea and Mohammadzadeh 2016; Fernandes and Dal Poz 2017; S. Kim and Rhee 2018); and (d) deep learning classification (Y. Liu *et al.* 2018; J. Huang *et al.* 2019; Wurm *et al.* 2019).

Methods of the first category generally adopt some edge-detection operators to process the image first, and then combine features of spectrum, texture, corner, or spatial information to optimize the contours (Cui *et al.* 2012; Cote and Saeedi 2013; J. Wang *et al.* 2015). J. Wang *et al.* (2015) used a line-segment detector called EDLines to extract building lines, and then perceptual grouping was applied to reorganize the relationship of detected line segments and to gain complete contours of buildings. Cote and Saeedi (2013) developed an automatic system for detecting rooftops using line segments and corners. Although these methods can effectively utilize the underlying features of the image, they are mostly prone to false detections caused by shadows, roads, noise, and others, resulting in inaccurate building boundaries. The final extraction results depend on the effect of edge and corner detection.

Methods based on auxiliary information, such as building shadows, can help determine the locations of buildings and select samples for an image-segmentation algorithm through the spatial relationship between building and shadow. Gao *et al.* (2018) used a shifted shadow algorithm to select samples of buildings, and then buildings were extracted using a support vector machine. Ngo *et al.* (2015) proposed an original region-level Markov random-field image-segmentation method, and buildings were extracted based on the segment rectangularity and location with respect to shadows. Although this type of method can automatically locate building areas to a certain extent and improve the level of automation, it is difficult to distinguish a building from the surrounding background when the foreground and background have similar spectral properties.

Another type of method is to extract buildings by fusing the height and spectrum information of image pixels. Fernandes and Dal Poz (2017) obtained a normalized nDSM from an airborne laser-scanning point cloud and projected onto the image, then used the height information from the DSM to delimit regions (subimages) to be segmented in the image. Then a Markov random-field probabilistic approach was used to extract building roof contours. Zarea and Mohammadzadeh (2016) extracted off-terrain objects including trees and buildings, then a number of features were produced as inputs of support vector machines to separate buildings from trees. These methods use elevation information from auxiliary data (e.g., DSM, synthetic aperture radar) as constraints, obtaining promising results, but the cost of using multiple data is high, and the extraction accuracy is easily affected by the quality of data fusion (Zarea and Mohammadzadeh 2016; Fernandes and Dal Poz 2017; S. Kim and Rhee 2018).

Recent studies have demonstrated that deep convolutional neural networks can achieve impressive performance on remote sensing image processing, such as scene classification and object detection (J. Huang *et al.* 2019). Thus many building extraction methods based on deep learning have been proposed (Wurm *et al.* 2019). J. Huang *et al.* (2019) used a gated residual refinement network to extract buildings from high-resolution aerial images and lidar data. Y. Liu *et al.* (2018) established a multilevel building detection model using convolutional neural networks to extract buildings from remote sensing images. Although this kind of method

can obviously improve extraction accuracy, it needs a large number of samples and long running time, and can still result in incomplete boundaries (Wurm *et al.* 2019).

These four categories of methods mainly aim at building extraction in the case of using true orthophotos or ones with a negligible view of building elevations. When the oblique viewing angle is large in high-resolution images, they tend to suffer (El-naggar 2018). In fact, many studies have achieved promising results in complex image segmentation by using the graph-cut optimization framework (Li *et al.* 2018; Ullah *et al.* 2018). The basic idea is to use the graph-cut correlation theory to separate regions of interest from images after the initial foreground samples are obtained manually or by introducing other auxiliary information (S. Liu *et al.* 2015; Zheng *et al.* 2018; Reza *et al.* 2019). S. Liu *et al.* (2015) automatically calculated the threshold value of each image, and used the graph-cut algorithm to perform prebackground segmentation after the initial sample was selected. Privalov and Kazantsev (2018) proposed a new method based on graph cuts which proposes a hybrid algorithm with efficient parallel implementation on a general-purpose graphics processing unit. However, in complex geographic scenes, the results of these methods are not ideal.

Thus, in light of limitations of all of these methods in building extraction from high-resolution and oblique-viewing remote sensing images, this article proposes a building extraction method based on GrabCut with automatic selection of foreground and background samples.

Method

The proposed method consists of four steps (Figure 1). The first step is to use the rational function model to calculate the direction of building image displacement, and then rotate the remote sensing image. In the next step, an algorithm based on the Canny operator and morphology is proposed to extract building elevation contour lines from the rotated images. The third step is to select foreground and background samples with constraints of building elevation contour lines. In the

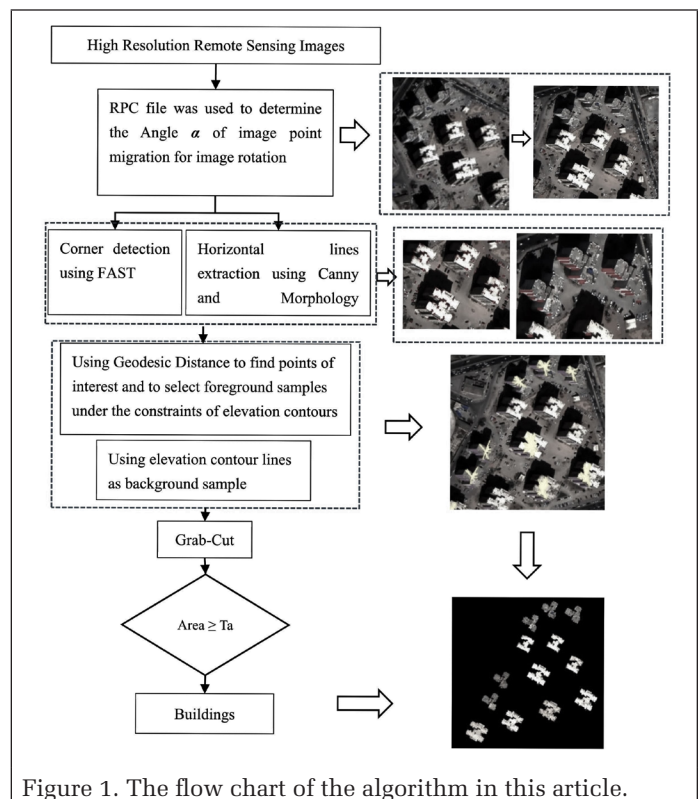


Figure 1. The flow chart of the algorithm in this article.

last step, the GrabCut algorithm is applied to image segmentation using the samples, and then buildings are extracted from the segmentation results according to simple geometric rules.

Image Rotation

In order to make it easier to extract the elevation contour line of the building, the image is rotated according to the angle of image-point displacement. In this way, the line can be extracted using a rectangular morphological structure element. In this part, the rational function model is used to determine the angle of image rotation. The rational function model is a general geometric imaging model for charge-coupled device satellite images which is independent from the sensor (Grodecki and Dial 2003):

$$\begin{cases} r = \frac{P_1(X, Y, Z)}{P_2(X, Y, Z)} \\ c = \frac{P_3(X, Y, Z)}{P_4(X, Y, Z)} \end{cases} \quad (1)$$

Most satellite systems will provide an RPC file (rational polynomial coefficients or rapid positioning capability) containing various parameters in the model. Rational function models can be divided into a positive-solution model and a negative-solution model. Equation 1 represents the transformation from object to image, which is a positive-solution model. In contrast, the general inverse solution model is as follows:

$$\begin{cases} X = \frac{P_5(r, c, Z)}{P_6(r, c, Z)} \\ Y = \frac{P_7(r, c, Z)}{P_8(r, c, Z)} \end{cases} \quad (2)$$

where (r, c) and (X, Y, Z) are the image-space coordinates of the normalized image points and their corresponding object-space coordinates, and P_1 through P_8 are rational polynomial functions (Moghaddam, Mokhtarzade and Moghaddam 2018).

In this article, the process of calculating the displacement angle of image points by the RPC model is as follows: First we take a random point (r_0, c_0, Z_0) , where Z_0 is the average elevation of the area. Based on Equation 2, a virtual object point (X_0, Y_0, Z_0) can be obtained after transformation. Then P points near Z_0 are taken at an interval of 10 m, and the corresponding P image points are obtained by Equation 1. The value of P can be between 5 and 10.

According to the theory of the epipolar line (T. Kim 2000; Morgan *et al.* 2006), the epipolar line of a remote sensing image can be regarded as a straight line in a small range (M. Wang *et al.* 2011; Jannati, Zoj and Mokhtarzade 2018). Moreover, the WorldView images have good parallel characteristics, meaning their epipolar lines are almost parallel. Therefore, these image points can be fitted with a straight line, and the displacement direction of the image point is the direction angle α of the straight line:

$$\alpha = \tan^{-1}k, \quad (3)$$

where k is the slope of the fitting line. The original image is noted as I and the rotated image is I_{rot} , as shown in Figure 2.

Building Elevation Contour-Line Extraction Based on Canny and Morphology Operators

In order to obtain the elevation contour line in an image, we first use bilateral filtering to denoise the image I_{rot} and then the Canny edge detector (Xu, Baojie and Guoxin 2017) to

get a binary image I_1 that contains building contours. Next, the binary image is filled with small voids by a morphological closing operation, and then a rectangular morphological structure element of a certain length is constructed to extract the horizontal lines by a morphological opening operation. Morphology is used to analyze or extract image features corresponding to structural elements in images, so the shape and size of the structural element will directly affect the results of image analysis. Because the contours of buildings are horizontal after rotation, structural elements with a width of 1 pixel and a length of L_m are used in this experiment. The value of L_m depends on the size of displacement of the building in images. Generally, the more the image points are displaced, the larger the value of L_m is. Finally, the Hough transform, for which the angle threshold is set to 90° , is used to detect the horizontal building contours in the image. Those horizontal contours are the building elevation contour lines as shown in red in Figure 3.

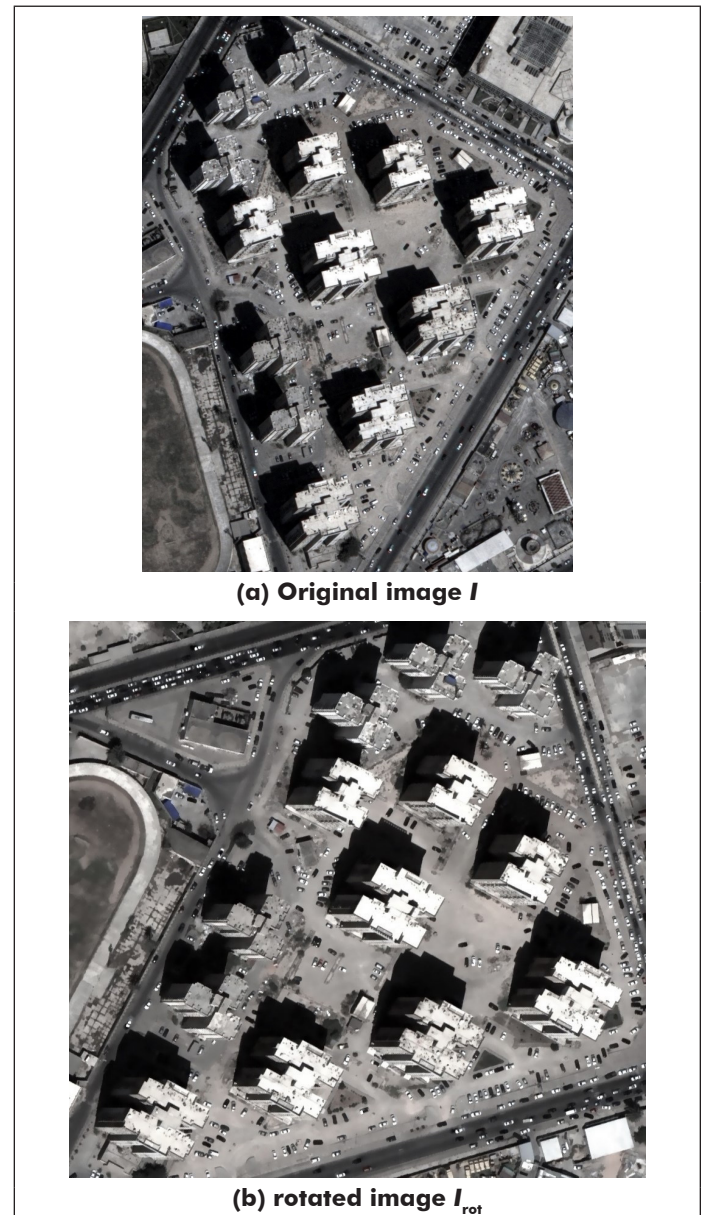


Figure 2. Image rotation using displacement direction angle α .

Foreground and Background Sample Determination with Constraints of Building Elevation Contour Lines

High-resolution remote sensing images without orthorectification may contain large areas of building elevations, which are difficult to distinguish from the tops of buildings because their texture and spectral characteristics are very similar. This phenomenon will be more obvious with improved spatial resolution in sensing images. However, these elevations are also effective features to distinguish buildings from other ground objects. In this article, after the elevation contour lines are extracted, a foreground sample is selected under the constraint of the elevation contour lines, and the elevation contour lines are taken as the background. Finally, the top of the building is extracted using GrabCut.

FAST Corner Detection

FAST is a corner-detection algorithm for optical images proposed by Rachmawati, Supriana, and Khodra (2017). It shows good performance in corner extraction and computational efficiency. The main principle of FAST is shown in Figure 4. To detect if a pixel is a corner point, it is taken as the center of a circle whose radius is 3 pixels. If there are nine or more consecutive pixels of the 16 on the circle that are not similar to the center pixel, the center pixel is judged to be a corner point. The result of FAST corner detection on a remote sensing image is shown in Figure 5, in which corner points are in red and horizontal lines are in green.

Horizontal-Line Adjustment Using Corners and Geometric Rules

In order to select the foreground samples more accurately under the constraint of the building elevation contour lines, the length of the contours must be accurate. Therefore, the detected horizontal lines are refined according to geometric shape rules and adjusted under corner constraints. Suppose that the left and right endpoint coordinates of a horizontal line are (l_x^l, y) , (l_x^r, y) . The merging rules of horizontal lines (Figure 6) are as follows:

1. The horizontal and vertical distances of two lines are below certain thresholds: $l_{2x}^r - l_{1x}^l \leq t_1$, $y_1 - y_2 \leq t_2$.
2. Both ends of a horizontal line exceed those of a neighboring line: $l_{1x}^l \leq l_{2x}^l$, $l_{1x}^r \geq l_{2x}^r$, $y_1 - y_2 \leq t_2$.



Figure 3. Horizontal lines obtained by morphology and Canny operators.

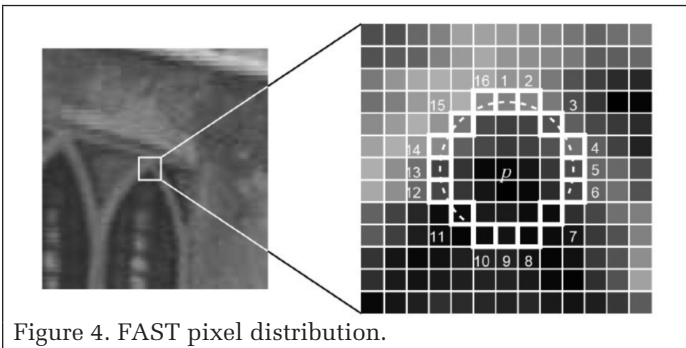


Figure 4. FAST pixel distribution.

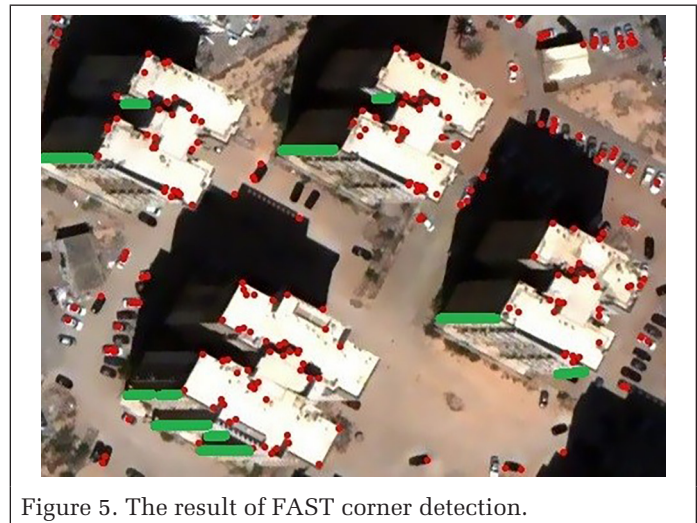
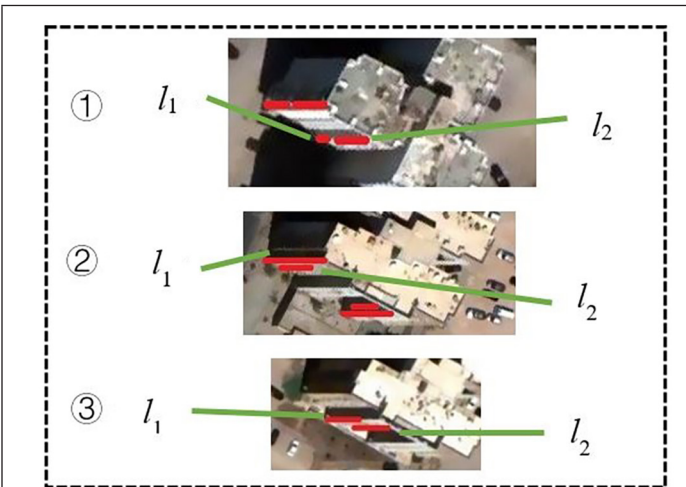
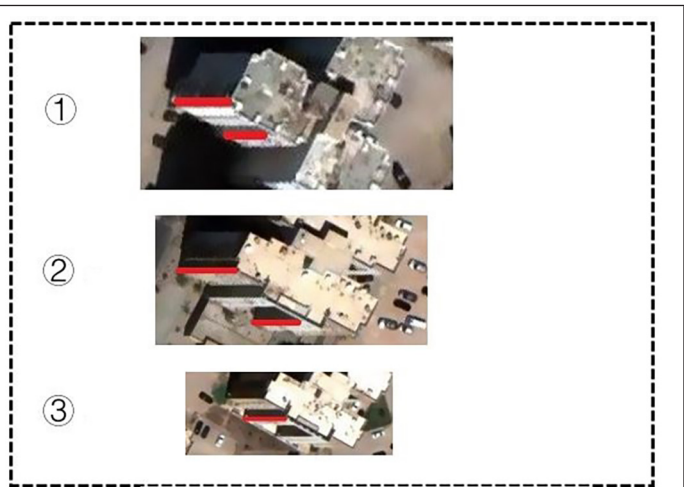


Figure 5. The result of FAST corner detection.



(a) Before the merge



(b) After the merge

Figure 6. Contour-line merge.

3. The distance between the right end of one line and the left end of the other line is below a certain threshold: $I_{1x}^1 - I_{2x}^1 \leq t_1$, $y_1 - y_2 \leq t_2$. In these rules, t_1 and t_2 are the distance thresholds of the linear coordinates x and y , and the values of t_1 and t_2 can be set between 5 and 10 pixels.

After the horizontal contour lines are merged, the detected corners are used to further refine their lengths. First, a small window of $D_s \times D_s$ pixels is used to find the nearest corner from the endpoint. (If the satellite's view perspective is on the right side of the area, the corners of the tops of buildings are on the left of the endpoints.) The size of D_s can be between 5 and 9 pixels. The displacement of buildings with different satellite viewing directions is shown in Figure 7. The green lines in Figure 8a are the initial result of the contour-line extraction, and the green lines in Figure 8b are the adjusted extraction result. The red points are the detected corner points. The length of the contour line can be corrected by extending or shrinking it to the nearest corner points at either end, depending on whether it is shorter or longer than the contour length. See Figure 8 for the results of line adjustment.

Horizontal-Line Grouping and Initial Seed-Point Setting

False detections of contour lines can be observed on objects that resemble buildings. In order to eliminate the false detections, all lines are grouped as follows. First, let the set of all horizontal lines be L_{all} . Given a certain distance interval D , L_{all} is divided into several subsets of t horizontal lines (L_1, L_2, \dots, L_t). The size of the threshold D is related to the algorithm running time and the number of samples selected. Generally speaking, the denser the building, the smaller the value of D ; and the more samples selected, the longer the algorithm running time. Normally, there will be at least two contour lines of a building elevation, and thus if the number of horizontal lines in L_i is 1, it can be considered a false detection. In Figure 9, the correct contour lines are highlighted in green rectangles and the incorrect contour line in a red rectangle.

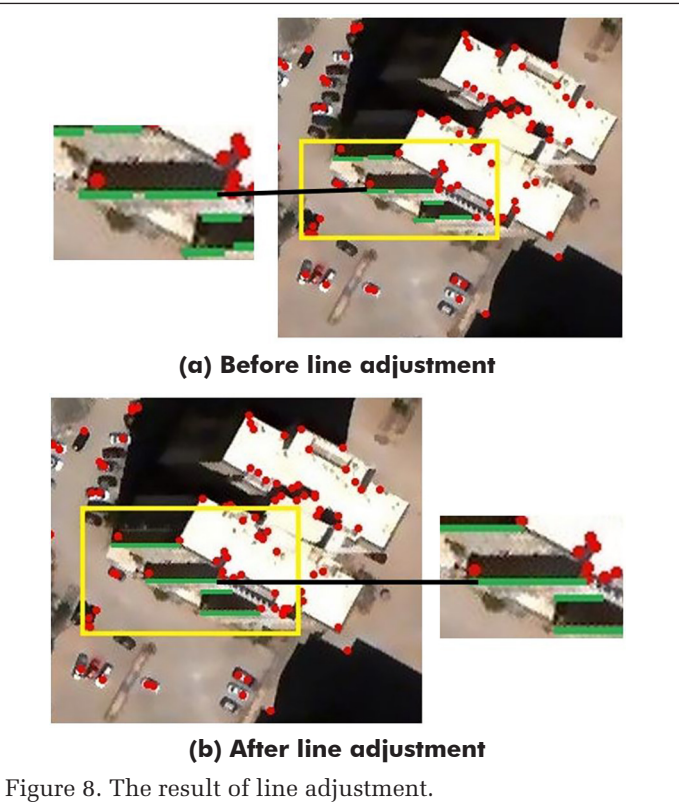
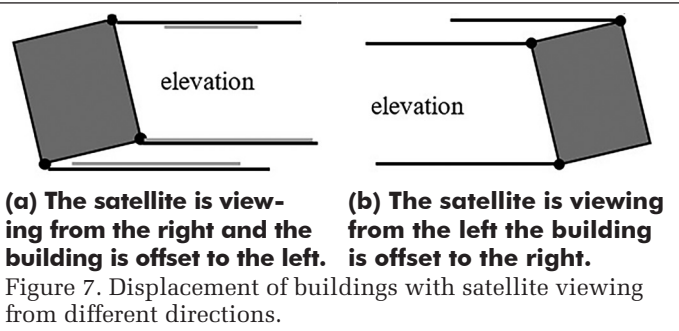
After elimination, the final number of subsets is denoted m , and each subset determines a seed point. Then the average value (x^{ai}, x^{aj}) of the line coordinates (x, y) is calculated near the top contour of the building in each set. In order to prevent the coordinates of the initial seed points from sitting on the edge line of the building contour, an offset τ is necessary. If the coordinates of the initial seed point C_i are (C_{xi}, C_{yi}) , then they are changed to $(C_{xi} + \tau, C_{yi})$. The values of τ are in the range of 10 to 20 pixels. The coordinates of P points that were used to calculate the displacement angle of the image are used to decide whether τ is positive or negative. If the x coordinate of the point in P is positively correlated with the virtual elevation Z , the roof is to the right of the elevation contour lines and τ is positive. The initial seed points are shown in green in Figure 10.

Sample Selection Based on the Geodesic Distance

The geodesic distance is a standard proposed by Gulshan *et al.* (2010) to measure the difference between image points by combining with gradient and spectral information. The specific calculation form is shown in Equations 4 and 5:

$$L(\Gamma) = \sum_{i=1}^{n-1} \sqrt{(1 - \gamma_g) d(\Gamma^i, \Gamma^{i+1})^2 + \gamma_g \nabla I(\Gamma^i)^2}, \quad (4)$$

where Γ is an arbitrary parametrized discrete path with n pixels given by $\{\Gamma^1, \Gamma^2, \dots, \Gamma^n\}$, $d(\Gamma^i, \Gamma^{i+1})$ is the Euclidean distance between successive pixels, and the quantity $\|\nabla I(\Gamma^i)\|^2$ is a finite difference approximation of the image gradient between the points (Γ^i, Γ^{i+1}) . The gradient image here is obtained using the Sobel operator. The parameter γ_g weights the Euclidean distance with the geodesic length. Using the above definition, the geodesic distance can be defined as



$$d_g(a,b) = \min_{\Gamma \in P_{a,b}} L(\Gamma) \quad \Gamma_{a,b} = \arg \min_{\Gamma \in P_{a,b}} L(\Gamma), \quad (5)$$

where $P_{a,b}$ denotes the set of all discrete paths between two grid points a and b . Here we use the geodesic distance as a measure of the point of interest and the seed point. First of all, the initial seed point is determined and the search window size set as $T_{se} \times T_{se}$ pixels. Then the corner point satisfying $d_g(a,b) \leq T_{geo}$ is the required point of interest, and all the pixel points between this point and the seed point are taken as foreground samples.

In order to distinguish the building elevation from the roof, the extracted elevation contour lines are taken as the background samples. In Figure 11, the purple lines are background samples and the yellow lines are foreground samples.

Image Segmentation Based on GrabCut

The basic idea of GrabCut (Li *et al.* 2018) is to map the entire image to the s - t network diagram, as shown in Figure 12, in which the source point s represents the foreground endpoint and the confluence point t represents the background endpoint. To build a GrabCut network, foreground and background samples are required to establish a Gaussian mixture model, which is initiated using the k -means algorithm, and then the distances between nodes and foreground or background and the distances between adjacent nodes are calculated. Then the energy weight of segmentation is obtained, and the s - t network graph is constructed for unknown regions. Finally, the max-flow-min segmentation algorithm is used to segment the unknown regions. The process of GrabCut segmentation updates and modifies the parameters of the Gaussian mixture model iteratively to ensure convergence. After the image is segmented by these procedures, the buildings can be extracted by screening the sizes of the extracted patches.

Experiment and Results

Data and Evaluation Methods

Data Sets

Five WorldView satellite images are tested, as shown in Table 1 and Figure 13. In the five images, building tops are clear but building elevations or other ground objects have similar spectrum features, which leads to the difficulty in separating top contours from elevation contours and from the ground. All the images are shown after fusion of multispectral and panchromatic bands.

Evaluation Method

The precision, recall, and F_1 scores were used to quantitatively evaluate the building extraction results:

$$\text{Precision} = \frac{TP}{TP + FP} \times 100\% \quad (6)$$

$$\text{Recall} = \frac{TP}{TP + FN} \times 100\% \quad (7)$$

$$F_1 = \frac{2 \times \text{Precision} \times \text{Recall}}{\text{Precision} + \text{Recall}} \times 100\%, \quad (8)$$

where TP (true positive) indicates the number of buildings extracted by the algorithm compared to the manually labeled ground truth; FP (false positive) indicates the number of objects falsely detected as buildings; and FN (false negative) denotes the number of buildings that are labeled in the ground truth but not detected by the algorithm.

Experimental Results and Analysis

The proposed method is implemented using Visual C# .NET 2013 programming language and Emgu CV function library in a Windows 10 environment.

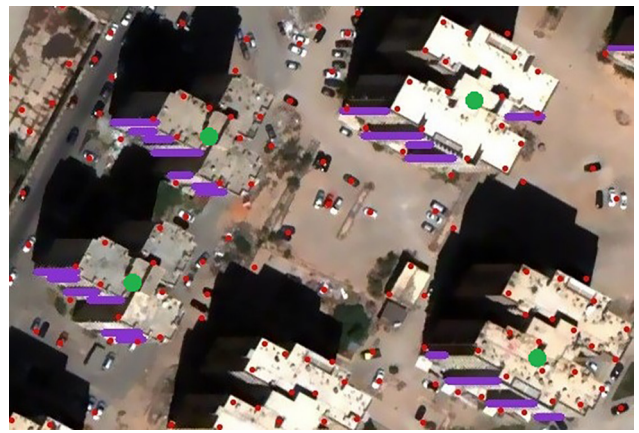


Figure 10. Examples of initial seed points in green.



Figure 11. Foreground sample (yellow) and background sample (red).

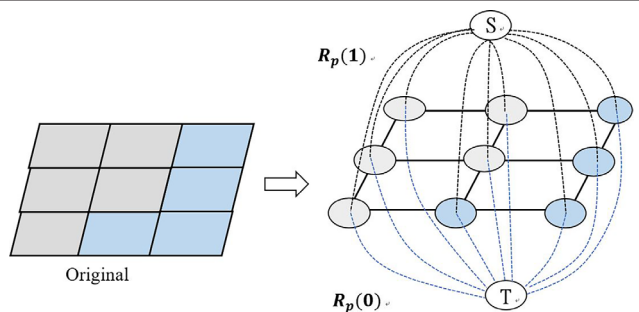


Figure 12. GrabCut s - t network diagram.

Parameter Sensitivity Analysis

In this section, the effects of different parameters on the final results are discussed. The four steps of this algorithm involve three main parameters: geodesic-distance weight γ_g , search range T_{se} , and geodesic-distance threshold T_{geo} , as shown in Table 2.

Using the data in this article, the real contours of the image are hand-drawn by reference to the DSM, and the sensitivities of the algorithm's precision, recall, and F_1 scores with respect to the three parameters are obtained, as shown in Figure 14.

Table 1. Experimental data sets.

Data set	Satellite	Band	Imaging area	Image size (pixels)
a	WorldView-3	4-Multispectral, 1.24 m 1-Pan, 0.31 m	Tripoli	948 × 914
b	WorldView-3	4-Multispectral, 1.24 m 1-Pan, 0.31 m	Tripoli	1036 × 706
c	WorldView-2	4-Multispectral, 1.8 m 1-Pan, 0.5 m	Guangzhou	798 × 853
d	WorldView-2	4-Multispectral, 1.8 m 1-Pan, 0.5 m	Guangzhou	1063 × 909
e	WorldView-3	4-Multispectral, 1.24 m 1-Pan, 0.31 m	Tripoli	1661 × 2104



(a) WorldView-3 Image Area1



(b) WorldView-3 Image Area2



(c) WorldView-2 Image Area1



(d) WorldView-2 Image Area2



(e) WorldView-3 Image Area 3

Figure 13. Experimental data in different areas.

Table 2. Parameters and descriptions.

Parameter	Description	Range
γ_g	The larger γ_g is, the larger the proportion of gradient difference.	0–1
T_{se}	If the value is too small, the search scope of interest point will be smaller, resulting in too few samples. If the value is too large, it is easy to take the point outside the building as the point of interest, thus causing false detections.	20–150
T_{geo}	The smaller the value, the more similar the pixel gradient and spectral value between the interest points and the seed points.	20–160

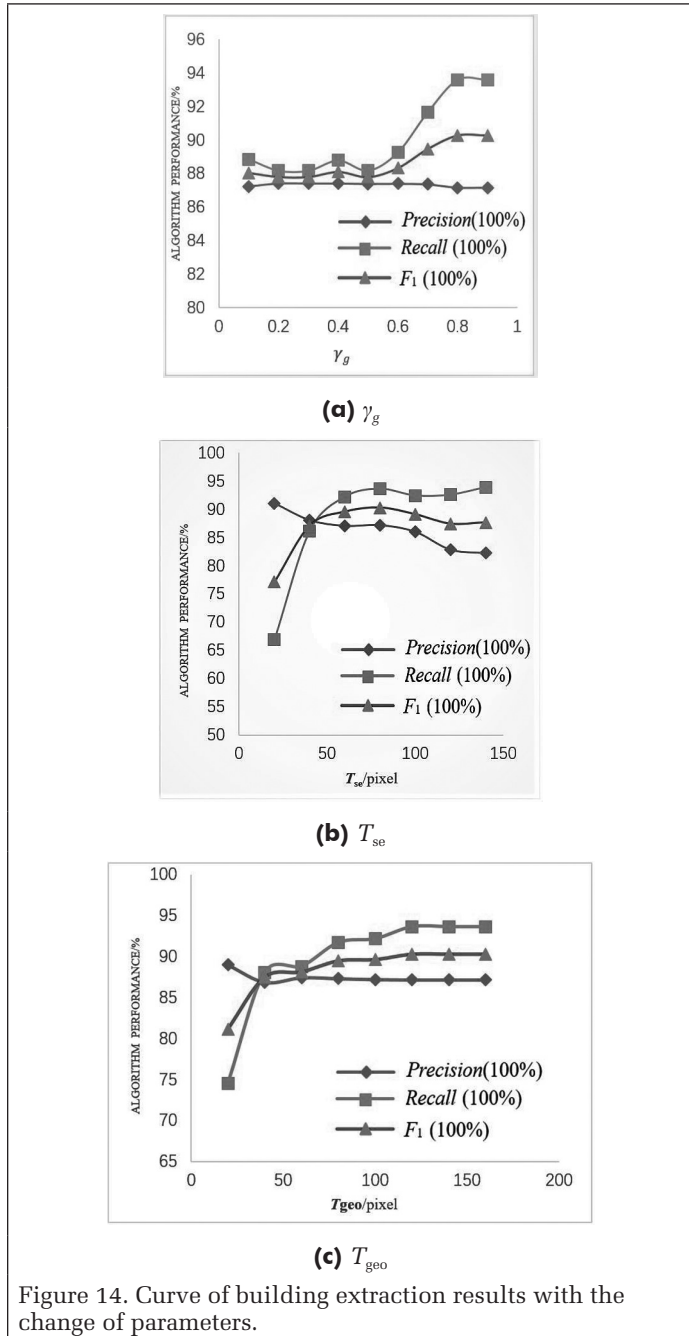


Figure 14. Curve of building extraction results with the change of parameters.

It can be seen that the three parameters have a certain regularity in their effects on the performance of the algorithm. Along the growth of parameter γ_g , the result changes slowly in the beginning, then reaches the maximum and stabilizes. When the parameters T_{se} and T_{geo} become larger, the results get better and tend to a fixed value. They both change quickly first and then tend to be stable. Therefore, the optimal thresholds of the algorithm can be determined as $\gamma_g = 0.9$, $T_{se} = 80$ pixels, and $T_{geo} = 100$.

Selection of Foreground and Background Samples

The selection of foreground and background samples depends on the quality of building elevation contour-line extraction. In order to extract the building elevation contour line better, both the high and low thresholds of the Canny detector were set to 200 (to keep the contour more detailed). After that, morphological closing operations were performed to fill the small holes in the contour, so that the contour looks more coherent.

The structure of morphological structural elements is very important to the final experimental results when the horizontal lines of buildings are extracted (Bibiloni, González-Hidalgo and Massanet 2017). In this experiment, structural elements of 15 pixels (a smaller value) were chosen to perform the morphological opening operations in the processed image to get more lines. Then the angle threshold was set to 90 and the horizontal lines were detected by the Hough transform. The threshold of FAST was set to 70 in order to adapt to different images and get more accurate corner points.

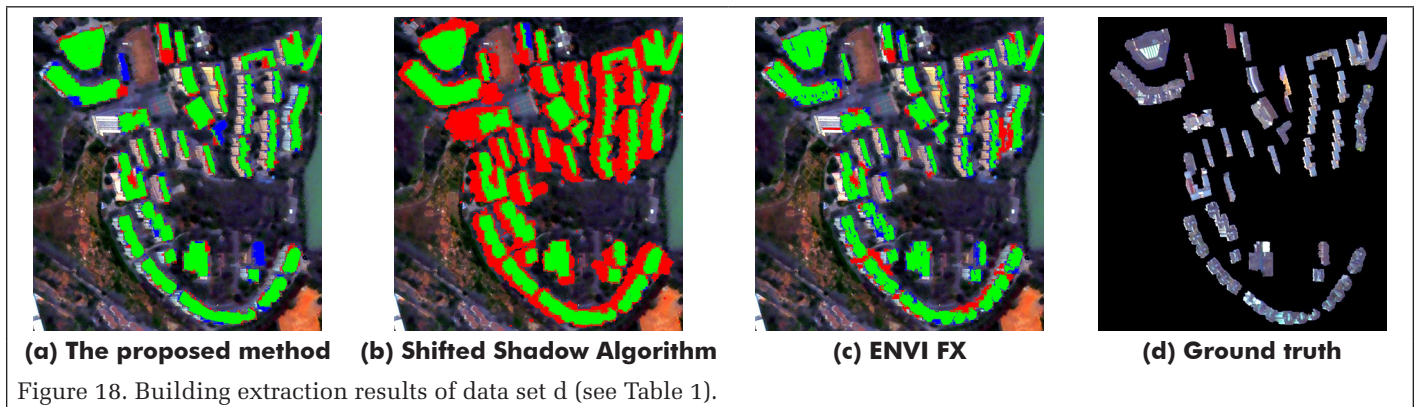
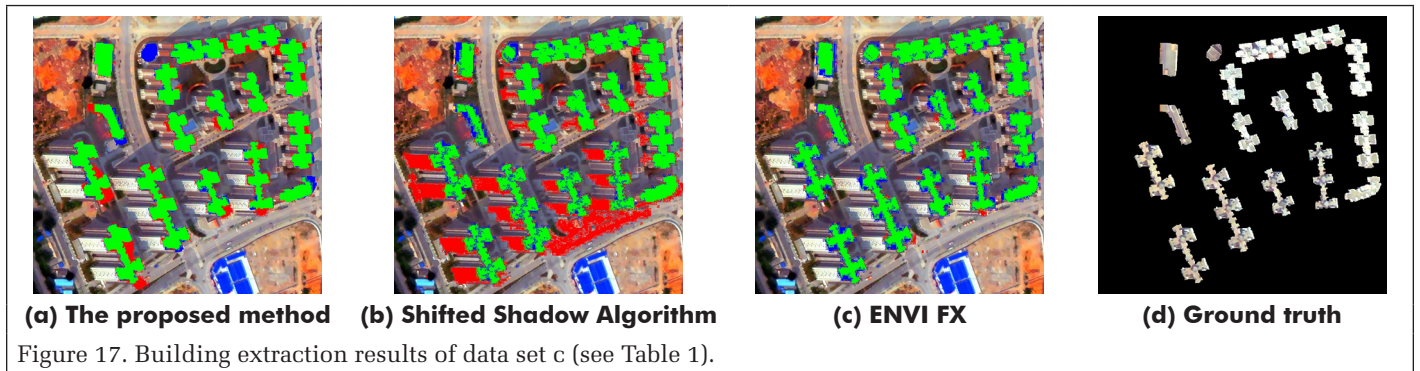
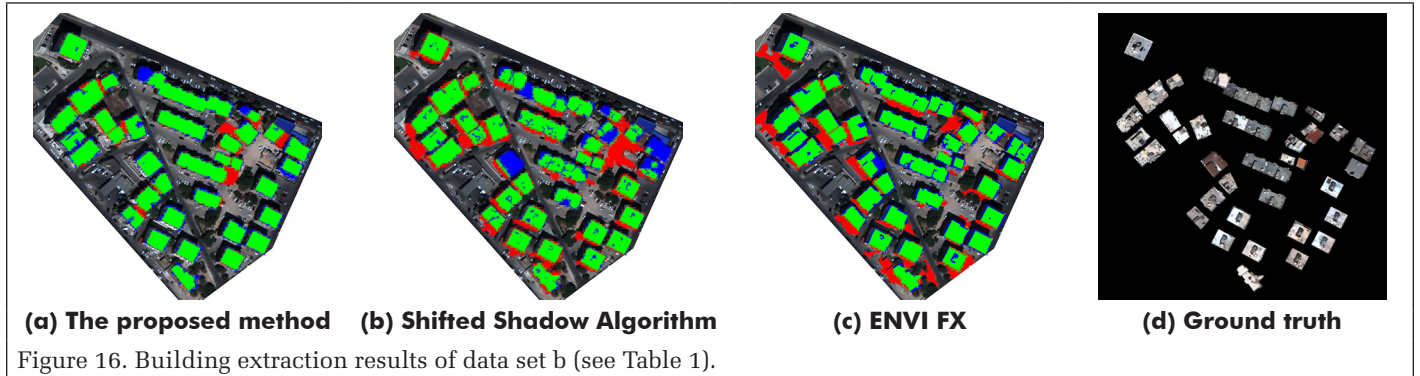
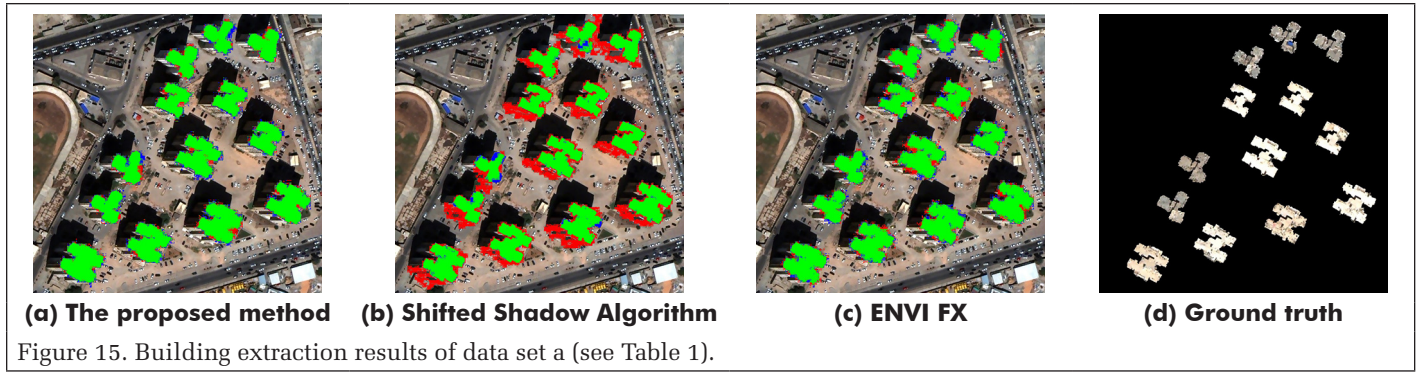
Method Comparison

In order to verify the effectiveness of the method proposed in this article, we selected for comparison the most popular software—ENVI 5.5 FX—and the most recent building extraction method, the shifted shadow algorithm (Gao *et al.* 2018). The extraction results and comparison of each method are shown in Figures 15–19. The true detection, false detection, and missed detection of building areas in the figures are colored in green, red, and blue, respectively. Specific accuracy comparisons are shown in Table 3.

The comparison demonstrates that the proposed method exceeded the compared methods in terms of F_1 score for all the tested data. The ENVI FX method requires a lot of manual work and takes a long time to determine the parameters of segmentation and fusion and to select the samples in the later stage. The shifted shadow algorithm, though using shadow as auxiliary information to accurately locate the initial building

Table 3. Comparison of building extraction results from various methods (highest results in boldface).

Data set	Method	Precision (%)	Recall (%)	F_1 (%)
a	Proposed method	91.58	90.52	91.04
	Shifted shadow algorithm	60.53	95.45	74.08
	ENVI FX	87.72	90.06	88.87
b	Proposed method	88.41	83.51	85.89
	Shifted shadow algorithm	69.66	79.29	74.16
	ENVI FX	73.14	81.91	77.28
c	Proposed method	87.84	84.12	85.94
	Shifted shadow algorithm	60.89	84.00	70.61
	ENVI FX	91.17	77.71	84.16
d	Proposed method	84.09	84.61	84.35
	Shifted shadow algorithm	45.44	98.18	62.13
	ENVI FX	80.30	82.33	81.30
e	Proposed method	85.78	83.24	84.48
	Shifted shadow algorithm	80.31	70.56	75.12
	ENVI FX	73.17	86.49	79.28



samples, did not effectively distinguish the roofs and elevations, resulting in a large number of false detections. In this article, the elevations of buildings are sampled separately, so that the roof contours of buildings can be distinguished well. In general, the average accuracy of the proposed method can reach 86.34%, which is 11.12% higher than that of the shifted shadow algorithm and 4.16% higher than that of ENVI FX. Nevertheless, because some building elevations are occluded by other objects, they cannot be effectively sampled, which leads

to missed detection, as shown in Figure 19a. This is the main limitation of the proposed method.

Conclusions

In this article, an effective and highly automated method of building extraction is proposed that can distinguish the top of a building from the elevation under the constraint of elevation contour lines, from a monocular optical high-resolution

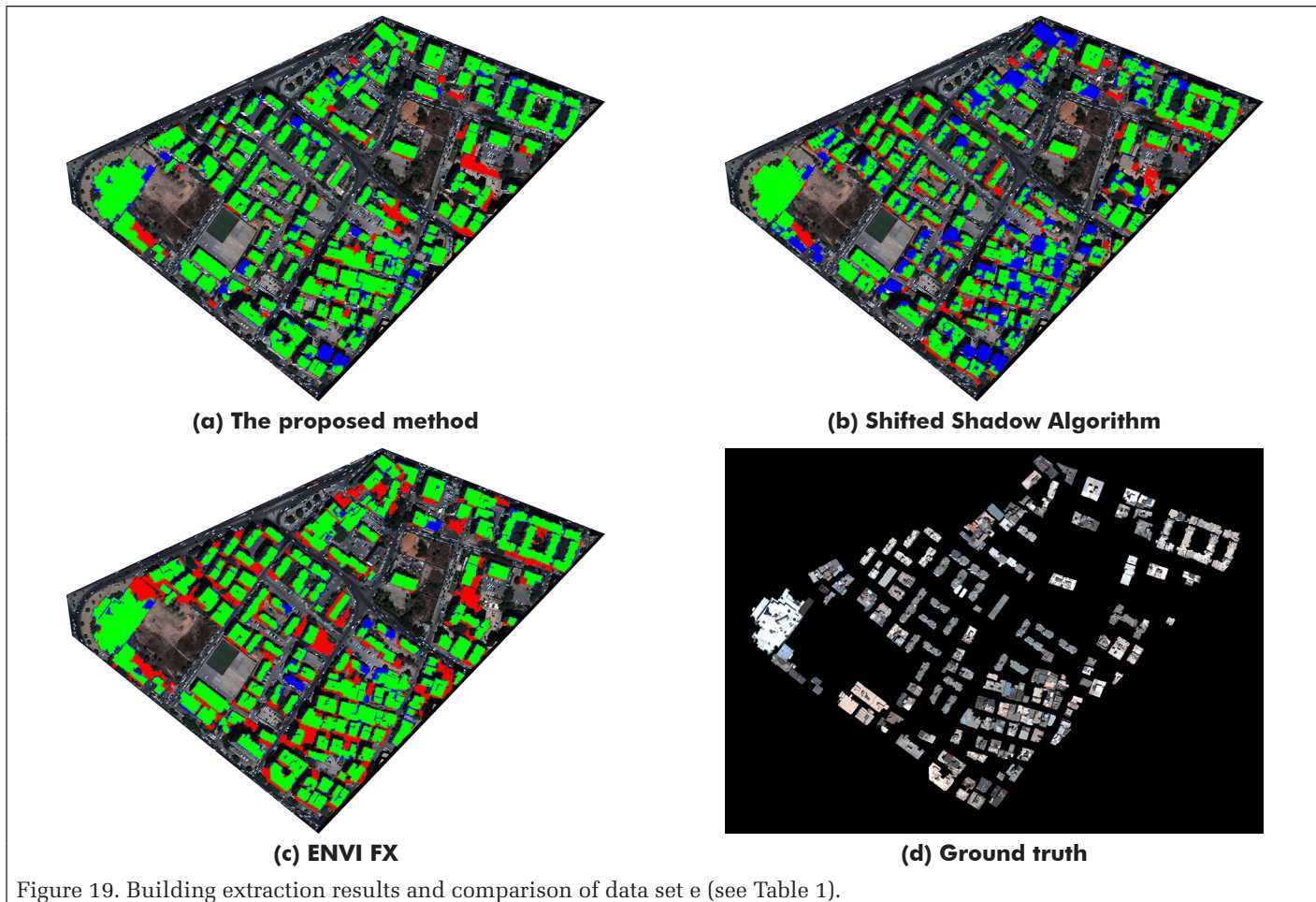


Figure 19. Building extraction results and comparison of data set e (see Table 1).

image. Compared with the method of using shadows as auxiliary information, the elevation contours of the building can not only accurately locate the building but also better reflect the relationship between the building roof and elevation. Moreover, image segmentation with GrabCut can better preserve the entire building boundary. In summary, the method has the following characteristics:

1. The method needs only the RGB image, meaning no other auxiliary data are needed. For the selection of samples, both foreground and background samples are automatically localized, and no sampling is required for the bare ground, vegetation, or shadow.
2. Without the use of DSM for orthorectification, building elevations in high-resolution images can be well distinguished from building-top contours, and thus false detections are reduced.

Acknowledgments

This work was supported by the Open Fund of Key Laboratory of Urban Land Resources Monitoring and Simulation, MNR, under grant number KF-2019-04-003; by the National Natural Science Foundation of China under grant number 41631175; by the Marine Science and Technology Innovation Project of Jiangsu Province under grant number HY2018-3; by the National Key Research and Development Plan of China under grants 2017YFB0503500 and 2017YFB0503504; and by the Priority Academic Program Development of Jiangsu Higher Education Institutions under grant number 164320H116.

References

- Bibiloni, P., M. González-Hidalgo and S. Massanet. 2017. General-purpose curvilinear object detection with fuzzy mathematical morphology. *Applied Soft Computing* 60:655–669.
- Cao, Q., L. Gu, R. Ren and L. Wang. 2016. Research of building information extraction and evaluation based on high-resolution remote-sensing imagery. *Proceedings of SPIE* 9976:99760Y.
- Cheng, G. and J. Han. 2016. A survey on object detection in optical remote sensing images. *ISPRS Journal of Photogrammetry and Remote Sensing* 117:11–28.
- Cote, M. and P. Saeedi. 2013. Automatic rooftop extraction in nadir aerial imagery of suburban regions using corners and variational level set evolution. *IEEE Transactions on Geoscience and Remote Sensing* 51 (1):313–328.
- Cui, S., Q. Yan and P. Reinartz. 2012. Complex building description and extraction based on Hough transformation and cycle detection. *Remote Sensing Letters* 3 (2):151–159.
- El-naggar, A. M., 2018. Determination of optimum segmentation parameter values for extracting building from remote sensing images. *Alexandria Engineering Journal* 57 (4):3089–3097.
- Fernandes, V. J. M. and A. P. Dal Poz, 2017. Extraction of building roof contours from the integration of high-resolution aerial imagery and laser data using Markov random fields. *International Journal of Image and Data Fusion* 9 (4):263–286.
- Gao, X., M. Wang, Y. Yang and G. Li. 2018. Building extraction from RGB VHR images using shifted shadow algorithm. *IEEE Access* 6:22034–22045.
- Grodecki, J. and G. Dial. 2003. Block adjustment of high-resolution satellite images described by rational polynomials. *Photogrammetric Engineering and Remote Sensing* 69(1):59–68.

- Gulshan, V., C. Rother, A. Criminisi, A. Blake and A. Zisserman. 2010. Geodesic Star convexity for interactive image segmentation. Pages 3129–3136 in *2010 IEEE Conference on Computer Vision and Pattern Recognition*, held in San Francisco, Calif., 13–18 June 2010. Edited by J. Editor. City, St.: Institute of Electrical and Electronics Engineers.
- Huang, J., X. Zhang, Q. Xin, Y. Sun and P. Zhang. 2019. Automatic building extraction from high-resolution aerial images and LiDAR data using gated residual refinement network. *ISPRS Journal of Photogrammetry and Remote Sensing* 151:91–105.
- Huang, X., W. Yuan, J. Li and L. Zhang. 2017. A new building extraction postprocessing framework for high-spatial-resolution remote-sensing imagery. *IEEE Journal of Selected Topics in Applied Earth Observations and Remote Sensing* 10 (2):654–668.
- Jannati, M., M. J. V. Zoj and M. Mokhtarzade. 2018. A novel approach for epipolar resampling of cross-track linear pushbroom imagery using orbital parameters model. *ISPRS Journal of Photogrammetry and Remote Sensing* 137:1–14.
- Kim, S. and S. Rhee. 2018. Semi-automatic extraction of 3D building boundary using DSM from stereo images matching. *Korean Journal of Remote Sensing* 34 (6):1067–1087.
- Kim, T. 2000. A study on the epipolarity of linear pushbroom images. *Photogrammetric Engineering and Remote Sensing* 66:961–966.
- Li, Y., J. Zhang, P. Gao, L. Jiang and M. Chen. 2018. Grab Cut image segmentation based on image region. Pages 311–315 in *2018 3rd IEEE International Conference on Image, Vision and Computing*, held in Chongqing, China, 27–29 June 2018. Edited by J. Editor. City, St.: Institute of Electrical and Electronics Engineers.
- Liu, S., Z. Zhang, B. Xiao and X. Cao. 2015. Ground-based cloud detection using automatic graph cut. *IEEE Geoscience and Remote Sensing Letters* 12 (6):1342–1346.
- Liu, Y., Z. Zhang, R. Zhong, D. Chen, Y. Ke, J. Peethambaran, C. Chen and L. Sun. 2018. Multilevel building detection framework in remote sensing images based on convolutional neural network. *IEEE Journal of Selected Topics in Applied Earth Observations and Remote Sensing* 11 (10):3688–3700.
- Manno-Kovacs, A. and T. Sziranyi. 2015. Orientation-selective building detection in aerial image. *ISPRS Journal of Photogrammetry and Remote Sensing* 108:94–112.
- Moghaddam, S. H. A., M. Mokhtarzade and S. A. A. Moghaddam. 2018. Optimization of RFM's structure based on PSO algorithm and figure condition analysis. *IEEE Geoscience and Remote Sensing Letters* 15 (8):1179–1183.
- Morgan, M., K.-O. Kim, S. Jeong and A. Habib. 2006. Epipolar resampling of space-borne linear array scanner scenes using parallel projection. *Photogrammetric Engineering and Remote Sensing* 72 (11):1255–1263.
- Ngo, T.-T., C. Collet and V. Mazet. 2015. Automatic rectangular building detection from VHR aerial imagery using shadow and image segmentation. Pages 1483–1487 in *2015 IEEE International Conference on Image Processing*, held in Québec City, Canada, 27–30 September 2015. Edited by J. Editor. City, St.: Publisher.
- Ok, A. O., C. Senaras and B. Yuksel. 2013. Automated detection of arbitrarily shaped buildings in complex environments from monocular VHR optical satellite imagery. *IEEE Transactions on Geoscience and Remote Sensing* 51 (3):1701–1717.
- Privalov, M. and M. Kazantsev. 2018. CT images segmentation algorithm based on graph cuts. Pages 1–6 in *2018 International Multi-Conference on Industrial Engineering and Modern Technologies*, held in Vladivostok, Russia, 3–4 October 2018. Edited by J. Editor. City, St.: Publisher.
- Rachmawati, E., I. Supriana and M. L. Khodra. 2017. FAST corner detection in polygonal approximation of shape. Pages 166–170 in *2017 3rd International Conference on Science in Information Technology*, held in Bandung, Indonesia, 25–26 October 2017. Edited by L. S. Riza, A. Pranolo, A. P. Wibawa, E. Junaeti, Y. Wihardi, U. R. Hashim, S.-J. Horng, R. Drezewski, H. S. Lim, G. Chakraborty, L. Hernandez and S. Nazir. City, St.: Institute of Electrical and Electronics Engineers.
- Reza, M. N., I. S. Na, S. W. Baek and K.-H. Lee. 2019. Rice yield estimation based on K-means clustering with graph-cut segmentation using low-altitude UAV images. *Biosystems Engineering* 177:109–121.
- Ullah, M., A. Iltaf, Q. Hou, F. Ali and C. Liu. 2018. A foreground extraction approach using convolutional neural network with graph cut. Pages 40–44 in *2018 3rd IEEE International Conference on Image, Vision and Computing*, held in Chongqing, China, 27–29 June 2018. Edited by J. Editor. City, St.: Institute of Electrical and Electronics Engineers.
- Wang, J., X. Yang, X. Qin, X. Ye and Q. Qin. 2015. An efficient approach for automatic rectangular building extraction from very high resolution optical satellite imagery. *IEEE Geoscience and Remote Sensing Letters* 12 (3):487–491.
- Wang, M., F. Hu and J. Li. 2011. Epipolar resampling of linear pushbroom satellite imagery by a new epipolarity model. *ISPRS Journal of Photogrammetry and Remote Sensing* 66 (3):347–355.
- Wurm, M., T. Stark, X. X. Zhu, M. Weigand and H. Taubenböck. 2019. Semantic segmentation of slums in satellite images using transfer learning on fully convolutional neural networks. *ISPRS Journal of Photogrammetry and Remote Sensing* 150:59–69.
- Xu, Z., X. Baojie and W. Guoxin. 2017. Canny edge detection based on Open CV. Pages 53–56 in *2017 13th IEEE International Conference on Electronic Measurement & Instruments*, held in Yangzhou, China, 20–22 October 2017. Edited by J. Editor. City, St.: Institute of Electrical and Electronics Engineers.
- Yu, Y., J. Zhu and J. Pei. 2018. Foreground target extraction in bounding box based on sub-block region growing and Grab Cut. Pages 344–349 in *2018 14th IEEE International Conference on Signal Processing*, held in Beijing, China, 12–16 August 2018. Edited by B. Yuan, Q. Ruan, Y. Zhao and G. An. City, St.: Institute of Electrical and Electronics Engineers.
- Zarea, A. and A. Mohammadzadeh. 2016. A novel building and tree detection method from LiDAR data and aerial images. *IEEE Journal of Selected Topics in Applied Earth Observations and Remote Sensing* 9 (5):1864–1875.
- Zheng, Q., H. Li, B. Fan, S. Wu and J. Xu. 2018. Integrating support vector machine and graph cuts for medical image segmentation. *Journal of Visual Communication and Image Representation* 55:157–165.

ASPRS Code of Ethics

Honesty, justice, and courtesy form a moral philosophy which, associated with mutual interest among people, should be the principles on which ethics are founded.

Each person who is engaged in the use, development, and improvement of the mapping sciences (Photogrammetry, Remote Sensing, Geographic Information Systems, and related disciplines) should accept those principles as a set of dynamic guides for conduct and a way of life rather than merely for passive observance. It is an inherent obligation to apply oneself to one's profession with all diligence and in so doing to be guided by this Code of Ethics.

Accordingly, each person in the mapping sciences profession shall have full regard for achieving excellence in the practice of the profession and the essentiality of maintaining the highest standards of ethical conduct in responsibilities and work for an employer, all clients, colleagues and associates, and society at large, and shall . . .

1. Be guided in all professional activities by the highest standards and be a faithful trustee or agent in all matters for each client or employer.
2. At all times function in such a manner as will bring credit and dignity to the mapping sciences profession.
3. Not compete unfairly with anyone who is engaged in the mapping sciences profession by:
 - a. Advertising in a self-laudatory manner;
 - b. Monetarily exploiting one's own or another's employment position;
 - c. Publicly criticizing other persons working in or having an interest in the mapping sciences;
 - d. Exercising undue influence or pressure, or soliciting favors through offering monetary inducements.
4. Work to strengthen the profession of mapping sciences by:
 - a. Personal effort directed toward improving personal skills and knowledge;
 - b. Interchange of information and experience with

other persons interested in and using a mapping science, with other professions, and with students and the public;

- c. Seeking to provide opportunities for professional development and advancement of persons working under his or her supervision;
 - d. Promoting the principle of appropriate compensation for work done by person in their employ.
5. Undertake only such assignments in the use of mapping sciences for which one is qualified by education, training, and experience, and employ or advise the employment of experts and specialists when and whenever clients' or employers' interests will be best served thereby.
6. Give appropriate credit to other persons and/or firms for their professional contributions.
7. Recognize the proprietary, privacy, legal, and ethical interests and rights of others. This not only refers to the adoption of these principles in the general conduct of business and professional activities, but also as they relate specifically to the appropriate and honest application of photogrammetry, remote sensing, geographic information systems, and related spatial technologies. Subscribers to this code shall not condone, promote, advocate, or tolerate any organization's or individual's use of these technologies in a manner that knowingly contributes to:
 - a. deception through data alteration;
 - b. circumvention of the law;
 - c. transgression of reasonable and legitimate expectation of privacy.

Topographic and Geomorphological Mapping and Analysis of the Chang'E-4 Landing Site on the Far Side of the Moon

Bo Wu, Fei Li, Han Hu, Yang Zhao, Yiran Wang, Peipei Xiao, Yuan Li, Wai Chung Liu, Long Chen, Xuming Ge, Mei Yang, Yingqiao Xu, Qing Ye, Xueying Wu, and He Zhang

Abstract

The Chinese lunar probe Chang'E-4 successfully landed in the Von Kármán crater on the far side of the Moon. This paper presents the topographic and geomorphological mapping and their joint analysis for selecting the Chang'E-4 landing site in the Von Kármán crater. A digital topographic model (DTM) of the Von Kármán crater, with a spatial resolution of 30 m, was generated through the integrated processing of Chang'E-2 images (7 m/pixel) and Lunar Reconnaissance Orbiter (LRO) Laser Altimeter (LOLA) data. Slope maps were derived from the DTM. Terrain occlusions to both the Sun and the relay satellite were studied. Craters with diameters ≥ 70 m were detected to generate a crater density map. Rocks with diameters ≥ 2 m were also extracted to generate a rock abundance map using an LRO narrow angle camera (NAC) image mosaic. The joint topographic and geomorphological analysis identified three subregions for landing. One of them, recommended as the highest-priority landing site, was the one in which Chang'E-4 eventually landed. After the successful landing of Chang'E-4, we immediately determined the precise location of the lander by the integrated processing of orbiter, descent and ground images. We also conducted a detailed analysis around the landing location. The results revealed that the Chang'E-4

lander has excellent visibility to the Sun and relay satellite; the lander is on a slope of about 4.5° towards the southwest, and the rock abundance around the landing location is almost 0. The developed methods and results can benefit future soft-landing missions to the Moon and other celestial bodies.

Introduction

On 3 January 2019, the Chinese lunar probe Chang'E-4, carrying the Jade Rabbit-2 lunar rover, successfully landed in the Von Kármán crater in the northwestern South Pole-Aitken (SPA) basin on the far side of the Moon (Figure 1). Chang'E-4 was the first spacecraft to make a soft landing on the lunar far side. The Chang'E-4 lander and the Jade Rabbit-2 rover are now exploring the surface and subsurface of the Von Kármán crater's mare-covered floor with their onboard scientific instruments. Their tasks include investigating the compositions of mare basalt and the subsurface structure of the regolith of this far side region (Wu *et al.* 2017), and finding clues that could provide insight into the early geologic history of the Moon (Wilhelms, John, and Trask 1987; Huang *et al.* 2018; Li *et al.* 2019; Di *et al.* 2019).

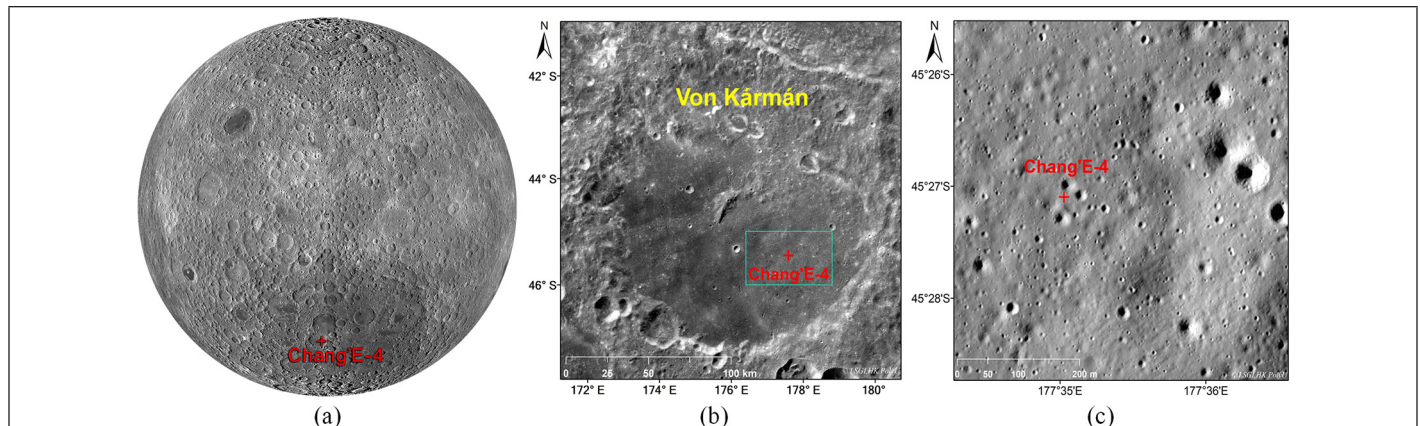


Figure 1. The Chang'E-4 landing site. (a) The landing site shown in a global view of the far side of the Moon; (b) an enlarged view of the landing site inside the Von Kármán crater shown in a Chang'E-2 image, with the green box indicating the targeted landing region; and (c) a further enlarged view of the landing site shown in a LRO NAC image.

Bo Wu, Han Hu, Yiran Wang, Peipei Xiao, Yuan Li, Wai Chung Liu, Long Chen, and Xuming Ge are with the Department of Land Surveying and Geo-Informatics, The Hong Kong Polytechnic University, Hung Hom, Kowloon, Hong Kong (bo.wu@polyu.edu.hk).

Fei Li, Yang Zhao, Mei Yang, Yingqiao Xu, Qing Ye, Xueying Wu, and He Zhang are with the China Academy of Space Technology, 104 Youyi Street, Haidian, Beijing, P.R. China (kuokuolee@163.com).

Photogrammetric Engineering & Remote Sensing
Vol. 86, No. 4, April 2020, pp. 247–258.
0099-1112/20/247–258

© 2020 American Society for Photogrammetry
and Remote Sensing
doi: 10.14358/PERS.86.4.247

Chang'E-4 is part of the second phase of the Chinese Lunar Exploration Program (Wu *et al.* 2017; Jia *et al.* 2018). This probe is a former backup of the Chang'E-3 probe (Jia *et al.* 2018), which made a successful lunar landing in the Sinus Iridum region in the Mare Imbrium on 14 December 2013 (Wu *et al.* 2014a). Unlike the landing site of the Chang'E-3, the targeted landing region of Chang'E-4 is on the far side of the Moon; therefore, a relay satellite was sent to the Earth-Moon Lagrangian Point 2 (L2) halo orbit in May 2018, which serves as a communication relay station between Earth and the lunar far side (Jia *et al.* 2018).

The selection of the Chang'E-4 landing site includes several steps. In the first step, two craters located inside the SPA basin, including the Von Kármán crater and the nearby Chretien crater, were selected. This is because a similar latitude to the Chang'E-3 landing site was preferred (i.e., at about 45°S in latitude) and due to the temperature and communication constraints. At the latitude of about 45°S inside the SPA basin, the Von Kármán crater and Chretien crater are superior to others in terms of crater size and roughness of the crater floor. In the second step, two candidate landing regions located inside the Von Kármán crater and Chretien crater, each covering an area of about 50 × 30 square kilometers, were selected for detailed analysis in terms of surface elevations, terrain slopes, and terrain occlusions to sun illumination and telecommunication. The candidate landing region located in the southeast floor of the Von Kármán crater, outlined in Figure 1b by the green box, was chosen based on its superiority in all these aspects.

To ensure a safe and successful landing, a careful analysis of the topography and geomorphology (De Rosa *et al.* 2012; Wu *et al.* 2014a) of the targeted landing region for further selecting a suitable landing site is critical. Topographic features, such as surface slopes and occlusions, along with geomorphological features such as the distributions of craters and boulders/rocks, were mapped and analyzed to identify the best suitable site for landing. In this research, we created digital topographic models (DTMs) of the Von Kármán crater at a spatial resolution of 30 m through the integrated processing of Chang'E-2 images and Lunar Reconnaissance Orbiter (LRO) Laser Altimeter (LOLA) data (Wu, Hu, Guo 2014b). Based on the DTMs, we scrutinized the surface slopes and terrain occlusions to the solar illumination and the relay satellite. Based on the Chang'E-2 images and the high-resolution LRO narrow angle camera (NAC) images, we analyzed the crater distribution and rock abundance inside the targeted landing region. The topographic and geomorphological features were then analyzed jointly to identify three subregions for landing. Chang'E-4 eventually landed in the subregion of the highest priority on 3 January 2019. After the landing, we precisely located the lander by using the images collected both in orbit and during the descent phase, together with a ground panorama collected by the lander's overhead camera upon landing. A detailed terrain occlusion analysis around the landing location was performed, and a 1.5 m/pixel DTM was generated using the shape-from-shading (SfS) approach (Wu *et al.* 2018a). This made it possible to conduct detailed topographic analyses to support the surface operations of the lander and rover.

This paper focuses on the targeted landing region inside the Von Kármán crater. It is organized as follows. The next section describes the methods and results regarding topographic mapping, with the topic of geomorphological mapping reserved for the section "Geomorphologic Mapping and Analysis of the Landing Region". The joint topographic and geomorphological analysis with the purpose of identifying subregions for landing are presented in the subsequent section. The section "Landing Site Localization and Analysis" includes further results regarding the precision localization of the lander and a detailed analysis of the surface slopes and occlusions around the landing site. Finally, the last section offers concluding remarks and discussion.

Topographic Mapping and Analysis of the Landing Region

Topographic Mapping

High-resolution DTMs are the vital data resources for topographic analysis of the targeted landing region. Currently, the Selenological and Engineering Explorer (SELENE) and LRO digital elevation model (SLDEM) generated by the co-registration of the photogrammetric results from the SELENE imagery and the LOLA measurements (Barker *et al.* 2016), provides full coverage of the targeted landing region at a spatial resolution of about 60 m. The SLDEM offers a typical vertical accuracy of 3 to 4 m. The SLDEM has favorable geometric accuracies but sparse spatial resolution. In this research, we used the Chang'E-2 images (7 m/pixel) covering the Von Kármán crater to generate a DTM with a spatial resolution of 30 m by the integrated processing with the LOLA measurements (Wu, Hu, Guo 2014b).

The Chang'E-2 camera consists of two linear push broom sensors with a convergence angle of about 25° that are used to formulate an along-track stereo configuration of the images (Wu, Hu, Guo 2014b). There is an overlap of about 50% between the images in the adjacent tracks. We developed a combined block adjustment approach for the integrated processing of the multiple-track Chang'E-2 images and the LOLA measurements to generate high-precision DTMs. By doing so, inconsistencies can be reduced between the multiple-track Chang'E-2 images, and between the three-dimensional (3D) measurements from the Chang'E-2 images and the LOLA measurements. This approach was used for the integrated processing of the Chang'E-2 images and LOLA measurements covering the Von Kármán crater and thus improved the orientation parameters of Chang'E-2 images. Dense image matching was carried out on the stereo Chang'E-2 images to generate dense matches, using a texture-aware semiglobal matching algorithm (Hu *et al.* 2016). 3D point clouds were then generated from the matching results based on the improved image orientation parameters, and finally, a DTM of the region with a spatial resolution of 30 m was interpolated from the 3D point clouds. The generated DTM was compared with the SLDEM covering the same region. The results indicated that the former has a degree of geometric accuracy similar to the latter but offers better spatial resolution (Hu and Wu 2019).

Figure 2a shows a 3D view of the generated DTM covering the Von Kármán crater. The right column shows an enlarged view of the targeted landing region as marked with a red box in the left column. Based on the generated DTM, the Von Kármán crater measures about 180 km in diameter, with a rim-to-floor depth of about 5 km. The crater floor has a diameter of about 140 km, and there is a central peak of about 1.55 km in height in the middle part of the crater. Within the targeted landing region, the terrain surface has a minimum height of -6076 m and a maximum height of -5776 m, respectively, with respect to a reference sphere of radius 1737.4 km. Figure 2b shows the generated ortho-image mosaics. Based on the generated DTM, the Chang'E-2 images were ortho-rectified and mosaicked to generate an orthographic image mosaic covering the Von Kármán crater, as shown in the left column of Figure 2b, which has the same resolution of 7 m/pixel as the original Chang'E-2 images. Inside the targeted landing region, LRO NAC images were collected to generate an image mosaic with a higher spatial resolution (1.5 m/pixel), as shown in the right column of Figure 2b.

Slope Analysis

Surface slope is an important engineering constraint in landing site evaluation to ensure the stability of the lander during touchdown, which is the magnitude of the derivatives of the gridded topographic model (i.e., the DTM) at a specific baseline. With two grid cells required for slope calculation along one direction, the corresponding baseline for slope analysis is two times the spatial resolution of the DTM, which is 60

m for the DTM generated from the Chang'E-2 images. For any point in the DTM, slopes along the east-west and north-south directions are calculated based on the distance and elevation difference of the two neighboring grid cells, and the square root of the sum of their squares is calculated as the maximum slope at that point. The slope calculation method is consistent with those provided in popular software systems, such as ArcGIS. After the slopes of all the points in the DTM have been calculated, a slope map can be generated. Figure 3 shows the slope map and statistics of the targeted landing region at a baseline of 60 m. It can be seen that most of the region (99.7%) has slopes of less than 15°, and 96.9% of the region has slopes of less than 8°. Only 3.1% of the region has slopes larger than 8°, and those areas are mainly distributed inside some craters.

A baseline of 8 m is further imposed for slope analysis, considering the lander footprint size of about 4.5 m plus a buffer for attitude adjustment of the lander before touchdown. However, slope analysis at an 8-m baseline requires a higher resolution DTM. There is only one stereo pair of LRO NAC images covering a small portion of the middle-north part of the landing region that could be used to generate a DTM of 4 m resolution. No high-resolution DTMs are available for other areas inside the landing region. In our previous work (Wang and Wu 2017), we presented a correlation analysis of slopes derived from the same terrain surface with different baselines. The results indicated that it is possible to estimate slopes at short baselines from slopes calculated from relatively longer baselines. The same method was used here for the estimation of slopes at different baselines. The 4-m resolution DTM from the stereo NAC images and the corresponding 30-m resolution DTM from the Chang'E-2 images, both covering the same local area inside the landing region, were used for correlation analysis of slopes at baselines of 8 m and 60 m. A slope amplification function with multipliers in the range of [1.1, 1.6] was obtained from the correlation analysis in this local area, which was then used for estimation of slopes at 8-m baseline in other areas inside the landing region, based on the assumption that the influences of different baselines on slopes should be similar for this local area and its nearby region. Therefore, we also compute an aggressive (the lower amplification bound of 1.1) and a conservative (the upper amplification bound of 1.6) estimation of the slopes at the 8 m baseline based on the original slopes at 60 m baseline. In the case of conservative estimations, about 3.4% of the areas have slopes larger than 8°, and this value only rises to about 5%, even in the aggressive case. Similarly, the areas with larger slopes are located inside the craters.

Occlusion Analysis

As the targeted landing region is on the floor of the Von Kármán crater and the height difference from the floor to the crater rim is about 5 km, it is crucial to analyze the possible terrain occlusions to solar illumination and communication signals from the relay satellite. The lander and rover rely on solar energy to charge the batteries of the onboard instruments. Also, communications and data transfer between the Earth control center and the lander require that the latter stays

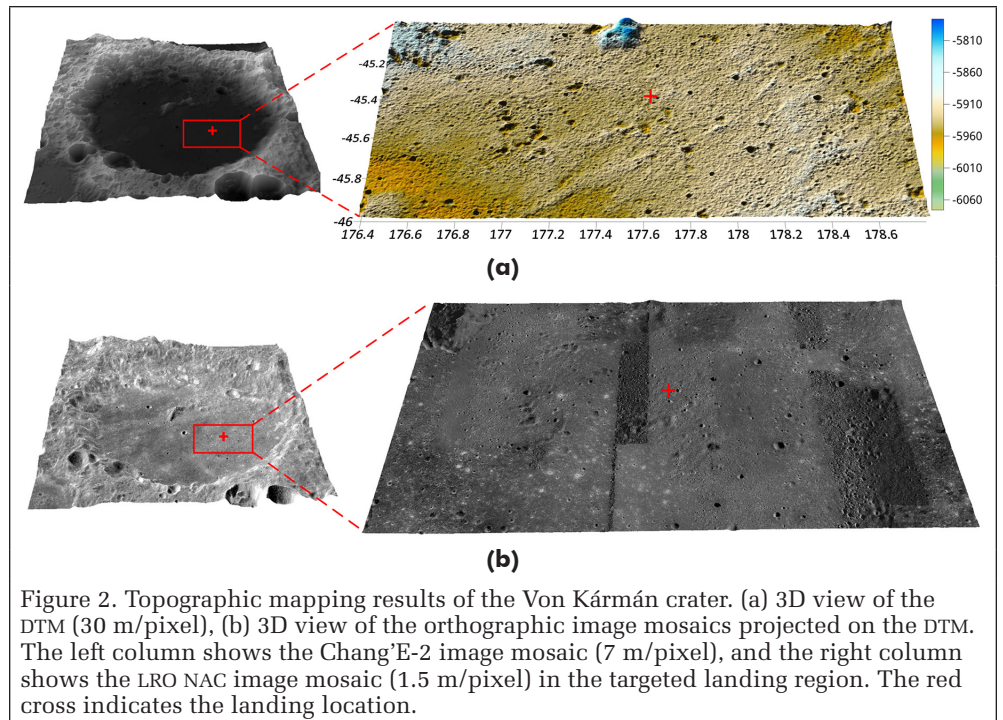


Figure 2. Topographic mapping results of the Von Kármán crater. (a) 3D view of the DTM (30 m/pixel), (b) 3D view of the orthographic image mosaics projected on the DTM. The left column shows the Chang'E-2 image mosaic (7 m/pixel), and the right column shows the LRO NAC image mosaic (1.5 m/pixel) in the targeted landing region. The red cross indicates the landing location.

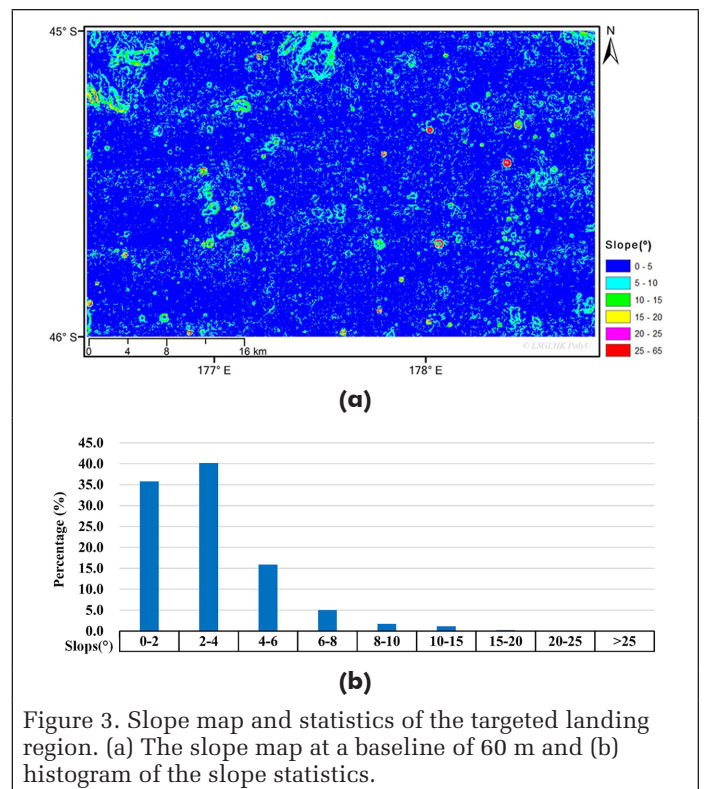


Figure 3. Slope map and statistics of the targeted landing region. (a) The slope map at a baseline of 60 m and (b) histogram of the slope statistics.

in the sight of the relay satellite. Therefore, areas with maximum visibility of the Sun and the relay satellite, that is, areas that feature the least amount of occlusion from the terrain, are preferred when evaluating landing site suitability.

In the analysis of the occlusion conditions caused by the terrain, a search radius of 200 km surrounding the targeted landing region is considered, to enclose the entire rim of the Von Kármán crater and some high mountains outside the crater that may cause occlusions. Due to the long distances involved when calculating terrain occlusion angles, the curvature of the lunar surface cannot be ignored. An approach

based on the geodesic line (Karney 2013) was developed to analyze the altitude angles of terrain occlusions, as illustrated in Figure 4. For each target point $A(\lambda_1, \varphi_1)$ at longitude λ_1 and latitude φ_1 in the landing region, a geodesic line l is determined by a specific azimuth angle α . Given a specific distance s_{12} , the geographic coordinates of the search point $B(\lambda_2, \varphi_2)$ can be determined based on the geodesic line (Karney 2013). The height of point B can be sampled from the DTM. Then, the 3D coordinates of B can be projected to a local Cartesian coordinate system of the target point A , in which the altitude and distance of B , with respect to the target point A , can be determined, and an altitude angle θ can be calculated to represent the terrain occlusion of point B to A . The process just described is repeated for all of the azimuth angles and the entire search radius of 200 km. The intervals for the azimuth angle α and geodesic distance s_{12} are set to be 1° and the spatial resolution of the DTM, respectively, considering the accuracy in capturing the topographic features and the processing time. Next, the maximum occlusion angle for point A along each azimuth direction can be determined, and the maximum occlusion angle among all the azimuth directions from 0° to 360° can be obtained. This procedure is further repeated for each grid point in the targeted landing region to generate the terrain occlusion map shown in Figure 5.

Figure 5 shows the terrain occlusion maps of the targeted landing region. Figure 5a shows the maximum altitude angle of terrain occlusion for each point inside the region, and Figure 5b shows the corresponding azimuth of the maximum altitude angle for each point. For most of the flat areas inside the landing region, the maximum terrain altitude angle is less than 10° . Also, most of the maximum altitude angles are caused by the rims of the Von Kármán crater in the southeast and east parts, as indicated by the azimuth map of terrain occlusion in Figure 5b. In the targeted landing region located in the southeast part of the crater floor, as shown in Figure 1, the southeast and east parts of the crater rim create larger terrain occlusions because they are closer to the landing region. In contrast, terrain occlusions in the northwest corner of Figure 5b show that the terrain occlusions in this part come from the northwest direction, either from the rim of the Von Kármán crater far to the northwest at a far distance or from the nearby central peak of Von Kármán crater, also located in the northwest of the landing region. The large terrain occlusions indicated in red or yellow in Figure 5a are inside the craters and along the slopes of the hills.

For a period of six months after the landing of Chang'E-4, from 3 January to 3 July 2019 (the designed working period of Chang'E-4), the solar azimuth and altitude of each point inside the landing region can be obtained from ephemeris information and compared with the altitude angle of the terrain occlusion along the same azimuth. The solar occlusion conditions are derived for each point by summarizing the possible occlusions of all the solar azimuth directions. Figure 6a presents the resulting percentage of visibility of the Sun during the six-month period over the entire region, with red representing occlusions to the Sun. It should be noted that the lander and rover hibernate during the lunar night and they will automatically wake up when the solar altitude angle is greater than 10° ; therefore, only the time slots with solar altitude angles greater than 10° (43.7% of the designed working period of six months) were considered in the above occlusion analysis. It can be seen from Figure 6a that a majority (99.8%) of the landing region has 100% visibility of the Sun during the six-month period (excluding the time when the solar altitude angles are $\leq 10^\circ$); however, in some areas, especially inside small craters and near hills, the solar visibility is as low as 86%.

Figure 6b presents the terrain occlusions to the relay satellite. As mentioned earlier, a relay satellite was sent to the Earth-Moon L2 point and stayed there in a halo orbit to provide continuous communication between the Earth

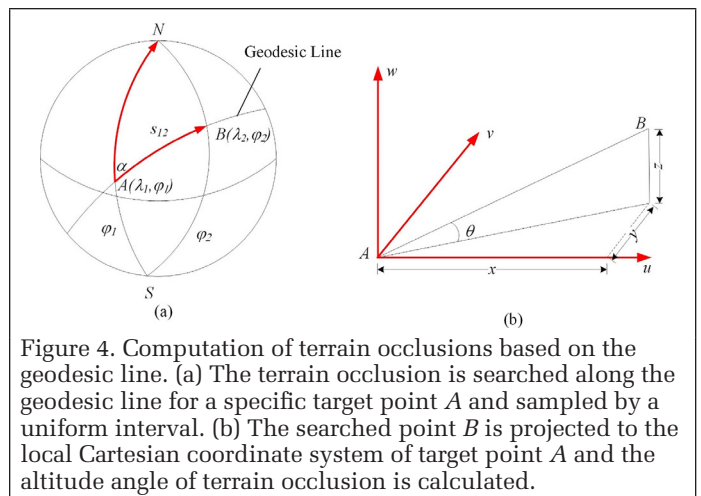


Figure 4. Computation of terrain occlusions based on the geodesic line. (a) The terrain occlusion is searched along the geodesic line for a specific target point A and sampled by a uniform interval. (b) The searched point B is projected to the local Cartesian coordinate system of target point A and the altitude angle of terrain occlusion is calculated.

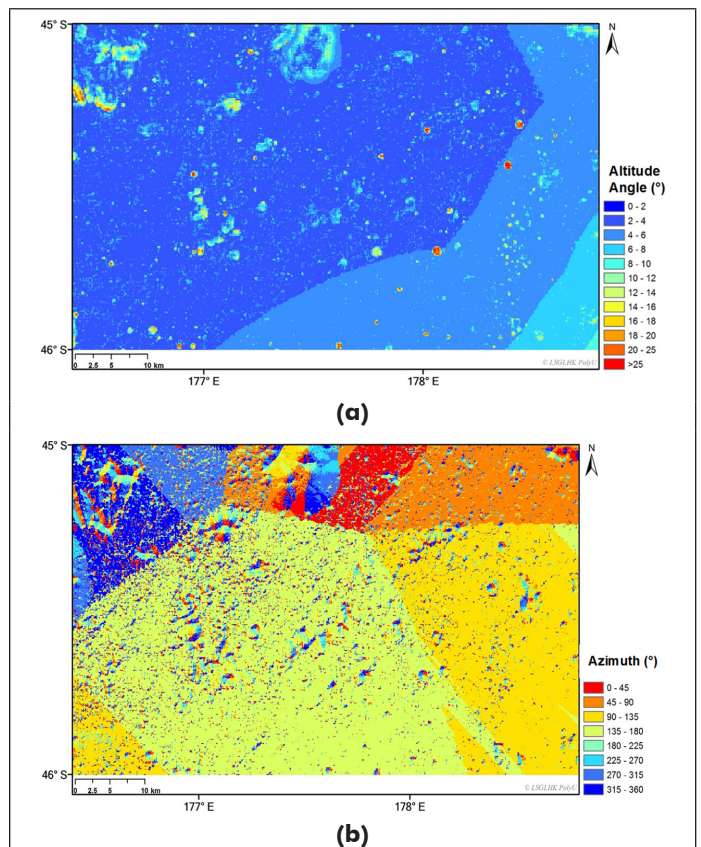


Figure 5. Terrain occlusion maps of the targeted landing region. (a) The maximum altitude angles of terrain occlusions for each point in all azimuth directions, (b) the corresponding azimuth angles for the maximum occlusion of each point.

control center and the Chang'E-4 lander on the far side of the Moon. For the same period of six months after the landing of Chang'E-4, the azimuth and altitude of the relay satellite with respect to each point inside the landing region were estimated from the orbit design of the relay satellite. An occlusion map to the relay satellite for the entire landing region was generated following the same process as for occlusion to the Sun, as shown in Figure 6b. As before, the time slots with solar altitude angles less than 10° , when the lander and rover hibernate, were ignored in the occlusion analysis. From Figure 6b, the relay satellite is 100% visible over the majority (99.98%) of the landing region during the six-month period of interest. Nevertheless, there are several places, shown in red, where the relay

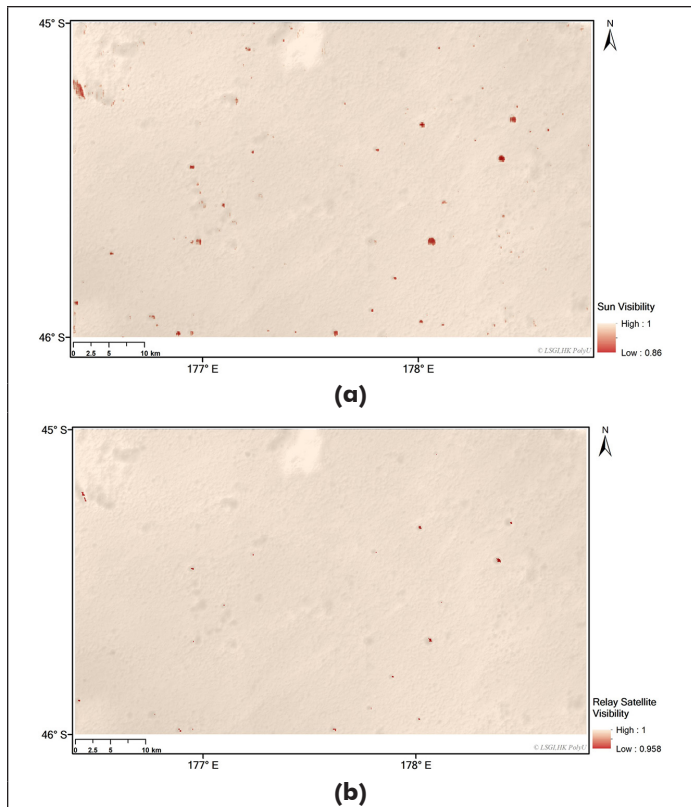


Figure 6. Visibility maps of the targeted landing region for the six-month period after the landing of Chang'E-4 from 3 January to 3 July 2019. (a) Visibility map to the Sun and (b) visibility map to the relay satellite.

satellite is visible only for 95.8% of the time. Fortunately, these places are rare and are distributed mainly inside a few craters or around the foot of the hill in the northwest of the landing region. The occlusions to the relay satellite are less severe compared with the occlusions to the Sun, as can be noted from Figure 6. This is reasonable considering that the altitudes of the relay satellite, with respect to the targeted landing region, are consistently larger than $\sim 25^\circ$ by the design of the halo orbit.

Geomorphologic Mapping and Analysis of the Landing Region

Crater Distribution

Craters are common geomorphologic features on the Moon. Craters are considered possible hazards in landing site evaluation due to their internal slopes and protuberant rims. Therefore, a lower crater density is preferred in selecting the landing site. Also, Chang'E-4 had to avoid landing in any small craters (a few meters to dozens of meters in diameter) to allow the maximum maneuvering capability of the rover (Brady *et al.* 2009; Wu *et al.* 2014a).

We developed an active machine-learning algorithm (Wang and Wu 2019) for automatic crater detection in the targeted landing region. The 7 m/pixel Chang'E-2 image mosaic was used for crater detection inside the landing region. We aimed to identify all craters larger than 70 m in diameter, which is equivalent to 10 pixels on the image, as the performance of our algorithm decreases for craters smaller than 10 pixels in diameter. It should be noted that the LRO NAC image mosaic was not used for crater detection here. Even though it offers higher resolution, LRO NAC imagery has varying illumination conditions and unbalanced image contrasts, as shown in the right column of Figure 2b, which will influence the crater detection and result in biases in crater density analysis across

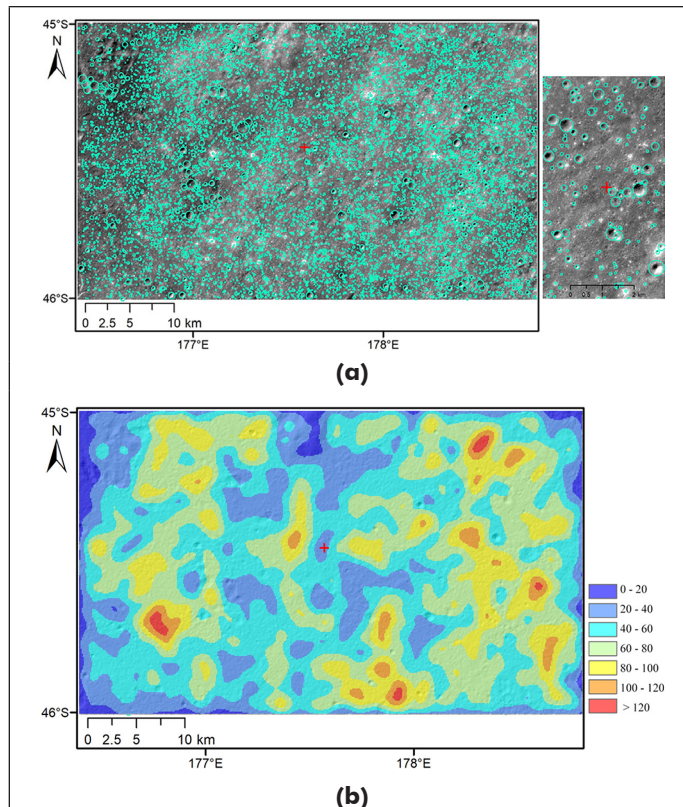


Figure 7. (a) Distribution of craters (≥ 70 m in diameter) in the targeted landing region. The red cross indicates the landing location, and the inset figure on the right shows an enlarged view of the detected craters around the landing location. (b) The crater density map in terms of crater numbers calculated using a moving circular window.

the landing region. By contrast, the Chang'E-2 image mosaic has consistent illumination and contrast conditions, as can be seen in the left column of Figure 2b. After the automatic crater detection on the Chang'E-2 image mosaic using the algorithm (Wang and Wu 2019), a manual checking process was further carried out to ensure the reliability of the detected craters, by digitizing missing craters and removing artifacts with the assistance of a grid with a cell size of $70 \text{ m} \times 70 \text{ m}$ overlaid on the image mosaic. Ultimately, 9391 craters with diameters ranging from 70 m to 1405 m were detected in the landing region. Figure 7a shows the distribution of those detected craters.

To understand the crater distribution in the targeted landing region, a crater density map depicting crater numbers in a unit area was generated, as shown in Figure 7b. The map was obtained by using a moving circular window with an area of 10 km^2 to count the numbers of craters. Smaller density represents a sparser distribution of craters and thus a relatively safer situation for landing. Figure 7b shows that the eastern part of the targeted landing region has relatively higher crater density compared with the central and western parts. The average crater density in the targeted landing region is about 60 craters over a circular window of 10 km^2 area.

Rock Abundance

Rocks are another type of major feature on the lunar surface that can be hazardous for the lander and rover. Rock abundance, defined as the cumulative fractional area covered by rocks with respect to their diameters, is another crucial factor in evaluating the suitability of finding a landing site for any landing mission (Golombek and Rapp 1997; Golombek *et al.* 2003; De Rosa *et al.* 2012; Wu *et al.* 2018b). For example, one

criterion for selecting the landing site of National Aeronautics and Space Administration's (NASA's) InSight mission on Mars was that the rock abundance had to be less than 10% (Golombek *et al.* 2017); and for the ExoMars mission of the European Space Agency, the rock abundance must be less than 7% (Pajola *et al.* 2017). In this research, a rock abundance constraint of 7% was considered in landing site evaluation given the ability of the lander and rover to tolerate rocks during their maneuvering.

We developed a rock detection algorithm (Li and Wu 2018) to extract rocks from the LRO NAC image mosaic. The algorithm detects rocks based on their particular brightness distributions and relief properties presented in the image. The details pertaining to this rock detection algorithm can be found in our previous work. Using the algorithm, a total of 21 004 rocks were identified from the LRO NAC image mosaic (1.5 m/pixel) covering the targeted landing region. The minimum size of rocks that were detected is 2 m (the longest diameter of the rock boundary), and the maximum size is 17.24 m. The detected rocks were manually checked by two independent operators to further ensure the reliability of rock detection. The distribution of the final detected rocks is shown in Figure 8a.

Figure 8a shows the distribution of rocks larger than 2 m within the targeted landing region. However, for landing site assessment, we will need to understand the overall distribution of rocks of all sizes. A rock abundance model developed by Li and Wu (2018) is used here, which allows us to infer the overall distribution of rocks of all sizes from rocks above a particular size. The rock abundance model has the following exponential format:

$$F_k(D) = ke^{-\left(\frac{0.5648 + \frac{0.01285}{k}}{D}\right)} \quad (1)$$

where D is the rock diameter, k is rock abundance, and $F_k(D)$ is the fractional area covered by rocks with diameters larger than D . Based on the rock detection result, the rock abundances were estimated using the above rock abundance model to generate a rock abundance map of the targeted landing region, as shown in Figure 8b. It should be noted that the rock abundance model can only be used to estimate the overall distribution of rocks in an area from the size-frequency distribution of the detected rocks. If no rock is detected from the image in a local area, this either indicates that the area is indeed rock-free, or there might be smaller rocks, but they are ignored. The latter case requires higher-resolution image data for checking the existence of smaller rocks. Nevertheless, the rock abundance map generated from the method above can still be used to analyze the relative rock abundances of different local areas in the targeted landing region.

The rock abundance map shown in Figure 8b was generated by calculating the fractional area of detected rocks within each tile of 250 m × 250 m inside the landing region and by further extrapolating the rock abundance values for each tile based on Equation 1. The tile size of 250 m was selected considering its statistical significance (Li and Wu 2018) and meaningfulness for comparing with LRO Diviner Radiometer data, as described below. According to the rock abundance map and the rock distribution map, as shown in Figure 8, most rocks are located around rocky impact craters and slopes of hills. Within the targeted landing region, 99.9% of the region has a rock abundance of < 7%, and 97.1% of the region has a rock abundance of < 1%. The highest rock abundance in the region is 18.21%, appearing on the slope of a rocky crater close to the south-western boundary of the target landing region located at (176.4488°E, 45.8222°S).

Our rock abundance map is further compared with the rock concentration map obtained from the LRO Diviner Radiometer data. Based on the contrasting thermal conductivities between rocks and lunar regolith, Bandfield *et al.* (2011) derived a rock concentration map (<http://ode.rsl.wustl.edu/moon/index.aspx>) using the LRO Diviner Radiometer data. The same reference system (Mean Earth/Polar Axis) and the same map projection (Mercator) were used for the Diviner map and the LRO NAC image mosaic, and we found that the two maps matched well in general by referring to the locations and shapes of some big craters commonly visible on them. The Diviner map has a spatial resolution of 128 pixels per degree (~250 m at the equator), and each pixel presents an aerial fraction of rocks with diameters larger than ~1 m. To compare with the Diviner map, the areal fraction of rocks ≥ 1 m was extrapolated from our detected rocks (≥ 2 m in diameter), which were then binned into pixels of the same scale of the Diviner bins, using the rock abundance model as shown in Equation 1. The differences between our results and the Diviner map in the landing region are shown in Figure 9a. The average absolute difference between our map and the Diviner map is 0.25%. The greatest positive difference is 12.8%, and the greatest negative difference is -2.2%, as shown in Figure 9b. The first row in Figure 9b shows the case in which the greatest positive difference appears. The fraction area of rocks (≥ 1 m) derived from our rock detection result is as high as 15.1%, while the Diviner result is only 2.3%, leading to a positive difference of 12.8%. Our higher value is more reasonable than the Diviner result considering that the areal fraction of the detected rocks (≥ 2 m) already reaches 8.2%. The reason for this kind of discrepancy might be that craters with various slopes may show a range of temperatures with the Diviner measurements, which may consequently lead to uncertainties

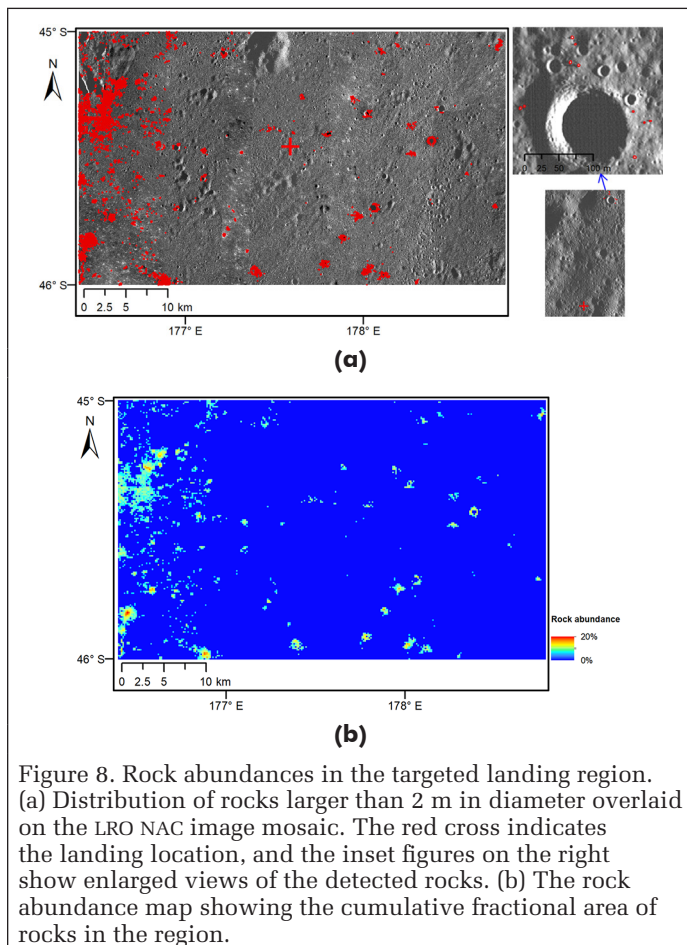


Figure 8. Rock abundances in the targeted landing region. (a) Distribution of rocks larger than 2 m in diameter overlaid on the LRO NAC image mosaic. The red cross indicates the landing location, and the inset figures on the right show enlarged views of the detected rocks. (b) The rock abundance map showing the cumulative fractional area of rocks in the region.

and errors (Li and Wu 2018; Bandfield *et al.* 2011). The second row in Figure 9b shows the greatest negative difference of -2.2% . This type of discrepancy can be attributed to the unfavorable illumination conditions in which rocks cannot be identified in the dark shadows. Fortunately, such shadowed areas cover less than 1% of the landing region.

Joint Topographic and Geomorphological Analysis for Landing Site Selection

The previously described topographic factors, including surface slopes and occlusions, and the geomorphologic factors, including crater distribution and rock abundance, are critical considerations when selecting suitable landing sites for Chang'E-4 to avoid hazards during touchdown and ensure favorable maneuverability of the robotic rover. Therefore, we carried out a joint topographic and geomorphologic analysis to identify subregions inside the targeted landing region that could be favorable for a safe landing.

The Chang'E-4 lander had an orbital inclination angle ranging from 80° to 100° from the east by orbit design dependent on the launching window. There were various uncertainties in orbit determination which might affect the actual landing (Li *et al.* 2017). In the longitude direction, considering the influence of midcourse orbit correction, near-Moon braking, and other orbit control errors, there were certain errors in the orbital inclination relative to the nominal design, which would be propagated along the longitude direction. In addition, simulation analysis of the powered descent phase also revealed kilometer-scale deviations in the longitude direction caused by the powered descent. In the latitude direction, uncertainties included the prediction error of the start point of the powered

descent phase and the thrust deviation of the 7500 N motor onboard the lander, which were also in kilometer scale. Considering the above engineering factors, a rectangle centered at the orbit track with a width of ± 5 km across the orbit direction and a length of ± 15 km along the orbit direction was defined as a subregion for landing. The targeted landing region was then divided into 25 subregions for detailed analysis, as shown in Figure 10a. There was a 2 km offset between any two neighboring subregions, and the areas beyond the targeted landing region were ignored in the analysis.

For all the 25 subregions, we examined five specific criteria to evaluate their suitability for a safe landing, including surface slopes, terrain occlusions to the Sun, terrain occlusions to the relay satellite, crater densities, and rock abundances. For each criterion, we set a soft threshold and scored the subregion based on the percentage of areas that exceed the threshold. For the slope threshold, 8° was applied on the slopes at the 8 m baseline. For the crater density, the average crater density of the landing region plus its standard deviation was used as the threshold, which was 78 craters (≥ 70 m in diameter) per 10 km^2 . For the rock abundance, 7% was used as the threshold. For the occlusions to both the Sun and relay satellite, we directly counted the percentages of areas with any occlusions during the six-month period after landing with respect to the total area of the subregion. It should be noted that some of these threshold parameters (e.g., slopes and rock abundance) were considered mainly based on the engineering constraints described previously. Some threshold parameters (e.g., the crater density) might not directly relate

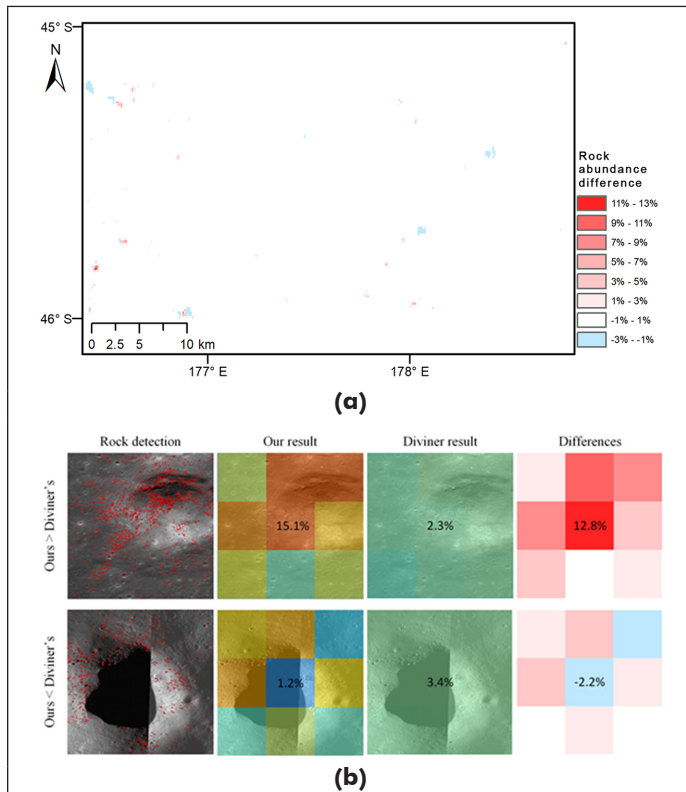


Figure 9. Comparison between the rock abundances from our results and the LRO Diviner Radiometer data in the targeted landing region. (a) Difference map of rock abundances (ours minus the Diviner map) and (b) enlarged views of examples for detailed comparison.

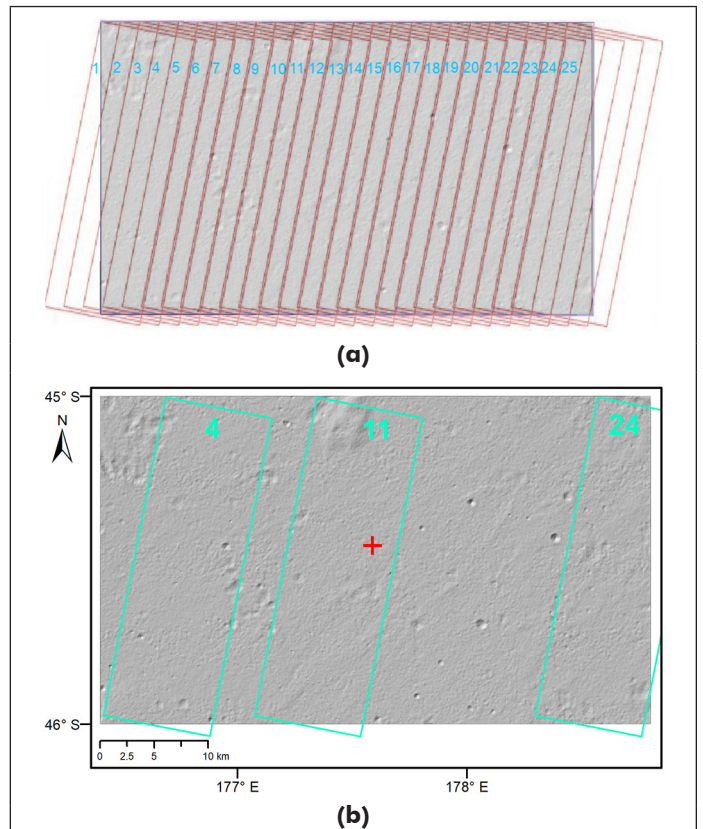


Figure 10. Joint analysis for selecting the subregion for landing. (a) 25 subregions covering the targeted landing region; (b) the three short-listed subregions, with 11 being the highest priority, where Chang'E-4 actually landed. The red cross indicates the exact landing location of Chang'E-4. The underlying image is a shaded relief of the DTM of the targeted landing region.

Table 1. Statistics of slopes, crater densities, rock abundances, and occlusions of the three short-listed subregions.

Subregion	Slope		Crater density		Rock abundance		Occlusion to the Sun (%)	Occlusion to the relay satellite (%)	Priority as landing site
	Average (°)	% of areas $\geq 8^\circ$	Average (no. craters per 10 km ²)	% of areas ≥ 78 craters per 10 km ²	Average (%)	% of areas $\geq 7\%$			
4	2.39	2.37	58	0.00	0.04	0.031	0.44	0.02	3
11	2.32	1.96	46	0.00	0.00	0.000	0.32	0.00	1
24	2.65	3.04	81	0.38	0.00	0.011	0.41	0.00	2

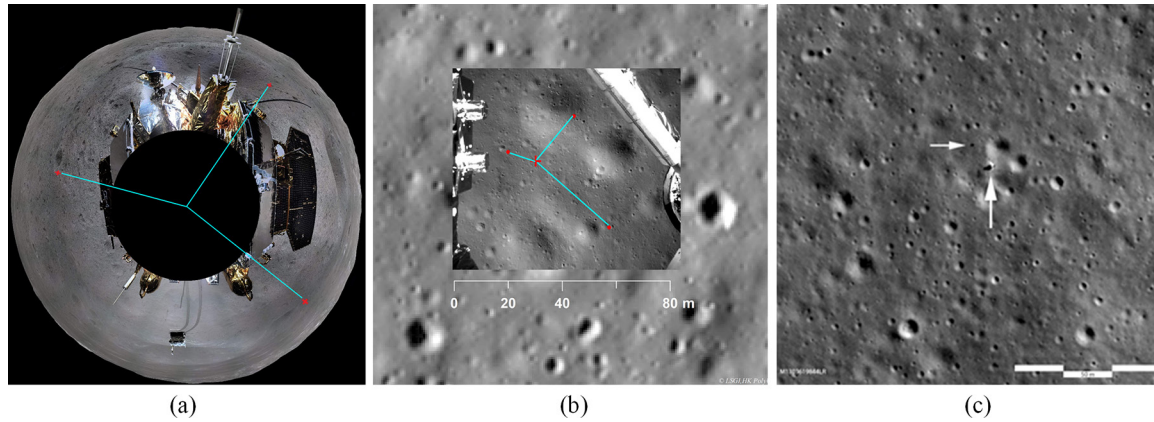


Figure 11. Localization of the Chang'E-4 lander. (a) Three small craters marked as red dots on the ground panorama image. (b) The corresponding positions of the craters marked on the descent image, which was geo-referenced with the LRO NAC image. The red cross indicates the lander location obtained by optimal cartographic triangulation. (c) The LRO NAC image (M1303619844LR) taken on 1 February 2019, showing the real locations of the lander and rover as indicated by the white arrows.

to an engineering constraint, but they worked fine as we were interested in the subregions of relatively favorable conditions.

We carried out the above analysis for all 25 subregions. The subregions (1–8) in the western part of the targeted landing region have relatively large slopes and rock abundances. Their crater densities are all below the threshold. The subregions (9–15) in the middle part have fewer slopes and rock abundances. Their crater densities are gradually increased. The subregions (16–25) in the eastern part have relatively large crater densities and slopes. Their rock abundances are moderate. For the occlusions to the Sun and the relay satellite, the first two subregions in the west and several subregions in the east (e.g., 19–23) have relatively large occlusions compared with other subregions. Comparing the subregions in the western, central, and eastern parts of the landing region, subregions 4, 11, and 24 show overall superiorities as compared with others in their neighborhoods. Therefore, they were short-listed for further consideration. The locations of the three short-listed subregions are shown in Figure 10b.

Table 1 lists the statistics of slopes, occlusions, crater densities, and rock abundances of the three short-listed subregions 4, 11, and 24. Their average slopes, crater densities, rock abundances, and occlusions to the Sun and relay satellite were further compared. From Table 1, it can be seen that subregion 11 shows the best performance in terms of all the aspects. Subregion 4 was ranked as the last, as it has a relatively high rock abundance and more serious occlusions to both the Sun and relay satellite. Subregion 11 was finally selected as the landing site with the highest priority, and Chang'E-4 actually landed in this subregion, with the exact location marked by a red cross in Figure 10b.

Landing Site Localization and Analysis

Localization of the Chang'E-4 Lander

On 3 January 2019, Chang'E-4 successfully landed in the Von Kármán crater. Identifying the exact location of the lander within the landing region and with respect to other surface features as soon as possible after landing was critical for planning science and engineering activities in the initial stages of surface exploration. The identification of other nearby features was also needed in traverse planning for the rover over the course of the mission. This was accomplished within two hours of landing before the rover drove off the lander. The related procedures involved Doppler positioning of the orbit track, reconstructing the entry, descent, and landing (EDL) process using returned descent images, and locating common features in the orbiter, descent, and ground images.

The navigation team determined the location of the lander at 45.5°S, 177.6°E, by Doppler positioning and orbit determination, which offered an initial location of the lander. A series of descent images collected by a descent camera mounted on the lander during the EDL process were used to reconstruct the lander's descent track, and the endpoint of the descent track was already close to the lander location. Finally, a ground panorama image, taken by the terrain camera mounted on top of the lander after landing, was used for the precise localization of the lander. As shown in Figure 11a, three meter-sized craters were manually identified on the ground panorama, and their centers were marked with red dots. Their corresponding positions on the descent image were then manually identified and marked with red dots as shown in Figure 11b. The descent image was geo-referenced to the LRO NAC image (M134022629L), as shown in the background in Figure 11b. The LRO NAC image was ortho-rectified using the Integrated Software for Imagers and Spectrometers software, which was already in the Mean Earth/Polar Axis reference system with planetocentric coordinates. The latitude and longitude coordinates of the lander were then calculated based on the optimal cartographic triangulation (Li *et al.* 2004) using these three

terrain features, which were in the same cartographic system of the used LRO NAC image. The elevation of the lander was measured from the DTM of the same location. The determined landing location of Chang'E-4 was at 45.4561°S, 177.5892°E, and at -5926 m elevation. The elevation was with respect to a reference sphere of radius 1737.4 km.

One week after the landing (on 11 January 2019), the LROC team at Arizona State University also identified the location of the Chang'E-4 lander at 45.457°S, 177.589°E, plus or minus 20 meters (<http://lroc.sese.asu.edu/posts/1087>), based on the co-registration of the Chang'E-4 descent frames and the NAC image (M1298916428LR). Liu *et al.* (2019) also located the Chang'E-4 landing site as 45.4446°S, 177.5991°E with an elevation of -5935 m using the digital orthophoto map and DTM of Chang'E-2 as geo-reference data, whose relative position to the surrounding terrain features is consistent with our results.

About one month later, after the successful landing of Chang'E-4, NASA's LRO passed by the Chang'E-4 landing region on 1 February 2019. The LRO NAC collected an image (M1303619844LR) of the landing region with a spatial resolution of 0.85 m/pixel, as shown in Figure 11c, on which the Chang'E-4 lander (the white dot with a dark shadow) and the Jade Rabbit-2 rover (the dark dot) can be clearly seen, as indicated by the white arrows. Comparing Figure 11b and 11c, it can be seen that the lander's location, as determined by our approach, is generally consistent with its real location, as imaged by the LRO NAC.

Analysis Around the Landing Site

After determining the lander's location, the analysis of its surrounding environment is vital for planning the subsequent science and engineering activities. We first examined the detailed terrain occlusions at the landing site. The approach described in the section "Occlusion Analysis" was adopted to analyze the occlusions at the landing site induced by the terrain, and the results are shown in Figure 12. Specifically, 360 geodesic lines were cast from the landing location at an azimuth interval of 1° as shown in Figure 12a. The position with the largest altitude angle induced by the nearby terrain was denoted by the endpoint of each geodesic line. Places with no geodesic lines visible are due to the terrain occlusions that happened in close ranges. Similarly, the relatively large occlusions were caused by the east-west rim of the Von Kármán crater. Overall, the terrain occlusion angles are generally less than 3° at the landing location. Figure 12b illustrates the relationships among the terrain occlusions, solar altitude angles, and altitude angles of the relay satellite among the terrain occlusions, solar altitude angles, and altitude angles of the relay satellite at the landing location for the six-month period after landing, from 3 January to 3 July 2019. It can be seen that the solar altitude angles and the altitude angles of the relay satellite are both much higher than the terrain occlusion angles at the landing location, which indicates its excellent visibility to the Sun and relay satellite.

For a detailed analysis of surface slopes and geometric information of small surface features around the landing location, higher resolution DTMs are required. However, at the time when Chang'E-4 landed, no high-resolution stereo pair of LRO NAC images had been collected around the landing site. Therefore, generating high-resolution DTMs from stereo images using the traditional photogrammetric approach was not possible. We developed an innovative sfs method for generating pixel-wise lunar DTMs from a single image with the constraint of a lower-resolution DTM (Wu *et al.* 2018a). Given a single image with a known light source, the sfs method is able to refine a lower-resolution DTM covering the same image area to higher resolution, the same as the image resolution, by using shading information to optimize regularization with respect to shape reconstruction (Kirk *et al.* 2003). Details about this sfs method can be found in our previous publications (Wu *et al.* 2018a; Liu *et al.* 2018). The developed sfs method was applied to the

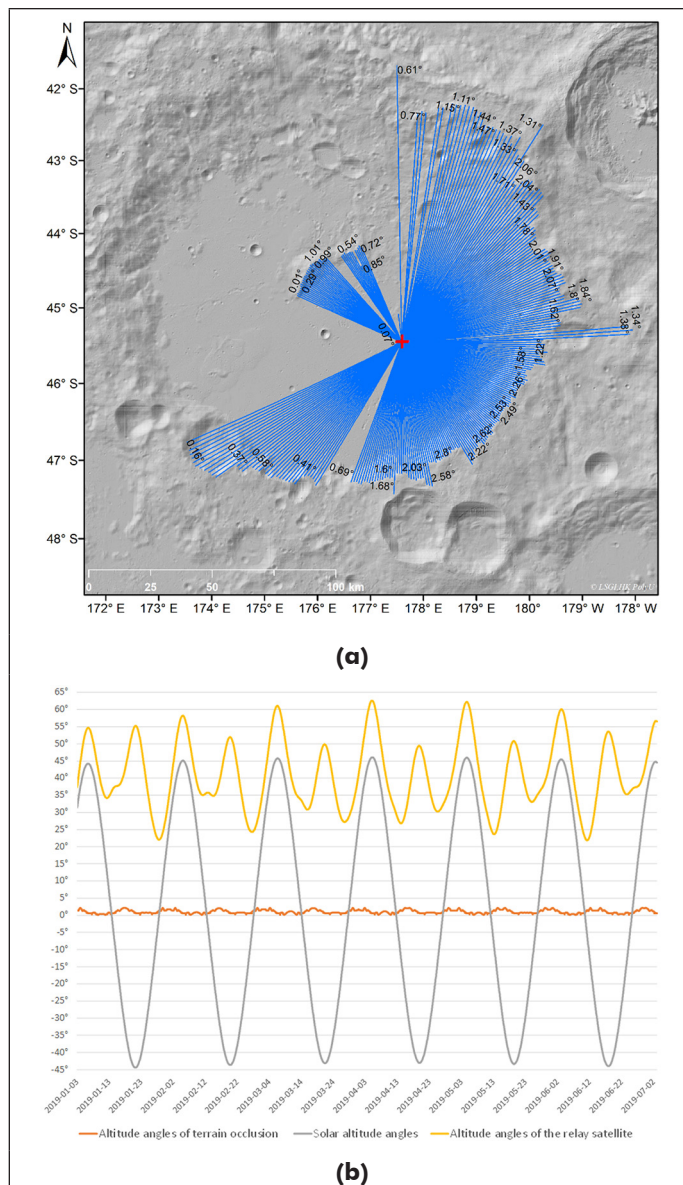


Figure 12. Occlusion analysis at the landing site. (a) The geodesic lines cast from the landing location (the red cross) at an interval of 1° and (b) the relationships among the terrain occlusions, solar altitude angles, and altitude angles of the relay satellite at the landing location for the six-month period after landing.

1.5 m/pixel LRO NAC image (M134022629L), and the SLDEM, with a resolution of 60 m used as the constraint, from which a high-resolution DTM (1.5 m/pixel) was generated, as shown in Figure 13. The differences in elevation between the sfs DTM and a photogrammetric DTM generated later using a stereo pair of NAC images is less than 5% (Liu and Wu 2020).

The upper row of Figure 13 shows a side-by-side comparison of the low-resolution SLDEM and the generated high-resolution sfs DTM, the latter showing overall consistent geometry with the former but providing much better details of the terrain features. The landing location of Chang'E-4 is marked in the sfs DTM and LRO NAC image with cyan crosses. It can be seen that the small craters around the landing location are clearly visible on the sfs DTM, but they are entirely missing on the SLDEM.

Based on the 1.5 m/pixel SFS DTM, a slope map with a baseline of 3 m was generated as shown in Figure 14a, from which it can be seen that the eastern part of the landing site has relatively larger slopes and the western part is relatively flat. For any point in the DTM, an aspect is calculated, which is the angle from the direction of the maximum slope at that point to the north direction. An aspect map was then generated to show the orientations of the slopes, as shown in Figure 14b. From the slope and aspect maps, the slope of the lander location is measured to be about 4.5°, and its aspect is toward southwest with an angle of 205° from the north.

The high-resolution DTM also enables the measurement of the detailed geometric information of small terrain features (e.g., diameters and depths of small craters) around the landing location. For instance, the three small craters surrounding the lander (see in Figure 13) have diameters of about 20–30 m and depths of about 2–2.6 m. These three craters all have a depth–diameter ratio of about 0.1. The shortest distance from the lander to any of these three craters is about 13 m. From the aforementioned rock abundance map, measurements show that the rock abundance around the landing location is almost 0. This type of detailed information is vital for the operation of instruments on the lander and for the surface operations of the rover.

Conclusions and Discussion

This paper presents the efforts concerning the landing site selection for the Chang'E-4 mission by jointly analyzing topographic and geomorphological features. Additionally, this paper describes the localization of the landing site and the analytical methods used to understand its surrounding area. The investigation leads to the following conclusions:

1. The DTM, with a resolution of 30 m generated from the integrated processing of Chang'E-2 images and LOLA data, reveals that the inner part of the Von Kármán crater is

quite flat. In the targeted landing region, about 5% of the areas have slopes larger than 8°. In addition, within the region there is satisfactory visibility to both the Sun and relay satellite, which are not occluded by the terrain surface in most areas.

2. The eastern part of the targeted landing region has relatively higher crater density. Overall, on average the crater density is about 60 craters (≥ 70 m in diameter) in a circular window of 10 km². Most of the landing region is rock-free based on our investigation, and most of the rocks are located around large impact craters and on the slopes of hills.
3. The joint analysis of surface slopes, occlusions to the Sun and relay satellite, crater densities, and rock abundances identified three subregions inside the targeted landing region. The one located close to the center of the region was recommended as the site with the highest priority, and the Chang'E-4 eventually landed at this site.
4. The integrated processing of orbiter, descent, and ground images identified the precise location of the Chang'E-4 lander within two hours after its successful landing, positioning it at 45.4561°S, 177.5892°E, and at -5926 m in elevation. This location is consistent with the actual observed location of the Chang'E-4 lander as fixed by the LRO NAC image one month later.
5. Detailed occlusion analysis around the landing location reveals that the lander has excellent visibility to the Sun and relay satellite. A detailed slope analysis around the landing location using an SFS DTM with a high resolution of 1.5 m/pixel indicates that the lander is on a slope of about 4.5° toward the southwest. The rock abundance around the landing location is almost 0.

The analytical methods described in this paper have demonstrated their effectiveness in real operations of the Chang'E-4 mission. The developed methods and results can benefit future missions of soft landings on the Moon and other celestial bodies.

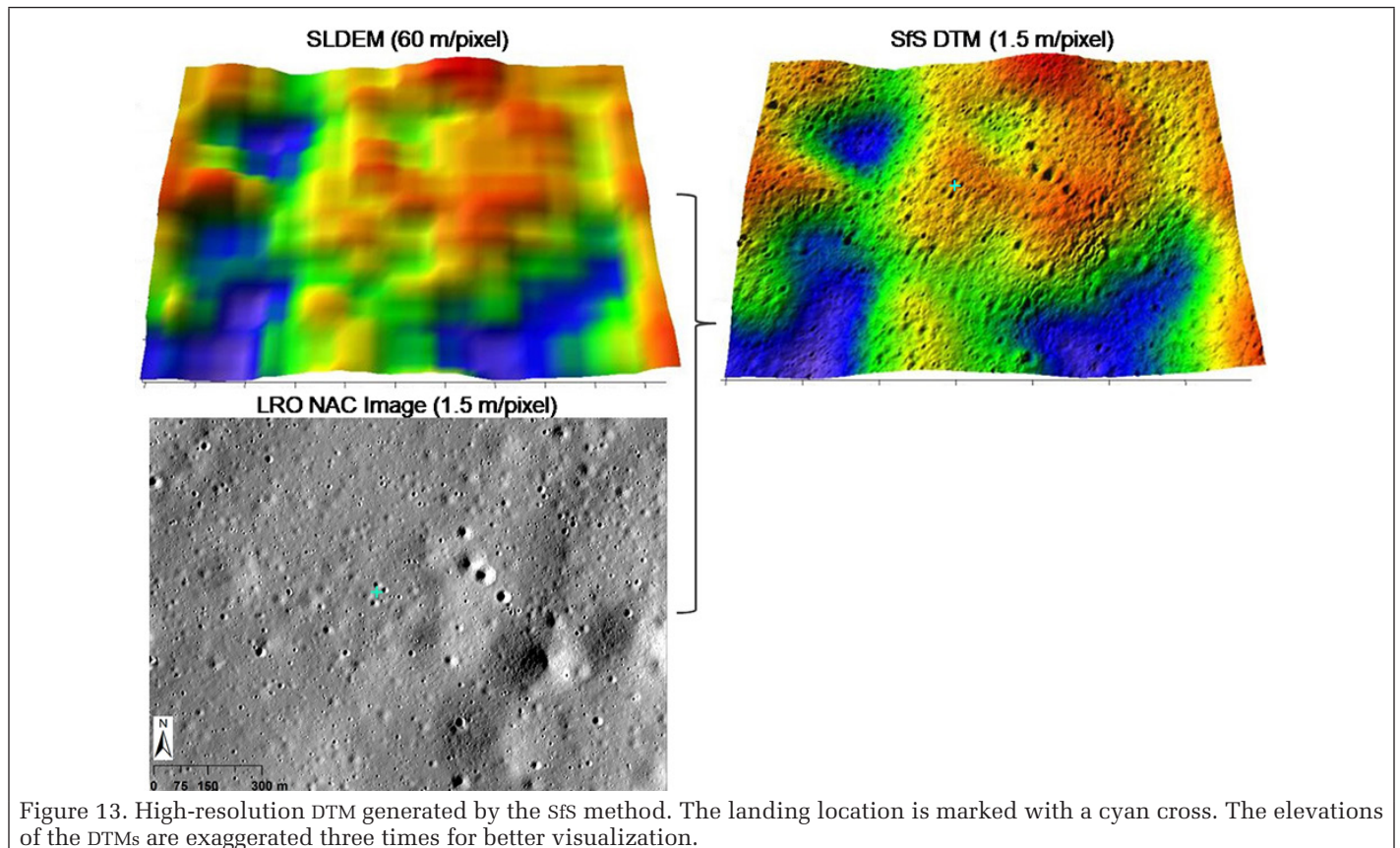


Figure 13. High-resolution DTM generated by the SFS method. The landing location is marked with a cyan cross. The elevations of the DTMs are exaggerated three times for better visualization.

Acknowledgments

This work was funded by China Academy of Space Technology (Project No: 17CPIT/HK0102) and a grant from the Research Grants Council of Hong Kong (Research Impact Fund - Project No: R5043-19). The work was also supported by a grant from the National Natural Science Foundation of China (Project No: 41671426). The authors would like to thank everyone who worked on the archives of the imagery and datasets used in this research for making them publicly available.

References

- Bandfield, J. L., R. R. Ghent, A. R. Vasavada, D. A. Paige, S. J. Lawrence and M. S. Robinson. 2011. Lunar surface rock abundance and regolith fines temperatures derived from LRO Diviner Radiometer data. *Journal of Geophysical Research: Planets* 116(E12).
- Barker, M. K., E. Mazarico, G. A. Neumann, M. T. Zuber, J. Haruyama and D. E. Smith. 2016. A new lunar digital elevation model from the Lunar Orbiter Laser Altimeter and SELENE Terrain Camera. *Icarus* 273:346–355.

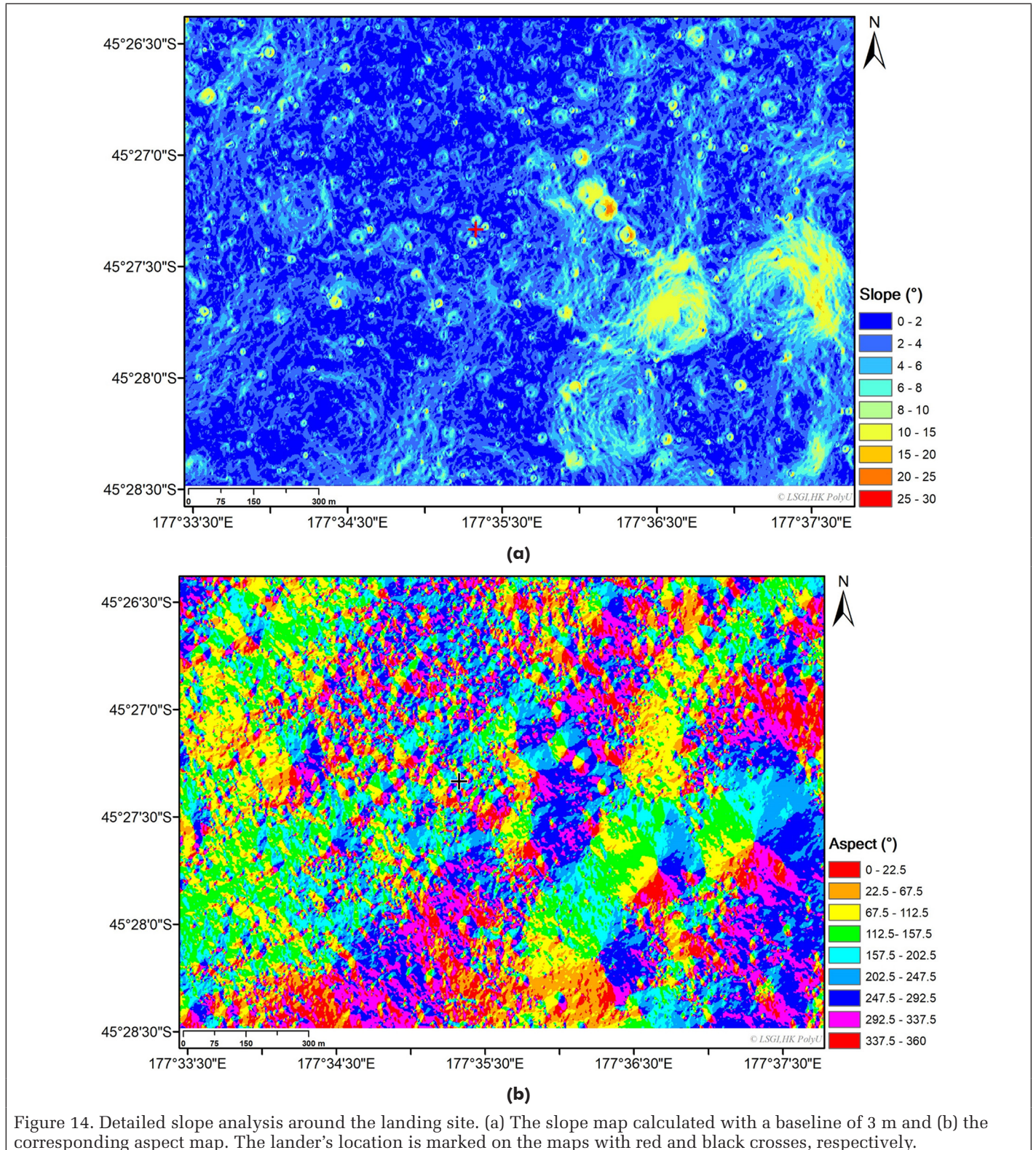


Figure 14. Detailed slope analysis around the landing site. (a) The slope map calculated with a baseline of 3 m and (b) the corresponding aspect map. The lander's location is marked on the maps with red and black crosses, respectively.

- Brady, T., E. Robertson, C. Epp, S. Paschall and D. Zimpfer. 2009. Hazard detection methods for lunar landing. Pages 1–8 in *Proceedings of the 2009 IEEE Aerospace Conference*.
- De Rosa, D., B. Bussey, J. T. Cahill, T. Lutz, I. A. Crawford, T. Hackwill, S. van Gassel, G. Neukum, L. Witte and A. McGovern. 2012. Characterization of potential landing sites for the European Space Agency's Lunar Lander project. *Planetary and Space Science* 74 (1):224–246.
- Di, K., M. Zhu, Z. Yue, Y. Lin, W. Wan, Z. Liu, S. Gou, B. Liu, M. Peng, Y. Wang, S. Niu, J. Zhang, J. Li, J. Xie, L. Xi, J. Yang and B. Xue. 2019. Topographic evolution of Von Kármán crater revealed by the lunar rover Yutu-2. *Geophysical Research Letters* 46 (22):12764–12770.
- Golombek, M. and D. Rapp. 1997. Size frequency distributions of rocks on Mars and Earth analog sites: Implications for future landed missions. *Journal of Geophysical Research: Planets* 102 (E2):4117–4129.
- Golombek, M. P., A. Haldemann, N. Forsberg-Taylor, E. N. Di Maggio, R. D. Schroeder, B. M. Jakosky, M. Mellon and J. Matijevic. 2003. Rock size-frequency distributions on Mars and implications for Mars Exploration Rover landing safety and operations. *Journal of Geophysical Research* 108 (E12):8086.
- Golombek, M., D. Kipp, N. Warner, I. J. Daubar, R. Ferguson, R. L. Kirk and B. A. Campbell. 2017. Selection of the InSight landing site. *Space Science Reviews* 211 (1–4):5–95.
- Hu, H. and B. Wu. 2019. Planetary3D: A photogrammetric tool for 3D topographic mapping of planetary bodies. *ISPRS Annals of the Photogrammetry, Remote Sensing and Spatial Information Sciences* IV-2/W5:519–526.
- Hu, H., C. Chen, B. Wu, X. Yang, Q. Zhu and Y. Ding. 2016. Texture-aware dense image matching using ternary census transform. *ISPRS Annals of the Photogrammetry, Remote Sensing and Spatial Information Sciences* III-3:59–66.
- Huang, J., Z. Xiao, J. Flahaut, M. Martinot, J. Head, X. Xiao, M. Xie and L. Xiao. 2018. Geological characteristics of Von Kármán crater, northwestern south Pole Aitken basin: Chang'E 4 landing site region. *Journal of Geophysical Research: Planets* (123):1684–1700.
- Jia, Y., Y. Zou, J. Ping, C. Xue, J. Yan and Y. Ning. 2018. The scientific objectives and payloads of Chang'E-4 mission. *Planetary and Space Science* 162:207–215.
- Karney, C. F. 2013. Algorithms for geodesics. *Journal of Geodesy* 87 (1):43–55.
- Kirk, R. L., E. Howington-Kraus, B. Redding, D. Galuszka, T. M. Hare, B. A. Archinal, L. A. Soderblom and J. M. Barrett. 2003. High-resolution topomapping of candidate MER landing sites with Mars Orbiter Camera narrow-angle images. *Journal of Geophysical Research: Planets* 108 (E12):8088.
- Li, C., D. Liu, B. Lu, X. Ren, J. Liu, Z. He, W. Zuo, X. Zeng, R. Xu, X. Tan, X. Zhang, W. Chen, R. Shu, W. Wen, Y. Su, H. Zhang and Z. Ouyang. 2019. Chang'E-4 initial spectroscopic identification of lunar far-side mantle-derived materials. *Nature* 569:378–382.
- Li, F., H. Zhang, X. Wu, J. Ma and L. Lu. 2017. Influence analysis of terrain of the far side of the Moon on soft-landing. *Journal of Deep Space Exploration* 4 (2):143–149.
- Li, R., K. Di, L. H. Matthies, W. M. Folkner, R. E. Arvidson and B. A. Archinal. 2004. Rover localization and landing-site mapping technology for the 2003 Mars exploration rover mission. *Photogrammetric Engineering and Remote Sensing* 70 (1):77–90.
- Li, Y. and B. Wu. 2018. Analysis of rock abundance on lunar surface from orbital and descent images using automatic rock detection. *Journal of Geophysical Research: Planets* 123 (5):1061–1088.
- Liu, W. C., B. Wu and C. Wöhler. 2018. Effects of illumination differences on photometric stereo shape-and-albedo-from-shading for precision lunar surface reconstruction. *ISPRS Journal of Photogrammetry and Remote Sensing* 136:58–72.
- Liu, W. C. and B. Wu. 2020. An integrated photogrammetric and photoclinometric approach for illumination-invariant pixel-resolution 3D mapping of the lunar surface. *ISPRS Journal of Photogrammetry and Remote Sensing* 159:153–168.
- Liu, J., X. Ren, W. Yan, C. Li, H. Zhang, Y. Jia, X. Zeng, W. Chen, X. Gao, D. Liu, X. Tan, X. Zhang, T. Ni, H. Zhang, W. Zuo, Y. Su and W. Wen. 2019. Descent trajectory reconstruction and landing site positioning of Chang'E-4 on the lunar farside. *Nature Communications* 10:4229.
- Pajola, M., S. Rossato, E. Baratti, R. Pozzobon, C. Quantin, J. Carter and P. Thollot. 2017. Boulder abundances and size-frequency distributions on Oxia Planum-Mars: Scientific implications for the 2020 ESA ExoMars rover. *Icarus* 296:73–90.
- Wang, Y. and B. Wu. 2017. Improved large-scale slope analysis on Mars based on correlation of slopes derived with different baselines. *International Archives of the Photogrammetry, Remote Sensing and Spatial Information Sciences* 42.
- Wang, Y. and B. Wu. 2019. Active machine learning approach for crater detection from planetary imagery and digital elevation models. *IEEE Transactions on Geoscience and Remote Sensing* 57 (8):5777–5789.
- Wilhelms, D. E., F. John and N. J. Trask. 1987. *The Geologic History of the Moon*. Washington, D.C.: U.S. Geological Survey.
- Wu, B., F. Li, L. Ye, S. Qiao, J. Huang, X. Wu and H. Zhang. 2014a. Topographic modeling and analysis of the landing site of Chang'E-3 on the Moon. *Earth and Planetary Science Letters* 405:257–273.
- Wu, B., H. Hu and J. Guo. 2014b. Integration of Chang'E-2 imagery and LRO laser altimeter data with a combined block adjustment for precision lunar topographic modeling. *Earth and Planetary Science Letters* 391:1–15.
- Wu, B., W. C. Liu, A. Grumpe and C. Wöhler. 2018a. Construction of pixel-level resolution DEMs from monocular images by shape and albedo from shading constrained with low-resolution DEM. *ISPRS Journal of Photogrammetry and Remote Sensing* 140:3–19.
- Wu, B., J. Huang, Y. Li, Y. Wang and J. Peng. 2018b. Rock abundance and crater density in the candidate Chang'E-5 landing region on the Moon. *Journal of Geophysical Research—Planets* 123 (12):3256–3272.
- Wu, W. R., Q. Wang, Y. H. Tang, J. Z. Liu and L. L. Lu. 2017. Design of Chang'E-4 lunar farside soft-landing mission. *Journal of Deep Space Exploration* 4 (2):111–117.

SUSTAINING MEMBERS

ACI USA Inc.

Weston, Florida
acicorporation.com
Member Since: 1/2018

Aerial Services, Inc.

Cedar Falls, Iowa
www.AerialServicesInc.com
Member Since: 5/2001

Airbus Defense and Space

Chantilly, Virginia
www.intelligence-airbusds.com
Member Since: 11/2018

Ayres Associates

Madison, Wisconsin
www.AyresAssociates.com
Member Since: 1/1953

Bohannon Huston, Inc.

Albuquerque, New Mexico
www.bhinc.com
Member Since: 11/1992

Cardinal Systems, LLC

Flagler Beach, Florida
www.cardinalsystems.net
Member Since: 1/2001

Dewberry

Fairfax, Virginia
www.dewberry.com
Member Since: 1/1985

Environmental Research Incorporated

Linden, Virginia
www.eri.us.com
Member Since: 8/2008

Esri

Redlands, California
www.esri.com
Member Since: 1/1987

GeoBC

Victoria, Canada
www.geobc.gov.bc.ca
Member Since: 12/2008

GeoCue Group

Madison, Alabama
info@geocue.com
Member Since: 10/2003

Geojano

Pleasanton, California
https://geojano.com/
Member Since: 05/2019

Geomni, Inc.

Lehi, Utah
Geomni.net/psm
Member Since: 03/2018

GeoWing Mapping, Inc.

Richmond, California
www.geowingmapping.com
Member Since: 12/2016

Global Science & Technology, Inc.

Greenbelt, Maryland
www.gst.com
Member Since: 10/2010

GPI Geospatial Inc.

formerly **Aerial Cartographics of America, Inc. (ACA)**
Orlando, Florida
www.aca-net.com
Member Since: 10/1994

Green Grid Inc.

San Ramon, California
www.greengridinc.com
Member Since: 1/2020

Kucera International

Willoughby, Ohio
www.kucerainternational.com
Member Since: 1/1992

L3Harris Corporation

Broomfield, Colorado
www.harris.com
Member Since: 6/2008

Martinez Geospatial, Inc. (MTZ)

Eagan, Minnesota
www.mtzgeo.com
Member Since: 1/1979

Pickett and Associates, Inc.

Bartow, Florida
www.pickettusa.com
Member Since: 4/2007

Quantum Spatial, Inc.

Sheboygan Falls, Wisconsin
www.quantumspatial.com
Member Since 1/1974

Robinson Aerial Survey, Inc. (RAS)

Hackettstown, New Jersey
www.robinsonaerial.com
Member Since: 1/1954

Routescene, Inc.

Durango, Colorado
www.routescene.com/
Member Since: 12/2007

Sanborn Map Company

Colorado Springs, Colorado
www.sanborn.com
Member Since: 10/1984

Towill, Inc.

San Francisco, California
www.towill.com
Member Since: 1/1952

Trimble

Munich, Germany
www.trimble.com/geospatial
Member Since: 4/19942

U.S. Geological Survey

Reston, Virginia
www.usgs.gov
Member Since: 4/2002

Woolpert LLP

Dayton, Ohio
www.woolpert.com
Member Since: 1/1985

Advertise in the #1 publication in the imaging and geospatial information industry!



Impact Factor (2018): 3.15

PE&RS (*Photogrammetric Engineering & Remote Sensing*) is the official journal of the American Society for Photogrammetry and Remote Sensing—the Imaging and Geospatial Information Society (ASPRS). This highly respected publication is the #1 publication in the industry by a wide margin. Advertisers with a desire to reach this market can do no better than PE&RS. It delivers the right audience of professionals who are loyal and engaged readers, and who have the purchasing power to do business with you.

PE&RS Readership Highlights

Circulation: 3,000
Total audience: 6,400*

Founded in 1934, the American Society for Photogrammetry and Remote Sensing (ASPRS) is a scientific association serving professional members throughout the world. Our mission is to advance knowledge and improve understanding of mapping sciences to promote the responsible applications of photogrammetry, remote sensing, geographic information systems (GIS), and supporting technologies.

Our members are analysts/specialists, educators, engineers, managers/administrators, manufacturers/ product developers, operators, technicians, trainees, marketers, and scientists/researchers. Employed in the disciplines of the mapping sciences, they work in the fields of Agriculture/Soils, Archeology, Biology, Cartography, Ecology, Environment, Forestry/Range, Geodesy, Geography, Geology, Hydrology/Water Resources, Land Appraisal/Real Estate, Medicine, Transportation, and Urban Planning/Development.

RESERVE YOUR SPACE TODAY!

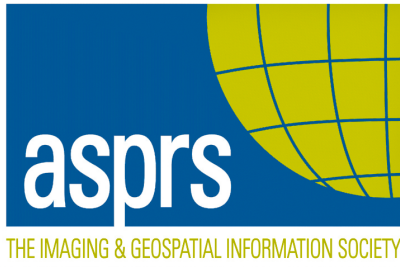
Bill Spilman, ASPRS Advertising, Exhibit Sales & Sponsorships
(877) 878-3260 toll-free
(309) 483-6467 direct
(309) 483-2371 fax
bill@innovativemediasolutions.com

	Corporate Member Exhibiting at a 2019 ASPRS Conference	Corporate Member	Exhibitor	Non Member
<i>All rates below are for four-color advertisements</i>				
Cover 1	\$1,850	\$2,000	\$2,350	\$2,500
<i>In addition to the cover image, the cover sponsor receives a half-page area to include a description of the cover (maximum 500 words). The cover sponsor also has the opportunity to write a highlight article for the journal. Highlight articles are scientific articles designed to appeal to a broad audience and are subject to editorial review before publishing. The cover sponsor fee includes 50 copies of the journal for distribution to their clients. More copies can be ordered at cost.</i>				
Cover 2	\$1,500	\$1,850	\$2,000	\$2,350
Cover 3	\$1,500	\$1,850	\$2,000	\$2,350
Cover 4	\$1,850	\$2,000	\$2,350	\$2,500
Advertorial	1 Complimentary Per Year	1 Complimentary Per Year	\$2,150	\$2,500
Full Page	\$1,000	\$1,175	\$2,000	\$2,350
2 page spread	\$1,500	\$1,800	\$3,200	\$3,600
2/3 Page	\$1,100	\$1,160	\$1,450	\$1,450
1/2 Page	\$900	\$960	\$1,200	\$1,200
1/3 Page	\$800	\$800	\$1,000	\$1,000
1/4 Page	\$600	\$600	\$750	\$750
1/6 Page	\$400	\$400	\$500	\$500
1/8 Page	\$200	\$200	\$250	\$250
Other Advertising Opportunities				
Wednesday Member Newsletter Email Blast	1 Complimentary Per Year	1 Complimentary Per Year	\$600	\$600

A 15% commission is allowed to recognized advertising agencies

THE MORE YOU ADVERTISE THE MORE YOU SAVE! PE&RS offers frequency discounts. Invest in a three-times per year advertising package and receive a 5% discount, six-times per year and receive a 10% discount, 12-times per year and receive a 15% discount off the cost of the package.

*Based on 2 readers per copy as well as online views | Source: PE&RS Readership Survey, Fall 2012



ASPRS AERIAL DATA CATALOG

“THE SOURCE FOR FINDING AERIAL COLLECTIONS”

[HTTP://DPAC.ASPRS.ORG](http://dpac.asprs.org)

The ASPRS Aerial Data Catalog is a tool allowing owners of aerial photography to list details and contact information about individual collections.

By providing this free and open metadata catalog with no commercial interests, the Data Preservation and Archiving Committee (DPAC) aims to provide a definitive metadata resource for all users in the geospatial community to locate previously unknown imagery.

DPAC hopes this Catalog will contribute to the protection and preservation of aerial photography around the world!

ASPRS Members: We Need Your Help!
There are three ways to get involved

1

USE

Use the catalog to browse over 5,000 entries from all 50 states and many countries. Millions of frames from as early as 1924!

2

SUPPLY

Caretakers of collections, with or without metadata, should contact DPAC to add their datasets to the catalog free of charge!

3

TELL

Spread the word about the catalog! New users and data collections are key to making this a useful tool for the community!

For More Details or To Get Involved Contact:

DAVID RUIZ • DRUIZ@QUANTUMSPATIAL.COM • 510-834-2001 OR DAVID DAY • DDAY@KASURVEYS.COM • 215-677-3119

LEARN
DO
GIVE
BELONG

ASPRS Offers

- » Cutting-edge conference programs
- » Professional development workshops
- » Accredited professional certifications
- » Scholarships and awards
- » Career advancing mentoring programs
- » *PE&RS*, the scientific journal of ASPRS

asprs.org

ASPRS